THEORETICAL MODELING AND EXPERIMENTAL CHARACTERIZATION OF STRESS AND CRACK DEVELOPMENT IN PARTS MANUFACTURED THROUGH LARGE AREA MASKLESS PHOTOPOLYMERIZATION

A Dissertation
Presented to
The Academic Faculty

by

Tao Wu

In Partial Fulfillment
of the Requirements for the Degree
Doctor of Philosophy in the
George W. Woodruff School of Mechanical Engineering

Georgia Institute of Technology
December 2014

THEORETICAL MODELING AND EXPERIMENTAL CHARACTERIZATION OF STRESS AND CRACK DEVELOPMENT IN PARTS MANUFACTURED THROUGH LARGE AREA MASKLESS PHOTOPOLYMERIZATION

Approved by:

Dr. Suman Das, Advisor
School of Mechanical Engineering
Georgia Institute of Technology

Dr. John Halloran
School of Materials Science and Engineering
University of Michigan

Dr. Karl I. Jacob
School of Materials Science and Engineering
Georgia Institute of Technology

Dr. Shuman Xia
School of Mechanical Engineering
Georgia Institute of Technology

Dr. Suresh K. Sitaraman
School of Mechanical Engineering
Georgia Institute of Technology

Date Approved: August 13, 2014

To my family.

ACKNOWLEDGEMENTS

First of all, I would like to thank my advisor, Dr. Suman Das, for his constant support and great patience throughout the tenure of my PhD. I have developed and learned a lot from him. Without his guidance, vision and support, this dissertation would be hard to be accomplished. I would also like to extend my sincerest gratitude to my reading committee, composed of Dr. Shuman Xia, Dr. Karl I. Jacob, Dr. Suresh K. Sitaraman and Dr. John Halloran. I am grateful for all their precious time and valuable advice that help me improve the quality of this dissertation.

Secondly, I would like to acknowledge all my fellow members of the Direct Digital Manufacturing Laboratory, Dr. Dajun Yuan, Dr. Rui Guo, Dr. Raphael Alabi, Dr. Anirudh V. Rudraraju, Dr. Chan Yoon, Ranadip Acharya, Mathew Conrad, Shaun Eshragi and Kiran Kambly. I am thankful for their camaraderie and that they can share their professional knowledge, experience and expertise with me. I would also like to thank several employees in DDM Systems, Dr. Erica Krivoy Davis, Dr. Michael Middlemas and Dr. Marvin Kilgo, for assisting me in using the LAMP machine and helping me prepare LAMP suspensions used in my experiments.

Thirdly, I would like to acknowledge Dr. Samuel Graham for allowing me access to his laboratory to conduct the DCB and ENF tests. I would like to extend my gratitude to Dr. Yongjin Kim and Sathyanarayanan Raghavan, for training me to use the test instrument and giving me advice on my research. I would also like to acknowledge Dr. Joseph W. Perry for allowing me access to his laboratory to use the FTIR instrument. I would also like to extend my gratitude to Dr. Vincent Chen for training me on conducting the FTIR analysis. In addition, I would like to thank Dr. Jeffrey Donnell for reviewing my dissertation and helping me make corrections to the text. I am grateful for his kindly comments on my writings, from which I learned a lot. I would also like to thank all of my friends, both in USA and in China, for their company that made the course of my study colorful and enjoyable.

Most importantly, I would like to express my sincerest gratitude to my family, whose constant love, steadfast support and encouragement gave me the confidence and strength to successfully accomplish my dissertation. I am truly grateful for their endless patience and thoughtfulness through all these years.

TABLE OF CONTENTS

LIST OF TABLES

LIST OF FIGURES

LIST OF ABBREVIATIONS

LAMP	Large Area Maskless Photopolymerization
DDM	Direct Digital Manufacturing
SLM	Spatial Light Modulator
DMD	Digital Micro-mirror Device
CAD	Computer Aided Design
SLS	Selective Laser Sintering
SLM	Selective Laser Melting
SL	Stereolithography
FDM	Fused Deposition Modeling
BBO	Binder Burn-out
FTIR	Fourier Transform Infrared Spectroscopy
DCB	Double Cantilever Beam
ENF	End Notched Flexure
IPA	Isopropyl Alcohol
ATR	Attenuated Total Reflectance
IR	Infrared
HDDA	Hexanediol Diacrylate

EPETA	Ethoxylated Pentaerythritol Tetraacrylate
FEA	Finite Element Analysis
BCM	Bridge Curvature Method
LEFM	Linear Elastic Fracture Mechanics
BT	Beam Theory
MBT	Modified Beam Theory
CC	Compliance Calibration
MCC	Modified Compliance Calibration
ELS	End Loaded Split
4ENF	Four Point End Notched Flexure
CBB	Compliance Based Beam
CBT	Corrected Beam Theory
FPZ	Fracture Process Zone
CZ	Cohesive Zone

LIST OF SYMBOLS

G_{Ic}	Mode I interlaminar fracture toughness
G_{IIc}	Mode II interlaminar fracture toughness
I	Initiator
$R\bullet$	Radical
M	Monomer molecule
$P_1\bullet$	Radical polymer chain of unit length
$P_n\bullet$	Radical polymer chain of length n
P_n	Dead polymer chain of length n
Z	Inhibitor species
$P_nZ\bullet$	Inhibited chain
k_i	Kinetic constant for chain initiation
k_i'	Kinetic constant for chain re-initiation
k_p	Kinetic constant for propagation reaction
k_t	Kinetic constant for bimolecular termination
k_{tp}	Kinetic constant for second termination mechanism
k_z	Kinetic constant for chain inhibition
z	Depth into the material

$E(z)$	Energy dose as a function of depth z traveled through the medium
D_p	Penetration depth
E_c	Critical energy dose
C_d	Cure depth
I	Light intensity
t	Exposure time
M_m	Molecular weight
ρ_m	Density of the monomer
FL	Filler loading in percentage
α	Degree of conversion in the monomer
f	Functionality of the monomer
V	Volume of the slurry
ρ_{mix}	Density of the monomer mixture
χ_i	Mole fraction of monomer (i)
ε_T	Linear shrinkage strain
ν	Poisson’s ratio
E_0	Instantaneous isotropic resin modulus
$E_{\alpha 0}$	Young’s modulus of uncured resin
$E_{\alpha 1}$	Young’s modulus of fully cured resin
$\overline{E}_{\alpha 0}$	Effective Young’s modulus of the uncured composite

$\overline{E}_{\alpha m}$	Maximum effective Young’s modulus of the cured composite
α_m	Maximum degree of conversion
$\overline{K}$	Effective bulk modulus of the composite
$\overline{\mu}$	Effective shear modulus of the composite
$\overline{E}$	Effective Young’s modulus of the composite
K_0	Bulk modulus of resin
K_1	Bulk modulus of particle
P	Load force
δ	Deflection
B	Specimen width
h	Specimen height
U	Strain energy
G	Energy release rate
K	Stress intensity factor
C	Compliance
a	Crack length
a_0	Initial crack length
D	Damage variable
t_n^0	Mode I interlaminar strength of cohesive element
t_s^o	Mode II interlaminar strength of cohesive element

K_n	Interfacial normal stiffness of cohesive element
K_s	Interfacial shear stiffness of cohesive element
l_{cz}	Cohesive zone length

SUMMARY

Large Area Maskless Photopolymerization (LAMP) is a disruptive additive manufacturing technology developed in the Direct Digital Manufacturing Laboratory at Georgia Tech. In LAMP, a programmable UV light source projects high resolution bitmap images through a digital micro-mirror device (DMD) chip to selectively cure areas of photocurable ceramic-loaded liquid resin layers according to patterns in the input image. Three-dimensional parts are thus built layer-by-layer with both high speed and fine feature resolution through LAMP. Upon production through LAMP, the polymer-ceramic composite parts are subjected to post-processing steps of binder burnout and sintering, ultimately resulting in fully ceramic parts that can be used as cores and shell molds for investment casting of metal components. Some of the key requirements for castability to be satisfied by such parts are their mechanical properties in the fired state, their structural integrity, and the lack of flaws such as cracks or delaminations. However, due to polymerization shrinkage during the layer-by-layer curing process, stresses are accumulated that can give rise to cracks and delaminations along the interfaces between adjacent layers. Cracks or delaminations present in the polymer-ceramic composite "green state" are known to propagate and manifest during the subsequent post-processing steps, resulting in unacceptable parts. The objective of this doctoral dissertation is to investigate the mechanisms of stress evolution and cracking/delamination during the LAMP manufacturing process. This investigation is

based on both theoretical modeling and experimental characterization. The ultimate objective of this dissertation is to elucidate strategies to alleviate or eliminate the defects and to achieve defect-free parts in arbitarily complex three-dimensional geometries.

In order to predict residual stresses and distortions occurring in LAMP-built parts, an elastic model has been developed. Due to light penetration through the upper layers, almost all of the layers, except for the topmost ones, are incrementally cured as subsequent layers above them are being exposed. This phenomenon is referred to as print-through. For each layer, the degree of conversion keeps increasing for several successive layers until no more curing occurs and a final value of conversion degree is reached. The evolving conversion degree in a layer has been characterized through Fourier Transform Infrared Spectroscopy (FTIR) and this leads to a so-called print-through curve. The polymerization shrinkage strain in each exposed layer has been calculated on the basis of the theoretical relationship between the volumetric shrinkage as a function of double-bond formation and the degree of conversion. Furthermore, the material’s elastic modulus, which also evolves with the degree of conversion, has been characterized by three-point bending tests. With the degree of conversion, cure-dependent modulus and shrinkage strain as the three primary inputs, finite element modeling has been conducted to dynamically simulate the layer-by-layer manufacturing process and to predict the process-induced stresses.

To investigate the fracture process, Mode I and Mode II interlaminar fracture toughness ($G_{Ic}\ and\ G_{IIc}$) of the LAMP-built laminates have been characterized, using the double cantilever beam (DCB) test and the end notched flexure (ENF) test, respectively. The data reduction schemes used for these testing methods are also presented.

In order to predict the crack initiation and propagation occurring in a LAMP-built part, a mixed-mode cohesive element model has been developed. In this model, cohesive elements are placed along every inter-layer interface of the laminates. The formulation of the cohesive finite elements is based on the cohesive zone model approach which assumes that a cohesive damage zone develops near the crack tip. The Mode I and Mode II cohesive parameters, which are used to describe the bilinear constitutive behavior of the cohesive elements, are determined by matching the numerical load-deflection curves to the experimental ones obtained from the DCB tests and the ENF tests, respectively. Using this model, the fracture of a hollow-cylinder part has been analyzed and the simulation results are compared with experiments.

Finally, a discussion on the strategies for mitigating the shrinkage related defects is presented. Reducing the overall polymerization shrinkage, optimizing the print-through curve and delaying the gel point of resin composite are demonstrated to be effective in reducing stresses and cracks.

CHAPTER 1

INTRODUCTION

Large Area Maskless Photopolymerization (LAMP) is a technology that has been developed by the Direct Digital Manufacturing (DDM) laboratory at Georgia Tech in collaboration with the University of Michigan and PCC Airfoils under the sponsorship of DARPA's Disruptive Manufacturing Technologies Program. It is a novel additive manufacturing process that can build three-dimensional objects layer-by-layer with both high speed and fine feature resolution. The current application of LAMP is in the manufacturing of integrally-cored ceramic molds for the investment casting of turbine blades that have complex internal cooling passages. By alleviating the need for tooling and manual labor, LAMP can lead to remarkable cost savings and significant reduction in lead times; it can therefore greatly impact the current state-of-the-art investment casting of turbine blades in industry.

A schematic of the LAMP process is shown in Figure 1.1. An essential element of the LAMP system is the spatial light modulator (SLM), which is a digital micro-mirror device (DMD). It is an optical chip with more than 1.3 million micro mirrors that can be turned on or off according to the color (white or black) of pixels in the corresponding bitmap image. A UV source is used to project light onto the DMD and expose large areas of photocurable ceramic-loaded liquid resin according to the input image. The optical imaging head, with the UV light source, DMD chip and projection optics inside, moves in a serpentine path and raster scans the build area. Complex three-dimensional parts are produced by sweeping and exposing successive layers of the ceramic-loaded resin wherein each layer corresponds to a digital slice of the CAD model of the part. Using this exposure mechanism, LAMP can realize massively parallel patterning, and its speed is much higher than that of traditional stereolithography, in which only a single laser beam is used to raster scan the exposure region point-by-point. The feature resolution achievable in this process is only limited by the DMD chip used and the projection optics. The DMD chip in the current setup has an array of 1024x768 micro mirrors with size of 17μm each, with projection optics of 1:1 magnification.

Figure 1.1 Schematic illustration of LAMP machine

LAMP is an additive manufacturing process; it was developed in order to fabricate functional ceramic components. It has many unique and novel features that make it superior to other direct digital manufacturing processes and enable it to build turbine blade molds with extremely complex cooling passages. However, some of these features, coupled with the inherent disadvantages of the layer-by-layer process used by all additive manufacturing technologies, may cause the fabricated parts to have defects, such as residual stress, distortion and delamination. This dissertation aims to characterize these defects and to search for possible approaches to alleviate them. To this end, this chapter gives an introduction to the background and motivation for the work presented in this dissertation. In the first section, various classes of additive manufacturing processes are summarized. Then, the LAMP process is described, and the characteristics that make it distinct from other additive manufacturing processes are introduced in section 1.2. The next section discusses the significance of studying the defects, especially cracks, that occur during the LAMP process. Descriptions are given for the cracks and delaminations appearing on the parts built through LAMP. Possible sources of these defects are provided, and polymerization shrinkage is introduced as one of the biggest reasons. Over the past several decades, there have been various studies on the defects observed in other additive manufacturing processes, and section 1.4 provides a literature review of these studies. Following the introduction to the background and motivation, the outline of this dissertation is given at the end of this chapter.

1.1 Additive Manufacturing Technology

Additive manufacturing is also referred to as rapid prototyping, solid freeform fabrication, direct digital manufacturing, among other names. It is an emerging technology in which three-dimensional objects can be manufactured directly, using a layer-by-layer process based on computer-aided design (CAD) models. The CAD model is either designed via CAD software or obtained from 3D scanning or tomography, respectively. Next, the respective model data is sliced through computer code into 2D images with desired slicing thickness. On the building system, a moving stage moves down as the part is built upon it according to the layer thickness. A recoating system is used to apply an appropriate amount of material for each layer. The patterns in the sliced images are then achieved by following different physical and chemical principles in the various RP processes. Various additive manufacturing systems are currently available, and these generally can be classified into three categories according to the characteristics of the processing material, 1) the solid-based system (e.g. Laminated Object Manufacturing and Fused Deposition Modeling), 2) the powder-based system (e.g. Selective Laser Sintering/Melting and Three-dimensional Printing), and 3) the liquid-based system (e.g. Stereolithography). In these various systems, the energy sources and deposition methods used are also different. For instance, selective laser sintering/melting (SLS/SLM) systems use a high-energy laser beam to raise the temperature of polymer, ceramic or metal powders to a point above the glass transition or melting point so as to form an individual layer. Stereolithography apparatus (SLA) systems use an ultraviolet laser beam to selectively cure liquid photo-curable resins into solid. Fused deposition modeling (FDM) systems extrude and deposit fused thermoplastics. Due to its intrinsic ability to fabricate objects directly from CAD models, additive manufacturing technology is especially suitable for manufacturing products that have complex shapes and internal structures. Over the past two decades, with improving accuracy, time and cost efficiency, the scope of their application has widened considerably. Additive manufacturing is today used in industries that include the fabrication of molds and dies, production of aircraft component prototypes for aerodynamic analysis, and the making of full-size automobile instrument panels [1].

Although they hold promise for industrial applications, additive manufacturing processes have inherent limitations. Some of these limitations prevent additive manufacturing technologies from being applied in industries when they compete with conventional manufacturing methods. Speed is the first severe limitation in many of the technologies, as they use a single laser beam to vector scan; this means that a single laser is used to scan point-by-point or line-by-line in order to pattern each layer. For industrial production that requires high throughput, these technologies would be too slow to use.

Another limitation is the need for support structures to successfully build geometries that lead to unsupported or floating islands. These support structures must be removed when building is concluded, since they are not a functional part of the design. However, in many applications, such as the case of integrally cored molds for investment casting, the core features are completely encapsulated by the outer shell, making it impossible to remove the support structures after the build.

Scalability is a limitation for many additive manufacturing technologies that are tailored to work best at specific length scales. These technologies are designed specifically according to the length scales, i.e. macro or micro size, of the components they are used to fabricate. For instance, stereolithography or selective laser sintering uses a galvanometer mirror to position the laser spot for building each layer. The minimum feature resolution that these processes can achieve decreases greatly when the build areas increase in size, since the mirror's discrete number of positions will be mapped over larger and larger areas. These limitations significantly affect the further application of many additive manufacturing technologies in industries. Many researchers are working on alternative methods to eliminate these limitations, and LAMP can be a promising alternative amongst them.

1.2 Large Area Maskless Photopolymerization (LAMP) Technology

Large Area Maskless Photopolymerization (LAMP) can be categorized as a liquid-based additive manufacturing technology. However, it possesses two unique characteristics that make it distinct from others such as stereolithography (SL). The first characteristic is the material system used. In LAMP, ceramic particle-loaded photocurable resins are used as the building material instead of the pure resin used in SL. A typical photopolymerizable material composition for LAMP consists of monomers, ceramic particles, dispersant, photoinitiators and absorbers. The monomers used in the current system involve a mixture of HDDA and EPETA. HDDA is a low volatility, low viscosity monomer, while EPETA is a fast curing monomer. Silica particles with 7μm mean diameter, and with 95% of all particles less than 25μm in diameter, are chosen as filler content. A dispersant such as Variquat CC59 is added to prevent agglomeration of the filler particles. The photoinitiator system is chosen to match the spectral characteristics of the UV source used for maximal utilization of the free radicals. Absorbers could further be used to alter the cure depths based on the process requirements. The mixture of materials is ball milled for about 48 hours to obtain a thoroughly homogeneous suspension.

The second distinction of LAMP is the mechanism used for UV beam projection. The maskless lithography system in LAMP comprises a spatial light modulator (SLM) which is a digital micro-mirror device (DMD) chip. It is an optical chip with more than 1.3 million tiny mirrors. Light from a UV source strikes the DMD chip, and the various mirrors turn on and off selectively according to the pixels in a corresponding black and white bitmap image; in this way, the pattern is projected onto the surface of photocurable ceramic-loaded liquid resin. The resin cures completely with exposures lasting 50~200ms. The optical imaging head, consisting of the UV source and the DMD chip, raster scans the entire exposure region in a serpentine path. After solidification of each successive layer, the build platform moves down by 25-200 microns, according to the slice thickness selected, and the appropriate amount of material is pumped and recoated onto the previously cured layer for the exposure of the next pattern. This exposure mechanism achieves much higher patterning speed than does the conventional SL process, in which a single laser beam is used to raster scan the exposure region point-by-point. After all the layers are built, the polymerized green part is then retrieved from the build platform by draining the excess liquid resin and washing away the uncured resin with appropriate solvents. The cured polymer is then removed by pyrolysis in a binder burnout step, and the ceramic body is further densified to 60-80% relative density through a furnace sintering process.

Currently, the ceramic molds produced through LAMP are applied for investment casting of turbine blades with extremely complex internal cooling passages. A gas turbine, which usually consists of hundreds of turbine blades rotating at very high speeds, takes in large volumes of air, compresses it to high pressure and temperature, mixes it with fuel, and ignites the air-fuel mixture in order to extract power. The inlet gas temperature is much higher than the melting point of the materials used to fabricate the turbine blades themselves, since higher thermodynamic and operating efficiencies can be accomplished for the turbine by elevating the operating temperature. Hence, it is imperative to incorporate efficient and innovative cooling schemes in the turbine blades.

The schematic of a typical state-of-the-art turbine blade with cooling schemes is illustrated in Figure 1.2. Turbine blades are typically made of nickel-based superalloys and other exotic metals which are hard to work mechanically. Thus, the primary method to fabricate these blades is investment casting, also known as lost-wax casting. Figure 1.3 shows a schematic of the current state-of-the-art investment casting process for fabricating turbine blades. Usually, the investment casting process begins with the creation of all the tooling necessary to fabricate the cores, patterns, molds, and setters for casting airfoils, typically involving over a thousand tools for each airfoil [2]. The ceramic core of an airfoil mold is first fabricated through injection molding. The injection molded core is then placed in a “wax die,” and molten wax is injection molded to define the airfoil’s external shape. Next, the wax pattern is subjected to several rounds of ceramic slurry coating, followed by stucco coating to build up shell thickness. After the coating is dried, the mold is dewaxed in an autoclave, and a hollow ceramic shell mold with ceramic cores inside is obtained. The core and shell are fired in a furnace and then molten metal is poured into the shell to form castings. Upon solidification, the ceramic mold is then broken away and the cores removed through chemical etching to provide the final

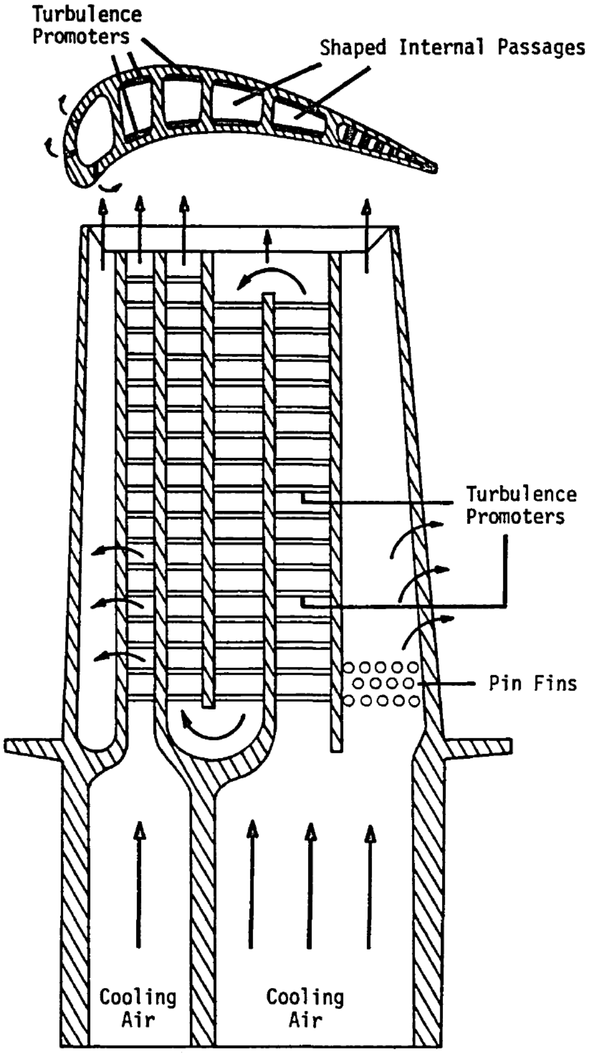

Figure 1.2 Schematic of a typical internally cooled turbine blade [3]

metal castings. Using LAMP, the integral-cored ceramic molds ready for casting can be directly manufactured through a much shorter process chain. All the above discussed conventional tools and processes of lost-wax investment casting can be eliminated, thus improving production yield and reducing associated costs.

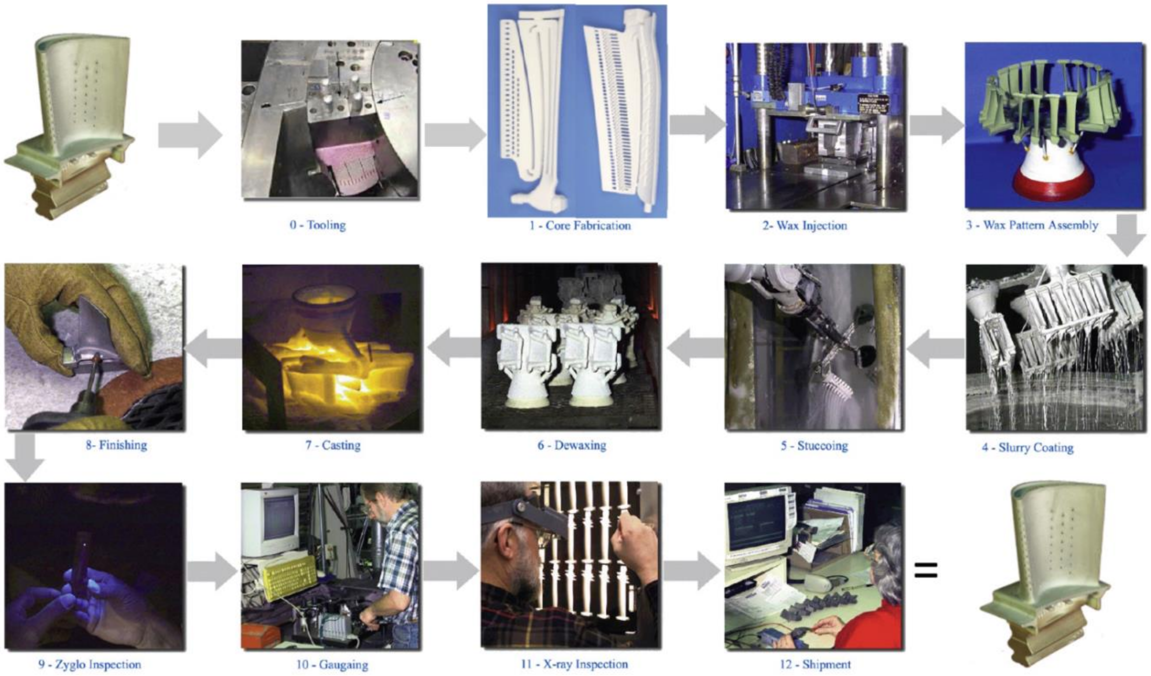

Figure 1.3 Various steps involved in the investment casting of turbine blades (Courtesy Alcoa Howmet)

1.3 Defects Associated with LAMP-built Molds

Defects are part of nearly every foundry's operations, and their causes are various. Investment casting shares these problems, of course, but its defects are largely shell-related, and differ somewhat from other metal casting processes. Among all of the problems with the shell mold, cracking is always the most adverse, as it can result in various defects on the final castings. For instance, a major cause of inclusion defects is mold cracks. If a burned out shell mold has cracked, erosion from the edges of the crack may occur, dispersing refractory particles throughout the casting. Some of the fine and vulnerable structures of the mold might break off due to cracking or delamination during shell firing or metal pouring, and these might become embedded inside the casting to form sub-surface inclusions. The direct defects resulting from shell mold cracks are characterized by lines of positive metal on the casting surface. The length and thickness of these fins are related to the extent of the cracks and delamination. The problem can be even worse when high metallostatic head pressures exist during pouring. In such cases, the metal will penetrate the cracks and deform the thin shell to form a scab on casting's surface. If the crack opening is too large, the shell mold might not be able to hold the poured liquid metal inside and may fail to form a casting. Crack-free ceramic molds are thus highly desired in order to obtain defect-free functional final castings.

1.3.1 Cracks on Molds Built Through LAMP

For ceramic molds made by the LAMP process, interfacial cracks and delamination were frequently observed either in as-manufactured green parts or in final sintered parts. Figure 1.4 shows the typical cracks, visible to the naked eye, appearing on a LAMP built airfoil mold. It can be seen that many small cracks exist in a mold made by LAMP, and through cracks or delamination can even occur in some areas with holes where stress concentrations might occur. On the external surface of an as-manufactured shell mold, it is not easy to see cracks with the naked eye or with optical microscopes. Therefore a line of liquid dye can be applied to the seemingly flawless green body using a cotton swab.

The dye quickly wicks in the same direction as the LAMP layers and away from where the swab contacted the mold, as can be seen in Figure 1.5 [4]. The figure shows that the beginnings of cracks can be found in the green body molds at room temperature. This can be shown clearly in Figure 1.6 [4], where pictures of a mold before and after binder burn-out (BBO) are compared. As seen in this figure, the dye is wicked along the plane of some of the LAMP layers and, after BBO, the cracks that appear visibly are lined up with the layers that wick the dye. This shows that the cracks can be found in the green body molds, and BBO merely reveals the inherent flaws in the mold.

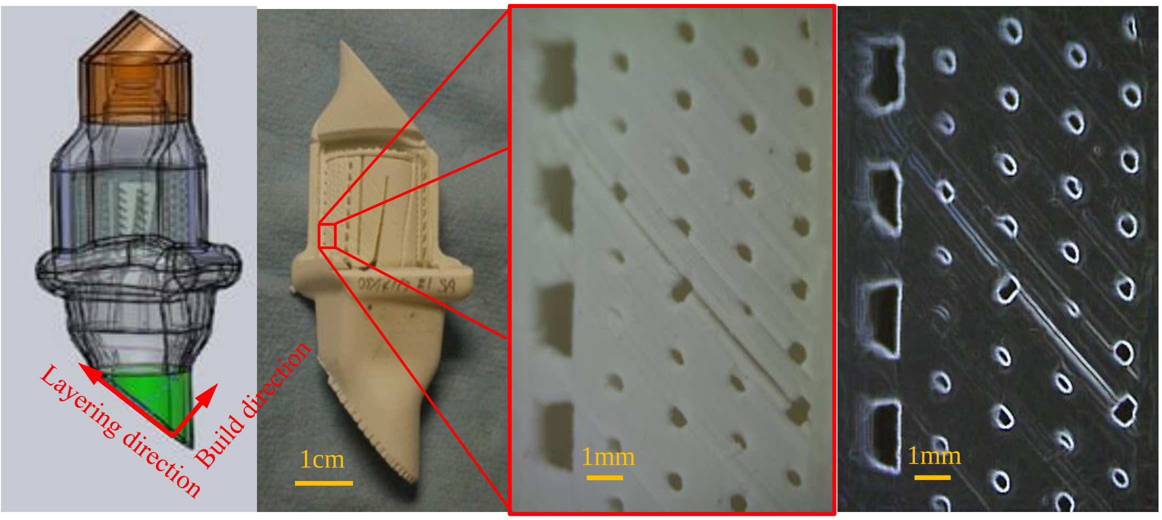

(a) (b) (c) (d)

Figure 1.4 (a) and (b) are the CAD model of airfoil mold and the corresponding green body mold with core built by LAMP, respectively; a close view of the cracks on the mold's surface is shown in (c) and the processed picture is shown in (d).

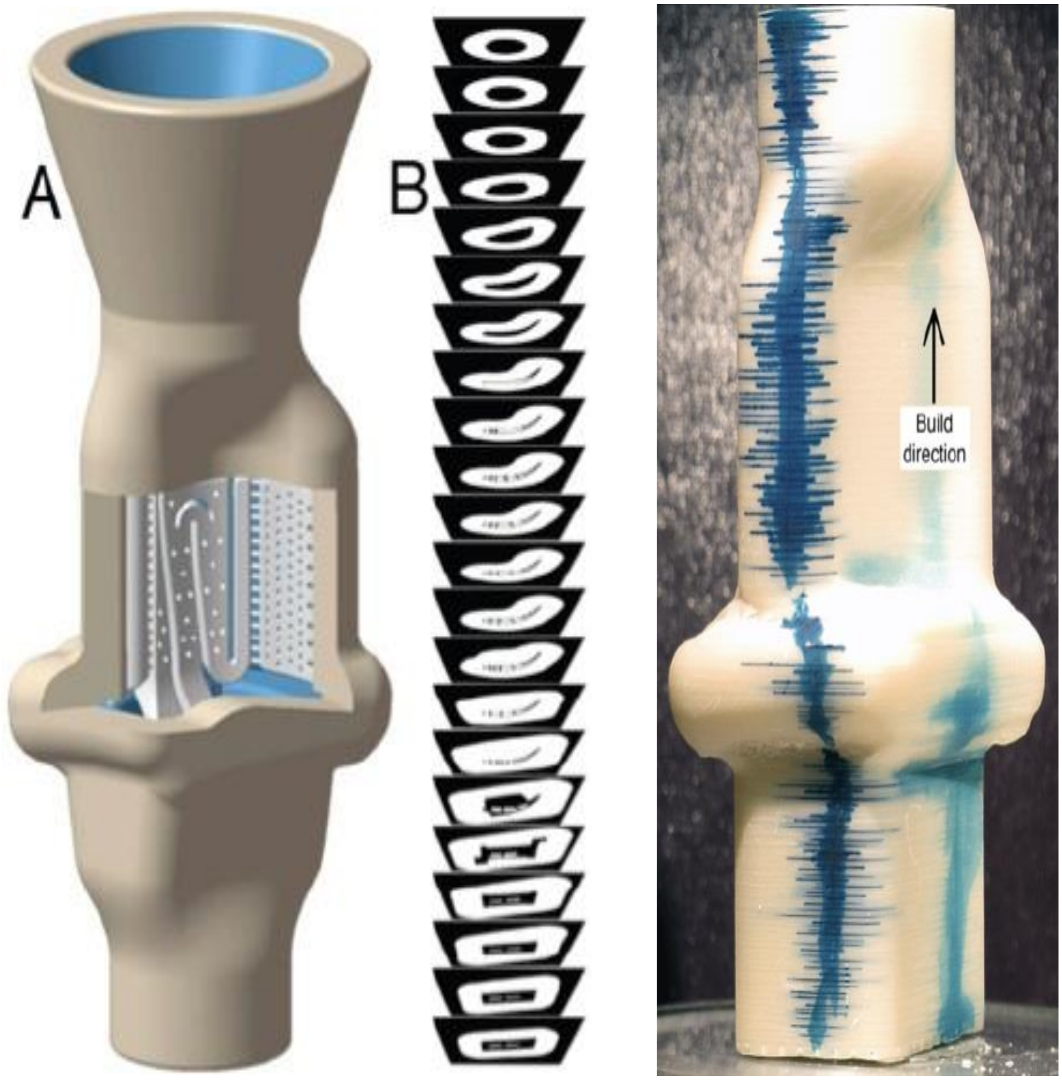

(a) (b)

Figure 1.5 (a) A CAD model of airfoil mold (A) is seen next to its individual sliced layer representation (B), (b) Green body airfoil mold with dye applied. [4]

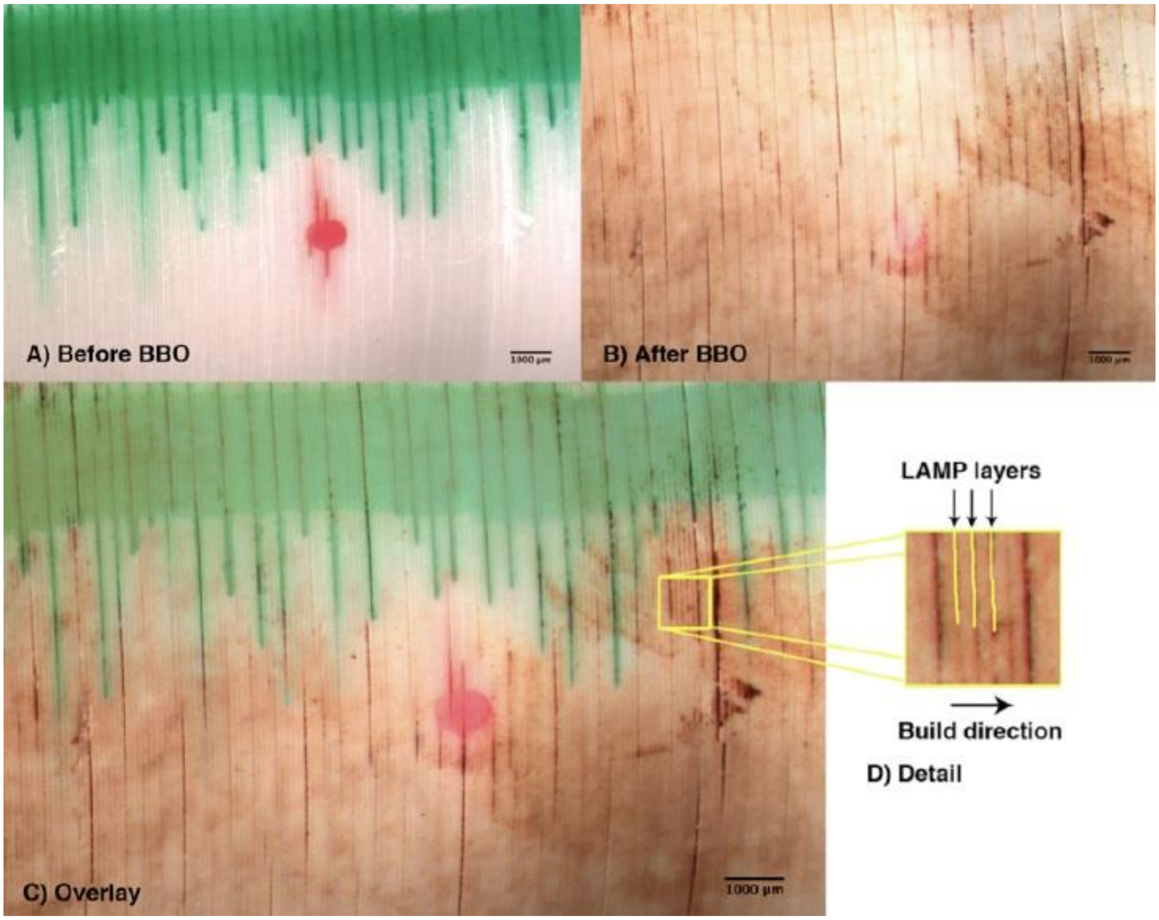

Figure 1.6 Stereomicroscope pictures of mold (a) before BBO, i.e. green body. Red dot is a dot of pen ink used to align the pictures. (b) After BBO. (c) Computer generated overlay of (a) and (b). Note how the green lines of dye in the before image match up with the dark cracks in the after image. (d) Detail of cracks in mold. [4]

1.3.2 Sources of Cracks

The reasons for the appearance of cracks in the green body mold can be many and varied. For instance, in order to wash away uncured monomers and resolve the structural gaps, a clean-up stage is conducted on the as-manufactured mold, using a solvent. During this process, the developer solvent might erode the interface, causing the monomers to dissolve, thereby resulting in interfacial cracks. After clean-up, the green body mold is dried in an environment of room-temperature and yellow light. Drying of the residual uncured monomer is another possible reason for cracking; volumetric shrinkage occurs as the monomer evaporates, and stresses might be induced. In addition to post-fabrication processes, the layer-by-layer fabrication process can also become a source for cracking. The recoating arm might apply a shear force onto the cured layers when each new layer of materials is dispensed over the building area, and this could lead to mode II (in-plane shear) cracking. Despite all of these possible sources for cracking, the primary one considered in this doctoral research is polymerization shrinkage. One of the objectives of this research is to validate the hypothesis that polymerization shrinkage is the main reason for cracks/delamination occurring in the LAMP-built mold, and these defects can be alleviated or eliminated by applying strategies found to be effective in reducing shrinkage-induced stresses and cracks.

1.3.3 Polymerization Shrinkage

Polymerization shrinkage in UV-curable composites is the result of a change in the intermolecular distances of the monomers during photopolymerization. In LAMP, acrylate-based ceramic particle-loaded resins, with added photoinitiators that are sensitive in the range of spectral characteristics of the UV source, form the basis for an ultra-fast photopolymerization reaction. At the start of the reaction, the monomer molecules are separated by the van der Waals distance ($\sim 10^4$Å). As the reaction proceeds, these monomer molecules form a closely packed network, thereby reducing their separation to covalent bond lengths (~1Å), resulting in bulk contraction in the cured resin. The degree of shrinkage is a direct measure of the number of covalent bonds formed. As an additive manufacturing technology, LAMP involves the layer-by-layer building process. Layers of liquid polymer composite are exposed and cured sequentially, according to the slices of the CAD model. The contraction of each newly exposed layer will tend to produce flexure in the layers solidified previously and will thereby result in internal stresses, which accumulate in the layer-by-layer process. This process-induced residual stress can have a significant effect on the quality of the parts by inducing defects such as distortion, cracks and delamination. Thus the objective of this doctoral thesis research is to investigate the mechanisms of stress evolution and crack development so as to infer strategies for alleviating these defects and improving part quality.

1.4 Studies on the Defects Occurring in Additive Manufacturing Processes

1.4.1 Distortions and Residual Stresses in Additive Manufacturing Processes

Rapid prototyping techniques can be classified in terms of the raw material used in the building process. The various material systems and corresponding consolidation mechanisms lead to different causes for residual stress and associated part defects. For processes utilizing metallic powders, such as selective laser melting (SLM), thermal stresses arise in the solidified material due to temperature gradients and shrinkage caused by the solidification of adjacent laser melted material [5]. For processes like stereolithography (SL) and LAMP, in which photopolymerizable liquid materials are cured under exposure of low-power laser or UV light, polymerization shrinkage is the primary reason for accumulating internal stress in parts.

Bugeda et al. [6] developed a finite element model to analyze part distortions during the SL process. This model was implemented and tested in the stereolithography analysis program code developed by the authors. It was assumed that the structural behavior of SL resins can be modeled using a linear elastic model with constant Young modulus and Poisson ratio. The model considered three sources of curl distortion: flexure of the previous part due to solidification of each new layer, overall shrinkage owing to postcuring of whole part, and liberation of the internal forces when the part is separated from the platform. Analysis of a twin cantilever geometry showed that curl distortion grows with the magnitude of volumetric shrinkage and reduces when the layer thickness increases. The analysis also showed that the dependence of curl distortion with respect to volumetric shrinkage is linear only for short parts (less than 6mm). The analysis results showed a good match with the experimental results taken from Jacobs [7].

Evans [8] proposed a mathematical model in which both elastic modulus and cure shrinkage curves were expressed as a function of absorption laser energy and elapsed time to describe the dynamic curing process. In another more complete model proposed by Xu [9], the temperature dependence of the elastic modulus was included, and the change from a glass-like behavior to a soft rubber-like behavior was considered for the polymer when temperature rises above glass transition temperature. Based on these mathematical models, Jiang, Huang and Kuriyama et al. [10-15] developed a dynamic finite element method to analyze curl distortion during the SL process. In this work, the influence of processing parameters such as laser scanning speed, scanning path and slicing thickness on distortion were investigated.

Widemann et al. [16] proposed a method to evaluate photopolymers with respect to the dynamics of polymerization, volumetric shrinkage and sensitivity of polymerization under different process conditions. When a new layer of resin is exposed to the laser, the beam penetrates toward the lower layer, and the lower layer absorbs additional energy until several new layers have been built above it. In Widemann's work, a mathematical model was developed to describe how a bottom layer keeps absorbing energy when new layers are built up.

In all previous finite element analyses, the mechanical properties of cured resin in a single layer were considered to be homogeneous. Based on works done by Widemann [16] and Huang [11], Vatani et al. [17] proposed a new model that included both heterogeneous properties in one single layer and those in adjacent layers. Then, classical lamination theory was used to estimate the final distortion of the SL parts. In this work it was shown that the mechanical property of cured resin is variable and has more influence on the final part distortion especially on thin parts.

1.4.2 Cracks and Delamination Analysis for Additive Manufacturing Processes

Due to the concentration of process-induced stress and relatively weak bonding strength along the interfaces between adjacent layers, cracks and delaminations are frequently observed defects in additive manufactured parts [7, 18].

Beuth and Narayan [19, 20] investigated the residual stress-driven delamination between successively deposited isotropic material layers. The particular process involved was shape deposition manufacturing in which material is deposited onto existing layers in the form of molten metal droplets. Methods were outlined for determining the conservative upper bound for the maximum energy release rate for extending interfacial cracks. These methods were based on potential energy calculations from a residual stress model for an uncracked multi-layer and do not require fracture mechanics modeling.

Alimardani et al. [21, 22] developed a coupled 3D time-dependent finite element model to study the correlation of the temperature distribution and thermal stress fields with the locations of the possible delamination and crack formations across the part. Locations with tensile stress concentrations were indicated to qualitatively determine the propensities to crack formation, and microscopic views of different cross-sections of a thin-wall sample were observed for verification. Preheating the substrate prior to the fabrication process was found to be a feasible method to substantially reduce the cracks formed across the part.

Although cracks and delamination have been found to be significant defects on additive manufactured parts in numerous studies, few researchers numerically or experimentally analyzed the mechanisms of crack/delamination development during the layer-by-layer building process, or worked to develop mitigation strategies for these defects. The work presented in this dissertation is aimed at developing a feasible approach to characterize and predict the delamination process, for application not only in LAMP, but also in other additive manufacturing technologies.

1.5 Dissertation Outline

This dissertation consists of five chapters. A brief outline of the content covered in each of these chapters is given in this section.

Chapter 1 gave an introduction to the background and motivation for the work presented in this dissertation. Various classes of additive manufacturing processes in existence were briefly reviewed. LAMP process is described and, particularly, the characteristics that make it distinct from other additive manufacturing processes were discussed. Then, the motivation for studying the defects, especially cracks, occurring in

LAMP-built parts was given. Furthermore, a literature review of various studies on the defects observed in the other additive manufacturing processes was given.

Chapter 2 presents the elastic model developed for predicting residual stresses and distortions in parts built with LAMP. The evolving double bond conversion of the cured material due to light penetration has been characterized through Fourier Transform Infrared Spectroscopy (FTIR). A theoretical relationship between the polymerization shrinkage strain and the degree of conversion is presented. The material’s elastic modulus, which also evolves with the double bond conversion, has been characterized by three-point bending tests. Finally, a finite element model is developed to predict the residual stresses and distortions in the parts. Experimental validation of this model is also shown.

Chapter 3 focuses on characterizing the Mode I and Mode II interlaminar fracture toughness ($G_{Ic}\ and\ G_{IIc}$) of the LAMP-built laminates. Double cantilever beam (DCB) tests and end notched flexure (ENF) tests have been conducted to characterize Mode I and Mode II fracture, respectively. An overview of the typical data reduction schemes used to compute the values of $G_{Ic}\ and\ G_{IIc}$ is given. A beam theory method and a compliance-based beam method are selected for DCB tests and ENF tests, respectively, and the corresponding computation results are shown.

Chapter 4 develops a mixed-mode cohesive element model to predict the crack initiation and propagation occurring in a LAMP-built part. In this model, the Mode I and

Mode II cohesive parameters, interlaminar strength and penalty stiffness, are determined by matching the numerical load-deflection curves to the experimental ones obtained from the DCB tests and the ENF tests, respectively. Using this model, the fracture of a hollow-cylinder part has been analyzed and the simulation results are compared with experiments.

Chapter 5 investigates several possible strategies to mitigate the shrinkage related defects that may occur in LAMP-built parts. Reducing the overall polymerization shrinkage, optimizing the print-through curve and delaying the gel point of resin composite are found to be effective in reducing stresses and cracks.

Chapter 6 summarizes the work presented in this dissertation, lists the unique contributions made and provides the scope for potential future research.

CHAPTER 2

ELASTIC MODEL FOR PREDICTING RESIDUAL STRESSES AND DISTORTIONS IN LAMP

In LAMP technology, as in many other additive manufacturing technologies, residual stresses are developed during the layer-by-layer building process. One of the outcomes is that curl distortion or geometry deviation occurs in the fabricated parts. In the LAMP process, the photopolymerization shrinkage of each newly exposed layer will tend to produce flexure of the layers solidified previously, i.e. layers beneath, and it thereby leads to internal stresses. As the process of curing sequential layers proceeds, stresses keep evolving and may significantly affect the part quality by inducing defects such as curl distortion, cracks and delamination. In this chapter, an elastic model is established to predict residual stresses and distortions occurring in LAMP-built parts. The objective of this model is to provide a convenient and reasonable approach to analyze the process-induced stresses, alleviate them, and help designers to improve the designs of their parts fabricated through LAMP. To achieve this goal, the details of the composition of the materials used in LAMP are introduced in the first section. Then, Fourier Transform Infrared Spectroscopy (FTIR) is used to study the kinetics of photopolymerization and to measure the double bond conversion degree of the cured material. The polymerization shrinkage strain in each exposed layer can be obtained on the basis of the theoretical relationship between it and the double bond conversion. The next section characterizes the material's elastic modulus, which will be used as an input to the simulation model. In the last part of this chapter, the numerical model, which is based on the characterization of conversion degree and elastic properties of the material, is given to predict stresses and distortions in parts built with LAMP. Experimental validation of this model is also shown.

2.1 Composition of the Materials Used in LAMP

A typical photopolymerizable material composition for LAMP consists of monomers, ceramic particles, dispersant, photoinitiators and absorbers. The LAMP process makes use of a mixture of monomers involving HDDA and EPETA. HDDA is a low volatility, low viscosity monomer, while EPETA is a fast curing monomer. Therefore, a compromise is reached between the ease of dispersal and the curing speed of the resin. Silica particles with 7μm mean diameter, and with 95% of all particles less than 25μm in diameter, are chosen as the filler content. A dispersant such as Variquat CC55 is added to prevent agglomeration of the filler particles. Since monomers in the reaction cannot absorb the UV radiation, it is necessary to add photoinitiators, which do not take part in the photochemical reaction, but can absorb the UV radiation. The photoinitiators transfer the energy thus absorbed to the monomer mixture, thereby forming active initiator radicals which, in turn, initiate the photopolymerization reaction. Therefore, the polymerization reaction rate and cure depth depend greatly on the photoinitiator used. The photoinitiator system is chosen such that it matches the spectral characteristics of the UV source used for maximal utilization of the free radicals. In this study, the commercially available photoinitiator Irgacure 184, from Ciba Inc., is used. Absorbers could further be used to slow down the polymerization rate and alter the cure depths based on the process requirements. The details about the composition of materials used in this study are shown in Table 2.1. Each component is added to the slurry according to the proportion and basis in this table. Volume percentages of all components in the slurry can be calculated based on their densities. The mixture of materials is then ball milled for about 48 hours to obtain a thoroughly homogeneous suspension.

Table 2.1 Composition of the materials used in LAMP

Components	Category	Density (g/cm^3)	Proportion	Basis
Hexanediol diacrylate, HDDA	Monomer	1.02	80-100%	Vol. % of monomer
Ethoxylated Pentaerythritol tetraacrylate, EPETA	Monomer	1.12	0-20%	Vol. % of monomer
Silica	Powder	2.2	55-75%	Vol. % of slurry
Variquat CC55	Dispersant	1.1	0-6%	Wt. % of powder
Irgacure 184	Photoinitiator	1.15	0-10%	Wt. % of monomer
Tinuvin 171	UV Absorber	1	0-2%	Wt. % of monomer

2.2 Photopolymerization Shrinkage

Residual stresses in the LAMP-built parts contribute to the polymerization shrinkage of materials during the curing process. Shrinkage results from the change in the intermolecular distances of the monomers, from the initial state at van der Waals distance (~10^4Å) to the final state at covalent bond lengths (~1Å), during photopolymerization [23]. The degree of shrinkage is a direct measure of the number of covalent bonds formed. Thereby, the polymerization shrinkage strain can be obtained, given the conversion degree of the resin, which can be measured experimentally through FTIR.

2.2.1 Photopolymerization Kinetics

In this subsection, the fundamentals of photopolymerization kinetics at various stages of the polymerization reaction are discussed. Goodner and Bowman [24] developed a comprehensive model based on the three primary reaction mechanisms occurring during the polymerization: initiation, propagation and termination. This model also incorporates both primary radical termination and inhibition, as shown in Figure 2.1. Figure 2.1 (a) represents the photolysis of initiator, I, to give two primary radicals, $R\bullet$. Figure 2.1 (b) is the second step, chain initiation process, where a primary radical reacts with the monomer, M, to form a unit-length polymer chain, $P_1\bullet$. The reaction rate is determined by the kinetic constant for chain initiation, $\mathrm{k_i}$. Figure 2.1 (c) represents the re-initiation of inhibited chains, where an inhibited chain, $P_nZ\bullet$, reacts with the monomer to form an actively growing chain. The kinetic constant for chain re-initiation, k_i', is usually several orders lower than k_i in magnitude for most polymer systems. Figure 2.1 (d) gives the propagation reaction of a growing chain with the kinetic constant k_p. Two mechanisms exist for the chain termination process. Through bimolecular termination, given by Figure 2.1 (e), two growing radical chains can react to form either one polymer chain (by combination) or two polymer chains (by disproportionation), with the kinetic constant k_t. In the second termination mechanism, represented by Figure 2.1 (f), a primary radical reacts with a growing polymer chain to form a dead polymer, and the corresponding kinetic constant is k_{tp}. Figure 2.1 (g) represents the chain inhibition process, in which an inhibitor species, Z, such as an oxygen molecule or an intentionally added inhibitor, reacts with a growing chain to form a relatively unreactive species. The corresponding kinetic constant is k_z.

Initiation

$$I \xrightarrow{h\nu} 2R\bullet \qquad \text{(a)}$$

$$R\bullet + M \xrightarrow{k_i} P_1\bullet \qquad \text{(b)}$$

$$P_n Z\bullet + M \xrightarrow{k_i'} P_{n+1}\bullet \qquad \text{(c)}$$

Propagation

$$P_n\bullet + M \xrightarrow{k_p} P_{n+1}\bullet \qquad \text{(d)}$$

Termination

$$P_n\bullet + P_m\bullet \xrightarrow{k_t} P_{n+m}/P_n + P_m \qquad \text{(e)}$$

$$P_n\bullet + R\bullet \xrightarrow{k_{tp}} P_n \qquad \text{(f)}$$

Inhibition

$$P_n\bullet + Z \xrightarrow{k_z} P_n Z\bullet \qquad \text{(g)}$$

Figure 2.1 Schematic of the photopolymerization process [24]

2.2.2 Cure Depth Model

After the slurry is thoroughly mixed and ready to be used for LAMP, a cure depth measurement is usually conducted to characterize the curing capability of the material. The cure depth measurement is based on a cure depth model, which is same as the Jacob's model commonly used in Stereolithography [7]; it is derived from the Beer-Lambert's law. The Beer-Lambert's law postulates that the light energy dose attenuates exponentially with respect to the distance traveled in a medium, according to the following equation

$$E(z) = E(z=0) * e^{-\frac{z}{D_p}} \qquad (2.1)$$

where $E(z)$ is the energy dose as a function of the distance z traveled through the medium, and $E(z=0)$ is the energy dose at the surface of the medium. D_p is called penetration depth and is treated as the property of the specific composition of the material. Mathematically, D_p denotes the distance z where the energy dose at the surface, $E(z=0)$, attenuates by a factor of e^{-1}. Another parameter E_c, the critical energy dose, is introduced in order to develop an expression for the cure depth, C_d. E_c is also considered as a property of the medium; it denotes the minimum energy dose required to initiate the photopolymerization chain reaction in the photocurable suspension. Thereby, it is assumed that the slurry just begins to gel and forms a soft solid when energy dose reaches E_c. And, if energy dose is above E_c, the suspension is increasingly cured into a solid. Thus, the cure depth is given by the distance z beneath the surface of the slurry at which an energy dose of E_c is received. Derived from the Equation (2.1),

$$E_c = E(z = C_d) = E(z = 0) * e^{-\frac{C_d}{D_p}} \tag{2.2}$$

is obtained. It can be rearranged to give

$$C_d = D_p * \ln\left(\frac{E}{E_c}\right) \tag{2.3}$$

The above equation is referred to as the working curve equation of a given material system, and it can be used to determine the energy dose required to cure a layer of given thickness, C_d. The energy dose can be expressed as $E = I * t$, where I is the constant light intensity of the lamp and t is the exposure time. Hence

$$C_d = D_p * \ln\left(\frac{I * t}{E_c}\right) \tag{2.4}$$

Therefore, the cure depth C_d is a function of the penetration depth D_p, the critical energy dose E_c, the lamp intensity I and the exposure time t. The lamp intensity cannot be changed during the LAMP process and is measured as a constant before each build. If the two material parameters, D_p and E_c, are given, then the required exposure time could be determined for a desired cure depth. The procedure for experimentally determining D_p and E_c is described in the next subsection.

2.2.3 Determination of D_p and E_c

The material constants D_p and E_c of a specific material system are determined experimentally by making a plot of the cure depth, C_d, versus the natural logarithm of energy dose, $I * t$. This plot is a linear regression of the experimental cure depth measurements and is known as the working curve. To obtain the measurements needed to plot the working curve, cure depth samples need to be prepared; this is shown in Figure 2.2. In this schematic, a UV transparent glass slide was placed on the surface of the slurry, and the exposure head introduced a uniform intensity of UV light onto the slurry. The intensity of the UV light was measured to be $0.84 W/cm^2$ by a power meter. The exposure dose was adjusted by selecting exposure times between $100ms$ and $550ms$ to get cured samples of various thicknesses. The cured samples adhered to the glass slide, and the residual monomer was rinsed from the slide and samples with isopropyl alcohol (IPA). The IPA was allowed to evaporate, and the samples were dried after the development procedure. Then, each of the samples was measured using a micrometer to get its thickness, i.e. cure depth. These measurements were linear regressed to obtain the working curve. A typical working curve for the material system used in LAMP (detailed composition was given in Table 2.1) is shown in Figure 2.3. From the working curve, D_p was determined as the slope of the linear fit and E_c was obtained from the intercept. For the material with formulation shown in Table 2.1, the penetration depth D_p was $209\mu m$ and the critical energy dose was found to be $82mJ/cm^2$. With these two parameters known, and given a desired cure depth, the corresponding required exposure time was calculated by Equation (2.4).

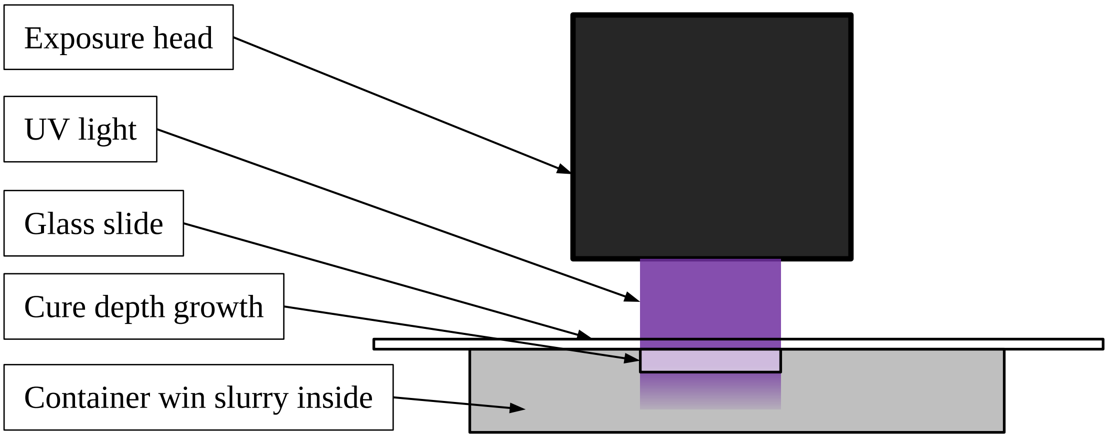

Figure 2.2 Schematic of the experimental setup for the determination of cure depth (The size of exposure head is scaled)

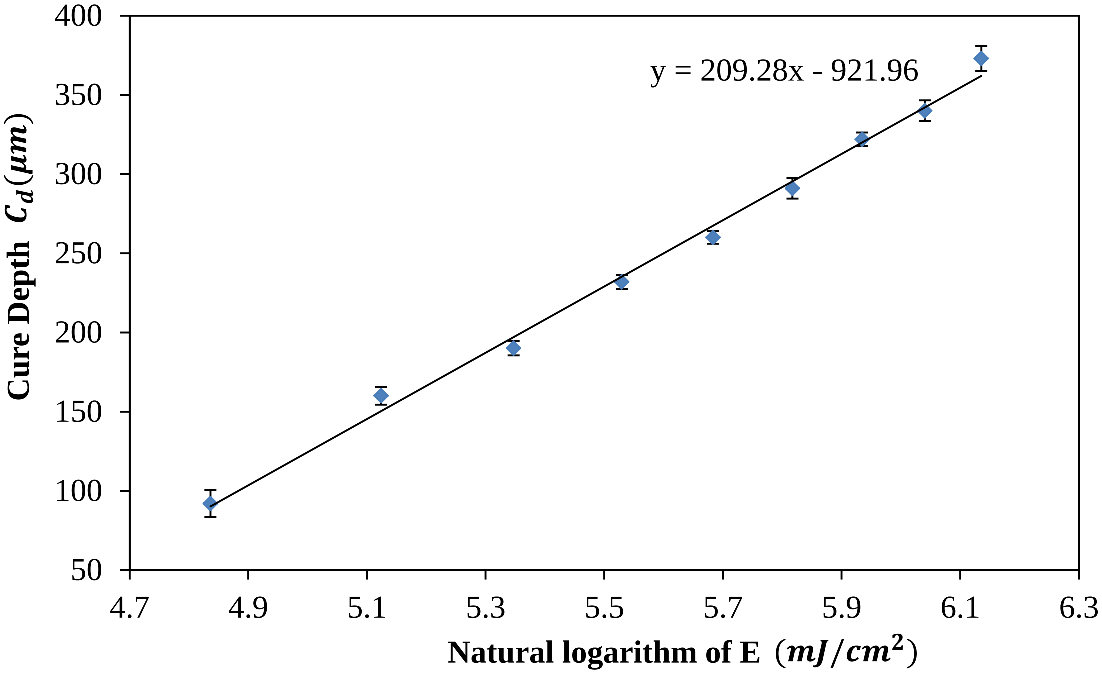

Figure 2.3 Working curve obtained from cure depth measurements for the material system used in LAMP

2.2.4 Fourier Transform Infrared Spectroscopy (FTIR) for Measuring the Degree of Conversion

Fourier Transform Infrared Spectroscopy (FTIR) is an analytical tool which can be used to determine various chemical species and bonds in a molecule. It is one of the most powerful tools for monitoring UV curing processes that proceed within a fraction of a second. It allows a rapid and quantitative measurement of the conversion of specific reactive functional groups under varying conditions such as exposure dose, photoinitiator concentration and coating thickness. For LAMP, it can realize the quantification of the acrylate double bond conversion in the cured resin and thereby the extent of polymerization shrinkage can be estimated. Usually, the FTIR equipment can be operated with different setups and in different modes, i.e. transmission mode, reflection mode and ATR mode. In this dissertation, all of the measurements for degree of conversion were made by FTIR operated in attenuated total reflectance (ATR) mode, which is illustrated in Figure 2.4. The sample is held by a pressure device and in contact with an ATR crystal (made of germanium in this study). Reflected by several mirrors and the crystal, an infrared (IR) beam is made to strike the sample. The depth of penetration by the IR beam (typically several microns) usually depends on the wavelength, refractive index of the sample and crystal, and the angle of incident radiation. Attenuated by the sample, the IR beam is led to a detector, where a spectrum, that is unique to a specific composition (like “finger print”), can be obtained. Thereby, the chemical species and bonds in the sample can be analyzed and quantified.

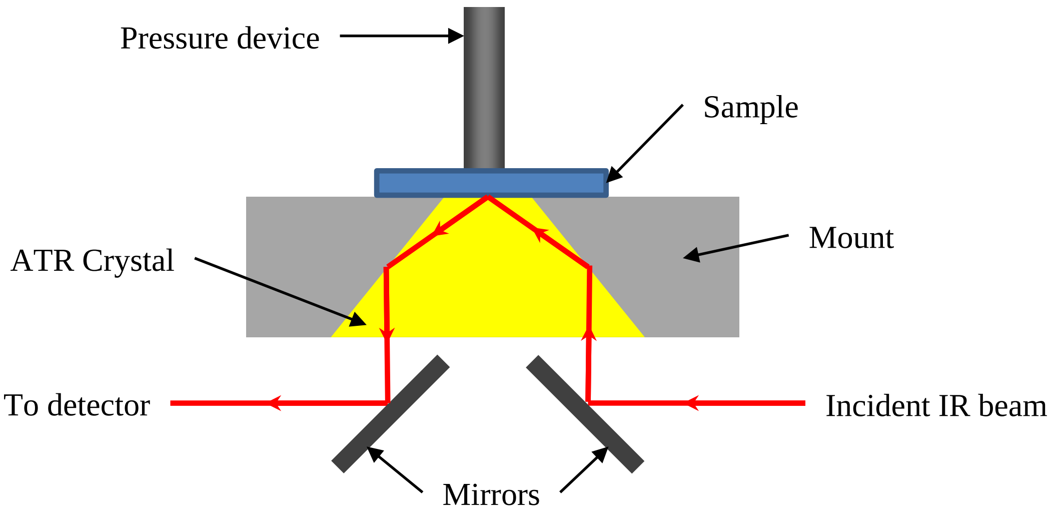

Figure 2.4 Schematic of FTIR operated in attenuated total reflectance (ATR) mode

The carbon double bond conversion takes place by means of stretching and twisting during the polymerization of acrylate monomers [25]. As shown in Figure 2.5, stretching is sensitive at the 1610-1640cm^{-1} wavenumbers while twisting is sensitive at the 1405-1415cm^{-1} wavenumbers. In this figure, the spectra are obtained with different exposure times; thereby the conversion of double bonds during photopolymerization is captured as a function of the exposure time (or energy dose). Peak heights go down and flatten out when the exposure time is increased, indicating that the reaction proceeds and the carbon double bonds (C=C) in acrylate monomers are consumed to form the polymer chains. In order to quantify the amount by which the carbon double bond peak reduces, comparison with a standard peak which does not change with respect to exposure time is necessary. For the acrylate monomer, the carbon oxygen bond (C=O) at around

$1750 cm^{-1}$ wavenumber is taken as the reference peak since C=O does not participate in the reaction and its peak remains constant.

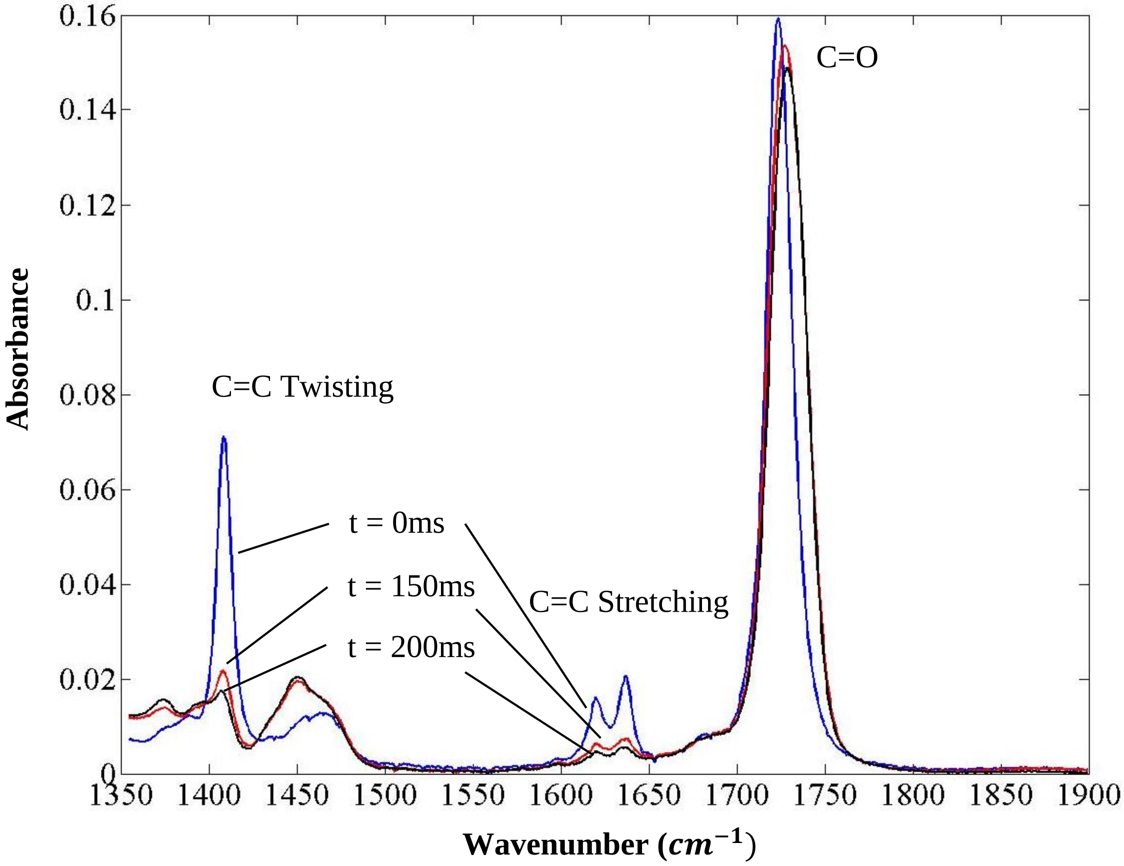

Figure 2.5 FTIR spectra of slurry used in LAMP with different exposure times

Therefore, the degree of conversion $\alpha(t)$ can be obtained through Equation (2.5).

$$\alpha(t) = \frac{\left[\frac{Area_{1625} + Area_{1410}}{Area_{1750}}\right]_0 - \left[\frac{Area_{1625} + Area_{1410}}{Area_{1750}}\right]_t}{\left[\frac{Area_{1625} + Area_{1410}}{Area_{1750}}\right]_0} \times 100\% \qquad (2.5)$$

where $Area_{1625}$, $Area_{1410}$ and $Area_{1750}$ represent the areas beneath the spectrum in the plot, corresponding to the peaks of C=C stretching, C=C twisting and C=O respectively. The subscript “0” means that the suspension is not exposed while subscript “t” means curing with exposure time t.

2.2.5 Print-through Mediated Incremental Curing

Due to light penetration through the upper layers, almost all of the layers, except for the topmost ones, are incrementally cured as subsequent layers above them are being exposed. This phenomenon is referred to as print-through. For each layer, the print-through phenomenon will keep occurring for several successive layers until the final conversion degree is reached and no further changes take place. Print-through can result in good layer-to-layer bonding. However, additional curing due to light penetration at the bottom layer from several layers above results in accumulation of internal stresses and warping of the fabricated part. Thus, it is desirable to characterize the print-through process and determine the extent to which a particular layer is being cured additionally due to this phenomenon. Figure 2.6 shows a schematic where a stair-shaped sample was fabricated to characterize the print-through phenomenon. In the sample, each layer was $100\mu m$ thick and was cured with a constant exposure time. The bottom layer can be divided into eleven regions at which different numbers of subsequent layers were swept and exposed from above. Five samples were built using five different exposure times, each of which corresponds to the cure depth of 120μm, 150μm, 200μm, 250μm and 300μm respectively. The material composition has been shown in Table 2.1. D_p and E_c for this material system, and the exposure times used are given in Table 2.2. For each sample, FTIR analyses were conducted in the eleven regions with different layers above them at the bottom layer. After the spectra were obtained, the degrees of conversion were calculated with Equation (2.5). For each region, five measurements were made, and the values of conversion degrees were averaged. The results are shown in Figure 2.7.

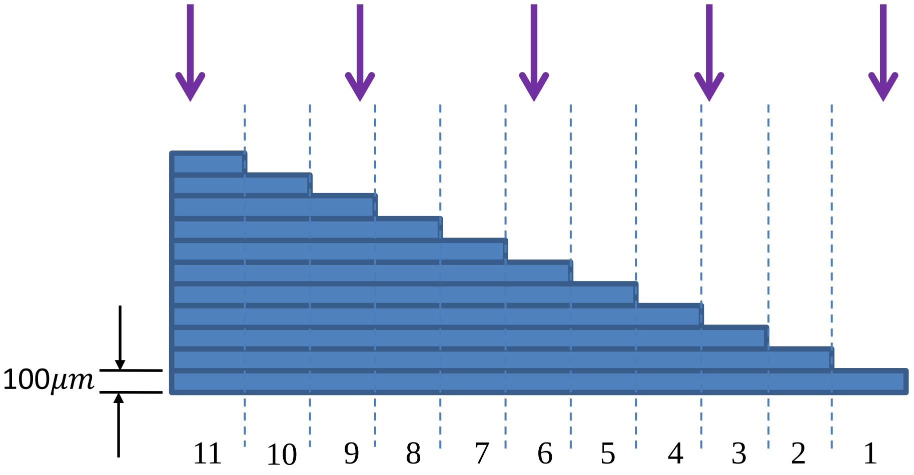

Figure 2.6 Print-through mediated incremental curing at the bottom layer due to exposures of layers above it

Table 2.2 Exposure parameters used in LAMP

Parameters					
$D_p(\mu m)$	209				
$E_c(mJ/cm^2)$	82				
Cure depth $C_d(\mu m)$	120	150	200	250	300
Energy dose(mJ/cm^2)	145	168	213	270	343
Exposure time(ms)	173	200	254	322	409

It can be seen from Figure 2.7 that, for cure depths of 200-300μm, the degrees of conversion at the bottom layers continuously increase up to approximately 4 exposed layers above, while for cure depth of 150μm, the degree of conversion at the bottom layer keeps going up for about 5 layers of exposure. When cure depth is 120μm, the degree of conversion at the bottom layer comes to a plateau after 6 layers are exposed above. Thereby, the potential to additionally cure the layers underneath is higher when cure depth is smaller or, equivalently, the energy dose of each exposure is less. However, the final value of conversion degree increases with increasing cure depth, which can be shown in Table 2.3. The final value is obtained through averaging the conversion degrees at the plateau of each print-through curve. The print-through curve demonstrates the change in conversion as subsequent layers are swept and exposed from above and thus it will be used as an input to the numerical model in this study.

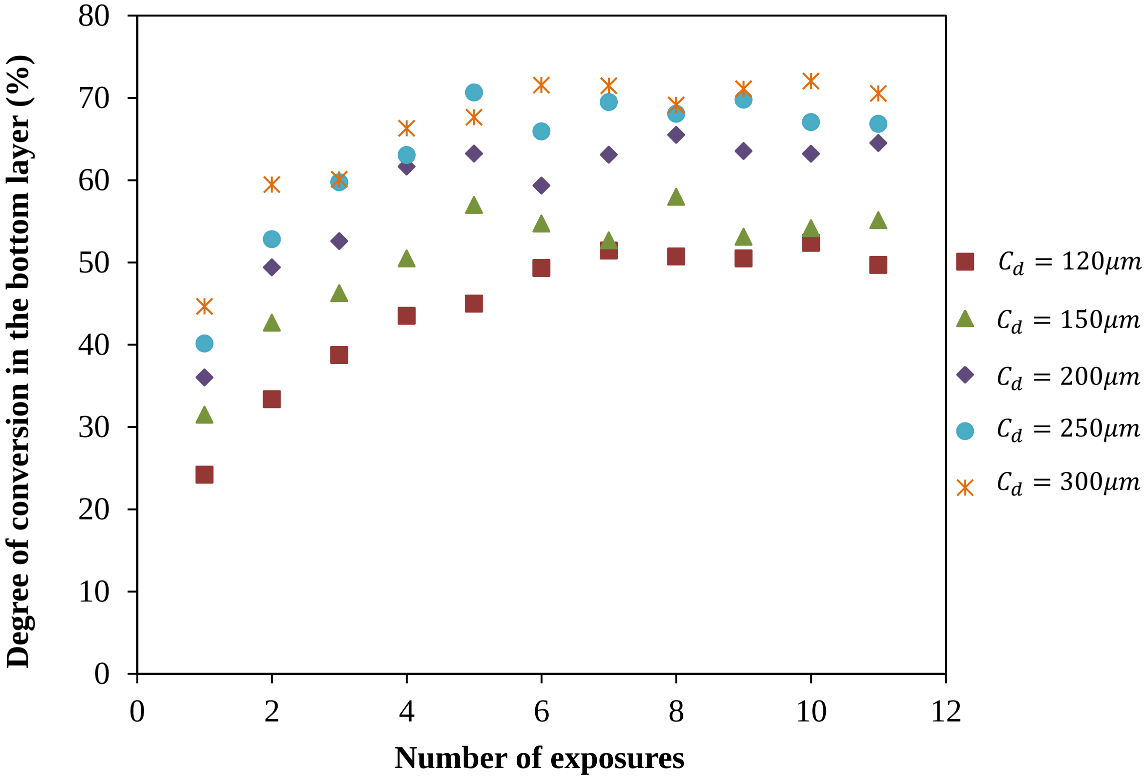

Figure 2.7 Conversion in the bottom layer vs. number of exposures above the bottom layer

Table 2.3 Final values of conversion degree at the bottom layer

Cure depth $C_d(\mu m)$	Final degree of conversion (%)
120	50.95
150	54.97
200	63.01
250	68.27
300	70.98

2.2.6 Gel Point

During photopolymerization process, the resin composite is transformed from a viscous fluid to an elastic gel at the gel point. Before the gel point, stress might be negligible since the material in pre-gel state can flow between the free surfaces and the bonded surface in a newly exposed layer. As viscosity of the developing polymer is still low, shrinkage stress can thus be rapidly compensated. At gel point, a space-spanning, load-bearing network forms, and stress starts to develop at the layer interface since the newly exposed material is constrained by adhesion to the solid layers beneath. Therefore, in the numerical model, it is assumed that the shrinkage taking place during the pre-gel phase does not cause stress buildup.

There have been several methods for characterizing the gel point of resin composites. Fano et al. [26] proposed that the maximum shrinkage strain rate of resin composites occurs at gel point, because that auto-acceleration of polymerization rate is due to “gel effect” [27]. At gel point, shrinkage strain rate is at its highest value because polymerization shrinkage is hindered by the build-up of three-dimensional networks of polymer chains [28], resulting in a dramatic change in mechanical properties. As a resin composite material gels, forces build up within the material. Thus, Visvanathan et al. [29] and Gao et al. [28] proposed polymerization shrinkage force as an indirect measure of gel point, and that gel point is arbitrarily defined as the time when a force threshold of a certain value is exceeded. All these methods need complex experimental setup and instruments. In this study, it is simply assumed that gelation occurs at the conversion degree of 20% (a little lower than the smallest value of conversion degree, 24.2%, obtained from the FTIR measurement conducted).

2.2.7 Theoretical Relationship Between Polymerization Shrinkage and Degree of Conversion

The volumetric shrinkage occurring during the LAMP process is related to the photopolymerization mechanism. The linkage of small monomer units produces large polymer chains, and the corresponding intermolecular spacing is reduced from Van der Waals distance to covalent bond (C=C) lengths. This results in density changes and thus bulk contraction in the cured resin, which accumulates as the part is fabricated layer-by-layer. Thus, the volumetric shrinkage is a direct measure of the number of covalent bonds formed (degree of conversion), and an exact semi-empirical relationship can be derived. Experimentally, the volume change per mole of acrylate groups (C=C) is reported to be $22.5\, cm^3/mol$ [30] when the acrylate monomer is polymerized. The molar volume of HDDA is

$$\frac{M_m}{\rho_m} = \frac{226}{1.02} = 221.57 cm^3/mol \tag{2.6}$$

where M_m is the molecular weight and ρ_m is the density of the monomer. Since HDDA is a diacrylate, which means that there are two acrylate groups (C=C) in one molecule, an estimate of volumetric shrinkage of fully cured (i.e. 100% conversion) HDDA can be given by

$$\frac{2 \times 22.5}{221.57} \times 100 = 20.31\% \tag{2.7}$$

The theoretical calculation method employed here is based on group (i.e. C=C) contributions, and it results in a value of shrinkage very close to the reported value 22.1% obtained through experimental approaches, such as the reflective laser beam scanning method [31]. In the more general case of multiacrylates with filler particles, the number of moles of functional groups present in volume V is

$$f \times \frac{V\rho_m}{M_m} \times \left(1 - \frac{FL}{100}\right) \tag{2.8}$$

where f represents the functionality of the monomer and FL is the filler loading in percentage. Hence, the number of moles of functional groups converted in volume V is

$$\alpha \times f \times \frac{V\rho_m}{M_m} \times \left(1 - \frac{FL}{100}\right) \tag{2.9}$$

where α is the degree of conversion in the monomer. The percentage relative change in volume, i.e. volumetric shrinkage, is

$$\frac{\Delta V}{V}(\%) = 22.5 \times \alpha \times f \times \frac{\rho_m}{M_m} \times \left(1 - \frac{FL}{100}\right) \times 100 \tag{2.10}$$

For a mixture of monomers of any functionality, and with ceramic filler particles, the volumetric shrinkage can be estimated through the following equation [32]:

$$\frac{\Delta V}{V}(\%) = 22.5 \times \alpha \times \frac{\sum_i (f_i \chi_i)}{\sum_i (M_{mi} \chi_i)} \rho_{mix} \times \left(1 - \frac{FL}{100}\right) \times 100 \tag{2.11}$$

where f_i is the functionality of monomer (i), χ_i is mole fraction of monomer (i),

M_{mi} is molecular weight of monomer (i) and ρ_{mix} is density of the monomer mixture. For the material system investigated in this dissertation, the values of all parameters are shown in Table 2.4.

Table 2.4 Values of parameters used to determine the volumetric shrinkage

Components	f_i	M_{mi}	ρ (g/cm^3)	v/o (%)	w/o (%)	χ_i	ρ_{mix} (g/cm^3)
Hexanediol diacrylate, HDDA	2	226	1.02	27.9	15.8	0.95	1.03
Ethoxylated Pentaerythritol tetraacrylate, EPETA	4	528	1.12	3.1	1.9	0.05	
Filler (ceramic powder)			2.2	65	79.7		

The value of volumetric shrinkage is calculated to be about 7.05% with the parameters in Table 2.4 substituting into Equation (2.11). Assuming a uniform strain contraction for all principle strain components and considering the volumetric strain to be smaller than 10 percent, the value of linear shrinkage strain is approximately one third of the volumetric shrinkage value. Thus the linear shrinkage strain ε_T can be expressed as

$$\varepsilon_T = \frac{1}{3} \times 22.5 \times \alpha \times \frac{\sum_i (f_i \chi_i)}{\sum_i (M_{mi} \chi_i)} \rho_{mix} \times \left(1 - \frac{FL}{100}\right) \times 100 \qquad (2.12)$$

The series of equations above does not involve some of the components in the slurry, i.e. dispersant, photoinitiator and UV absorber, because they are only very small portions compared to monomers and filler particles. Equations (2.9)-(2.12) embody the expectation that the volumetric shrinkage is proportional to the degree of conversion in the monomer systems, and they will be used to describe the linear contraction strain in the numerical model of this study.

2.3 Characterization of the Cure-dependent Elastic Modulus

In this section, the change of Young's modulus with respect to the degree of conversion in the cured material is investigated. Both theoretical and experimental approaches are explored to describe the cure-dependent modulus of the resin.

2.3.1 A Theoretical Model for Cure-dependent Elastic Modulus

For the ceramic particle-loaded resin composite used in LAMP, the mechanical properties are assumed homogeneous and isotropic in one layer, and the Poisson's ratio (ν) is assumed constant. The elastic modulus of the resin is strongly cure dependent, i.e. it relies on the conversion degree (α) of the resin. The prediction of the Young's modulus of polymer composite materials has been studied by several researchers. Dillman and Seferis [33] developed a model to quantitatively describe the dynamic modulus as a function of both the viscoelastic and kinetic intrinsic behavior of the polymeric system. Prasatya and Simon [34] developed a similar thermo-viscoelastic model to describe the time, temperature and conversion dependence of the modulus for thermosetting material during cure. However, these rigorous models were proposed particularly for thermosetting material, and they require the evaluation of several kinetic and viscoelastic parameters which need extensive experimental data. Therefore, they are not suitable for LAMP. Bugeda et al. [6] developed a finite element model for simulating the structural behavior of stereolithography resins by using a linear elastic model with constant Young's modulus. However, this does not conform to the reality that modulus is conversion dependent. Xu [9] developed a mathematical model, in which the elastic modulus was expressed as a function of absorbed laser energy and elapsed time, to describe the dynamic curing process for photopolymerizable material used in stereolithography. However, unlike stereolithography, LAMP can be modeled as a quasi-static process, because each layer is scanned in a square-by-square manner instead of point-by-point, and the whole liquid resin area is cured in a short period of time. Therefore, a more convenient α-mixing rule model [35, 36] is used here to obtain the cure-dependent modulus. The instantaneous isotropic resin modulus, denoted by E_0, is expressed explicitly as a function of conversion degree α:

$$E_0 = (1-\alpha)E_{\alpha 0} + \alpha E_{\alpha 1} + \gamma\alpha(1-\alpha)(E_{\alpha 1} - E_{\alpha 0}) \tag{2.13}$$

where $E_{\alpha 0}$ and $E_{\alpha 1}$ are the Young's moduli of uncured $(\alpha = 0)$ and fully cured $(\alpha = 1)$ resin, respectively. The parameter γ $(-1 \leq \gamma \leq 1)$ is introduced to quantify the competing mechanisms between stress relaxation and chemical hardening [35]. Increasing γ will make the modulus increase more rapidly at a relatively low conversion degree. The modulus of the uncured resin can be chosen arbitrarily small due to the negligible stiffness. Thus, only the modulus of fully cured resin is needed to characterize the elastic modulus with respect to conversion degree. Hence, this equation is simple and easy to use for numerical simulations when a cure-dependent modulus is needed in the model. However, it is very difficult to obtain a cured sample with 100% conversion, especially for the highly loaded ceramic suspension used in LAMP. Thus, Equation (2.13) is modified to

$$E_0 = \left(1 - \frac{\alpha}{\alpha_m}\right) E_{\alpha 0} + \frac{\alpha}{\alpha_m} E_{\alpha \mathrm{m}} + \gamma \frac{\alpha}{\alpha_m} (1 - \frac{\alpha}{\alpha_m})(E_{\alpha \mathrm{m}} - E_{\alpha 0}) \tag{2.14}$$

where $\mathrm{E}_{\alpha 0}$ and $\mathrm{E}_{\alpha \mathrm{m}}$ are the Young's moduli when $\alpha = 0$ and $\alpha = \alpha_m$, respectively. The quantity α_m is the maximum degree of conversion that can be achieved in LAMP, which is 71% for the ceramic suspension tested in this study, according to Table 2.3.

The material used in LAMP is a composite of silica particles and photocurable resin. The effective bulk modulus $\overline{K}$ of this composite can be derived according to the self-consistent method [37], shown in Equation (2.15)

$$\overline{K} = K_0 + \frac{c_1 (K_1 - K_0)(3\overline{K} + 4\bar{\mu})}{3K_1 + 4\bar{\mu}} \tag{2.15}$$

where K_0 and K_1 are the bulk moduli of matrix (resin) and inhomogeneity (particle) respectively. The quantity $\bar{\mu}$ is the effective shear modulus of the composite and c_1 is the volume fraction of particle loading. The silica particles can be considered rigid (over 70GPa) compared to the resin, thus we obtain

$$\bar{K}=\frac{3K_0+4c_1\bar{\mu}}{3(1-c_1)} \tag{2.16}$$

The quantity $\bar{\mu}$ can be expressed as a function of $\bar{K}$ and the effective Poisson's ratio ν, which is considered constant here.

$$\bar{\mu}=\frac{3\bar{K}(1-2\nu)}{2(1+\nu)} \tag{2.17}$$

Substituting into Equation (2.16), we obtain

$$\bar{K}=\frac{1+\nu}{1+\nu-3c_1+3\nu c_1}K_0 \tag{2.18}$$

The relation between bulk modulus and Young's modulus can be expressed as

$$\bar{K}=\frac{\bar{E}}{3(1-2\nu)}\ ,\ K_0=\frac{E_0}{3(1-2\nu)} \tag{2.19}$$

Using Equations (2.18) and (2.19), we obtain the effective Young's modulus of the composite as a function of the resin's modulus E_0, effective Poisson's ratio ν and particle volume fraction c_1.

$$\bar{E}=\frac{1+\nu}{1+\nu-3c_1+3\nu c_1}E_0 \tag{2.20}$$

It can be seen that the effective modulus is proportional to the resin's modulus. This argument can also be seen in empirical or semi-empirical equations used to predict the modulus of particulate-polymer composites [38] when the volume fraction of particles is fixed. Thus, similar to Equation (2.14), the effective modulus of the composite is also related to the conversion degree α of the resin:

$$\bar{E} = \left(1 - \frac{\alpha}{\alpha_m}\right)\bar{E}_{\alpha 0} + \frac{\alpha}{\alpha_m}\bar{E}_{\alpha m} + \gamma\frac{\alpha}{\alpha_m}(1 - \frac{\alpha}{\alpha_m})(\bar{E}_{\alpha m} - \bar{E}_{\alpha 0}) \tag{2.21}$$

where $\bar{E}$, $\bar{E}_{\alpha 0}$, $\bar{E}_{\alpha m}$ are the moduli of the ceramic particle-loaded composite, not the pure resin. Therefore, if an elastic testing specimen is built through LAMP, and if its final conversion degree α_m and Young's modulus $\bar{E}_{\alpha m}$ are measured, the moduli with respect to other values of conversion degree can be determined by Equation (2.21).

2.3.2 Experimental Characterization for Cure-dependent Elastic Modulus

Various testing methods are available for the measurement of elastic modulus, among which tensile testing and bend testing are most popular. The bending test should preferentially be used with brittle materials, for which tensile tests are difficult [39]. Therefore, a three-point bending test is used in this subsection to measure the elastic modulus of the material, since the parts made by LAMP are of brittle nature. A schematic of the three-point bending test is shown in Figure 2.8. The experimental tests were performed using uniform rectangular bars horizontally positioned between two supports.

The specimens were subjected to a vertical force applied midway between the supports. The test machine was operated in a displacement control mode with a constant crosshead rate of $5\mu m/s$ and was not stopped until the testing specimens were broken.

Five groups of specimens were built using five different exposure times, corresponding to the cure depths of 120μm, 150μm, 200μm, 250μm and 300μm respectively. The material composition has been shown in Table 2.1 and the five exposure times used are given in Table 2.2. Each group corresponds to a value of conversion degree, which has been determined by FTIR analysis and is given in Table 2.3. Hence, after post-processing the data obtained from the three-point bending tests for each group of specimens, the change in the modulus with respect to the degree of conversion can be obtained.

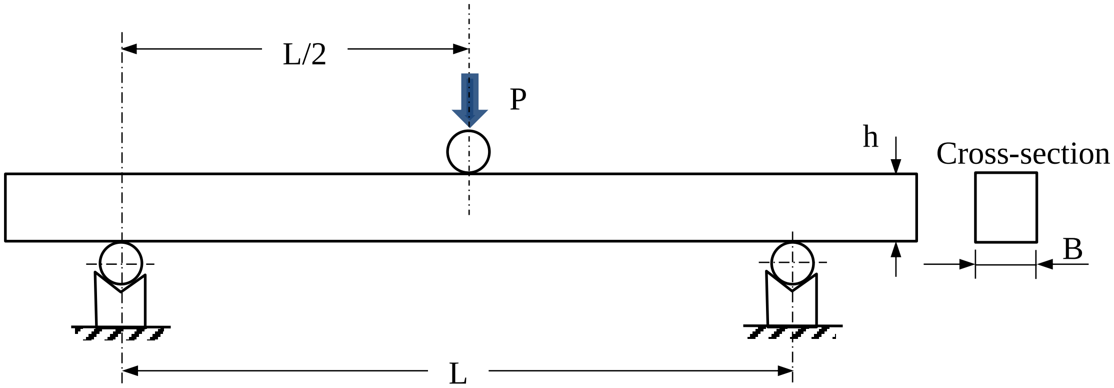

Figure 2.8 Three-point bending test to determine Young's modulus of the material

A typical load versus deflection ($\mathrm{P}-\delta$) curve obtained by three-point bending test is shown in Figure 2.9. The linear portion of this curve is fitted, and the slope of the fitted line can be used to determine the Young's modulus of the material using the following equation:

$$E=\left(\frac{P}{\delta}\right)\cdot\frac{L^3}{48I} \qquad (2.22)$$

where L is the span or the distance between supports, I $(=Bh^3/12)$ is the inertial moment of the cross-sectional area and P/δ represents the slope of the straight-line portion of the load-deflection curve. The dimensions of the specimens were not exactly the same, and they were measured with micrometer. For each specimen, the width, B, is about 3 millimeters and the height, h, is around 7 millimeters (70 layers). The span, L, is always 27 millimeters.

The Young's modulus, computed by Equation (2.22), versus the degree of conversion for five groups of specimens with different cure depths (exposure times) are illustrated in Figure 2.10. The modulus rises with increasing degree of conversion, as expected, and it rises more rapidly at a relatively high conversion degree. In the graph, an exponential curve is given by fitting the data points.

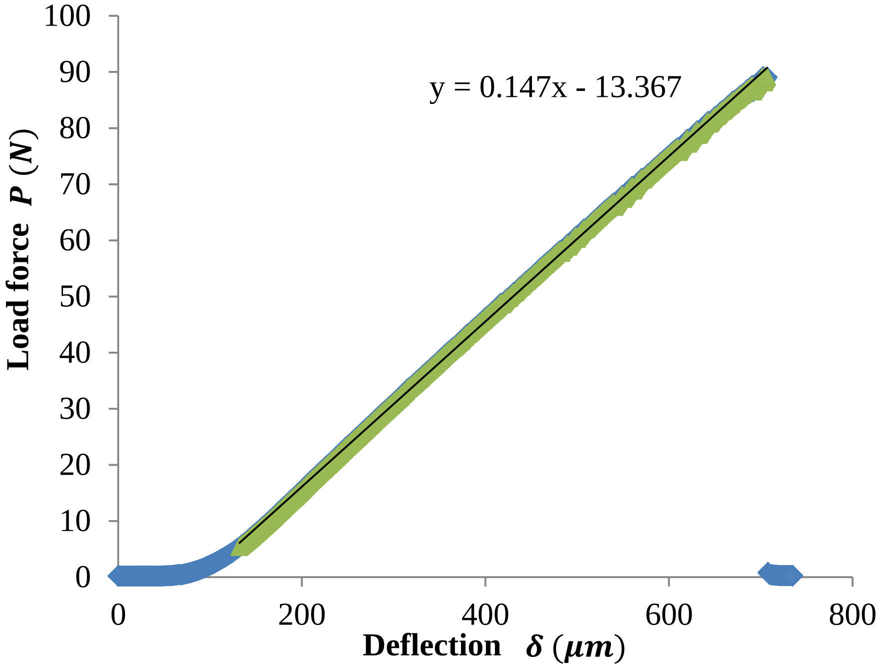

Figure 2.9 A typical load-deflection $(P - \delta)$ curve for three-point bending test

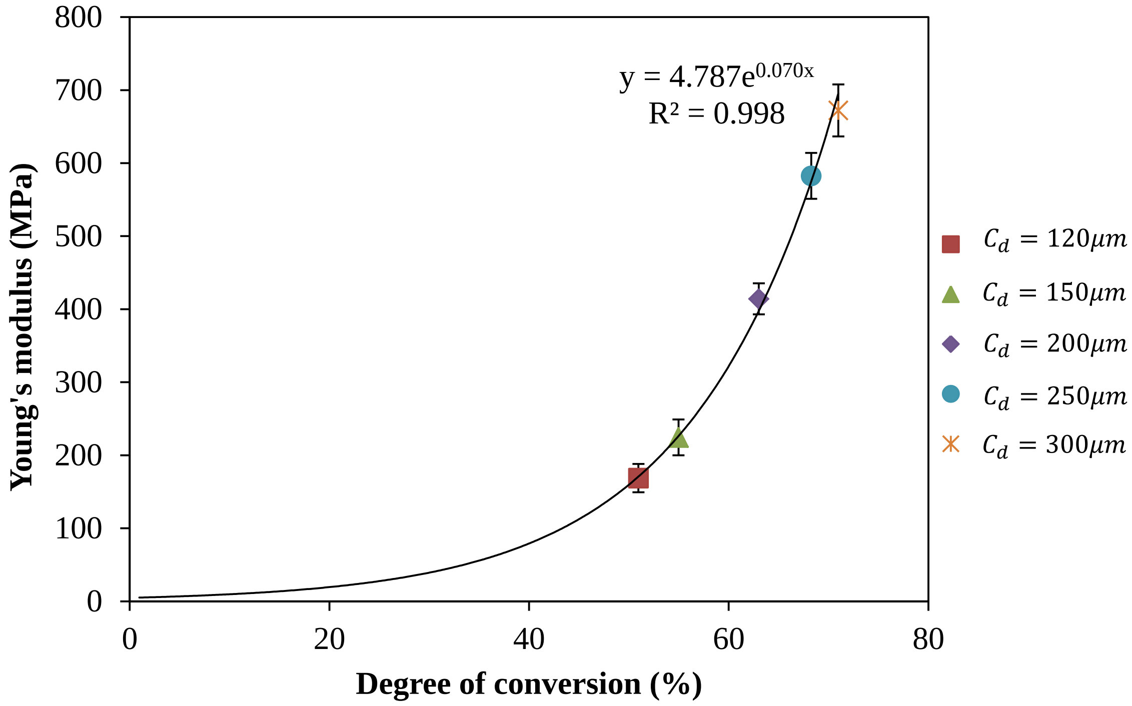

Figure 2.10 Young's modulus vs. final conversion degree of the specimen

In Figure 2.11, the experimental data are compared with the theoretical curves obtained by Equation (2.21). The parameter γ in the equation takes values of 0 and -1 for the two theoretical curves respectively. When γ equals to zero, the theoretical curve is a straight line, which is not appropriate since it cannot capture the characteristic that modulus increases much more rapidly at a higher conversion degree. When the value of γ is negative one, the theoretical curve becomes a quadratic curve, and the modulus rises faster as the conversion degree approximates bigger values. However, γ cannot be smaller than -1, therefore the theoretical curve cannot become even steeper (as steep as the experimental curve) when the conversion degree is high. Hence, the experimentally obtained data for the cure-dependent modulus will be used in the numerical simulation instead of the theoretical Equation (2.21).

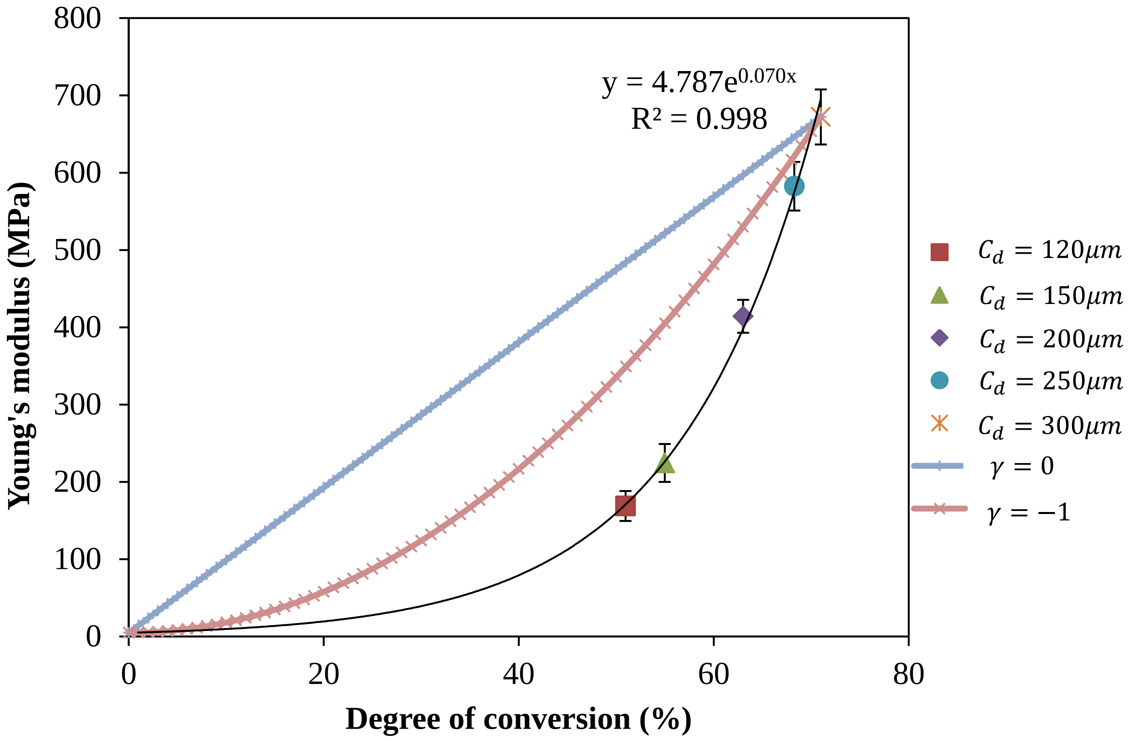

Figure 2.11 Experimental data compared with the theoretical curve for cure-dependent modulus

The flexural strength (modulus of rupture), which is a measure of the ultimate strength of a beam in bending, can also be obtained by post-processing the results of the three-point bending test. In the ASTM standard C1161 [40], the formula for the strength, S, of a beam in three-point flexure is given as follows:

$$\mathrm{S} = \frac{3PL}{2Bh^3} \tag{2.23}$$

Shown in Figure 2.12, the flexural strength is also cure dependent, and its value changes with the degree of conversion in a similar pattern as does the elastic modulus. This figure also demonstrates that the scattering of data for the strength is bigger than that for the modulus. This is due to the fact that the material of the specimen is brittle and thereby the randomly appearing small flaws on the surface of specimen may affect its strength.

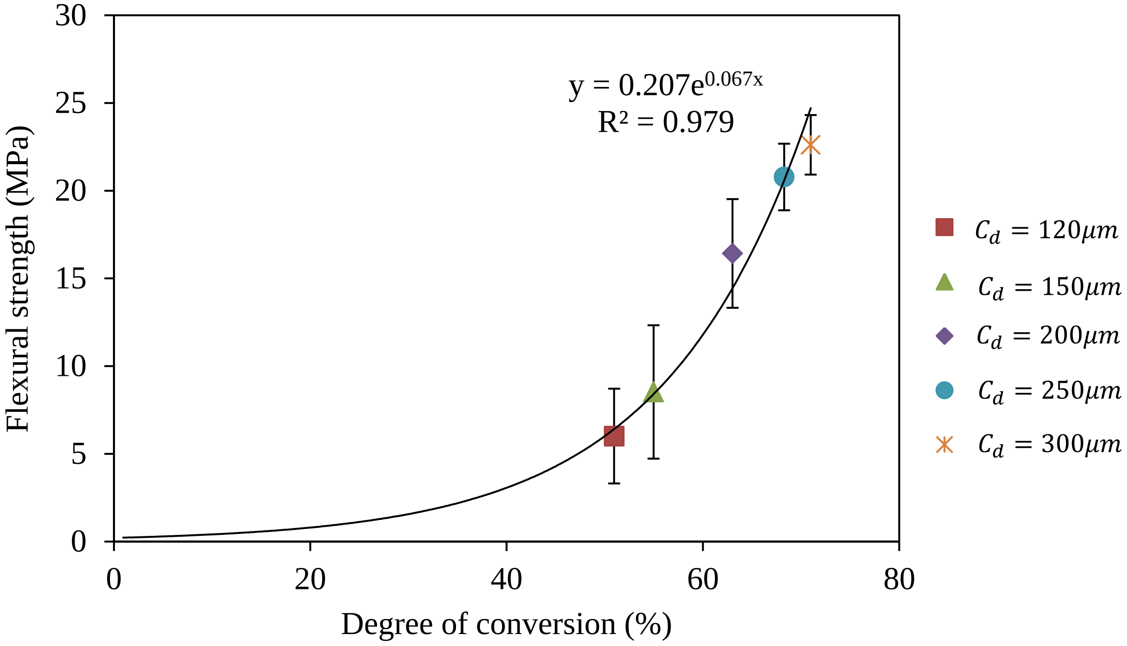

Figure 2.12 Flexural strength vs. final conversion degree of the specimen

2.4 Numerical Simulation of Residual Stresses and Distortions for LAMP

Finite element analyses (FEA) are conducted to simulate the evolution of internal stresses and distortions using the commercial FEA software package, ABAQUS. To simulate the LAMP process, the degree of conversion, cure-dependent modulus and the shrinkage strain are made to be the three primary inputs for the numerical model, as shown in Figure 2.13. The user subroutine UFIELD is used to define the field of conversion degree, upon which the elastic modulus depends, and to realize the print-through process. Another user subroutine UEXPAN is used to make the shrinkage strain a function of the degree of conversion. Furthermore, the model change command of ABAQUS is used to remove and, sequentially, reactivate the elements of each layer, so as to simulate the layer-by-layer manufacturing process. Therefore, the initial liquid meshes can be pre-constructed, but without any solidification properties. In other words, all the liquid meshes consist of dead (deactivated) elements until the liquid is cured. Before each new layer of elements is reactivated, the coordinates of the nodes are updated according to the deformation of cured layers. The flow chart for this numerical model is illustrated in Figure 2.14.

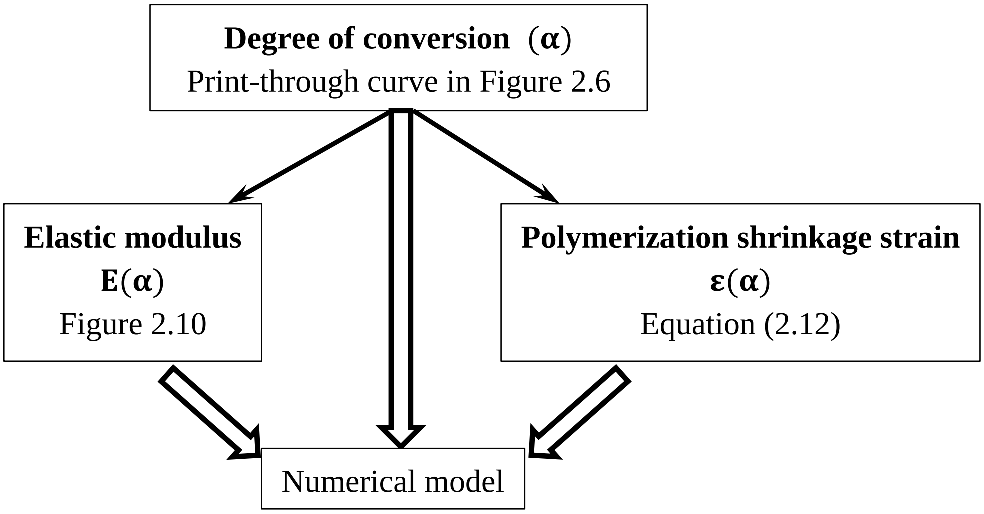

Figure 2.13 Schematic showing the inputs to the numerical model

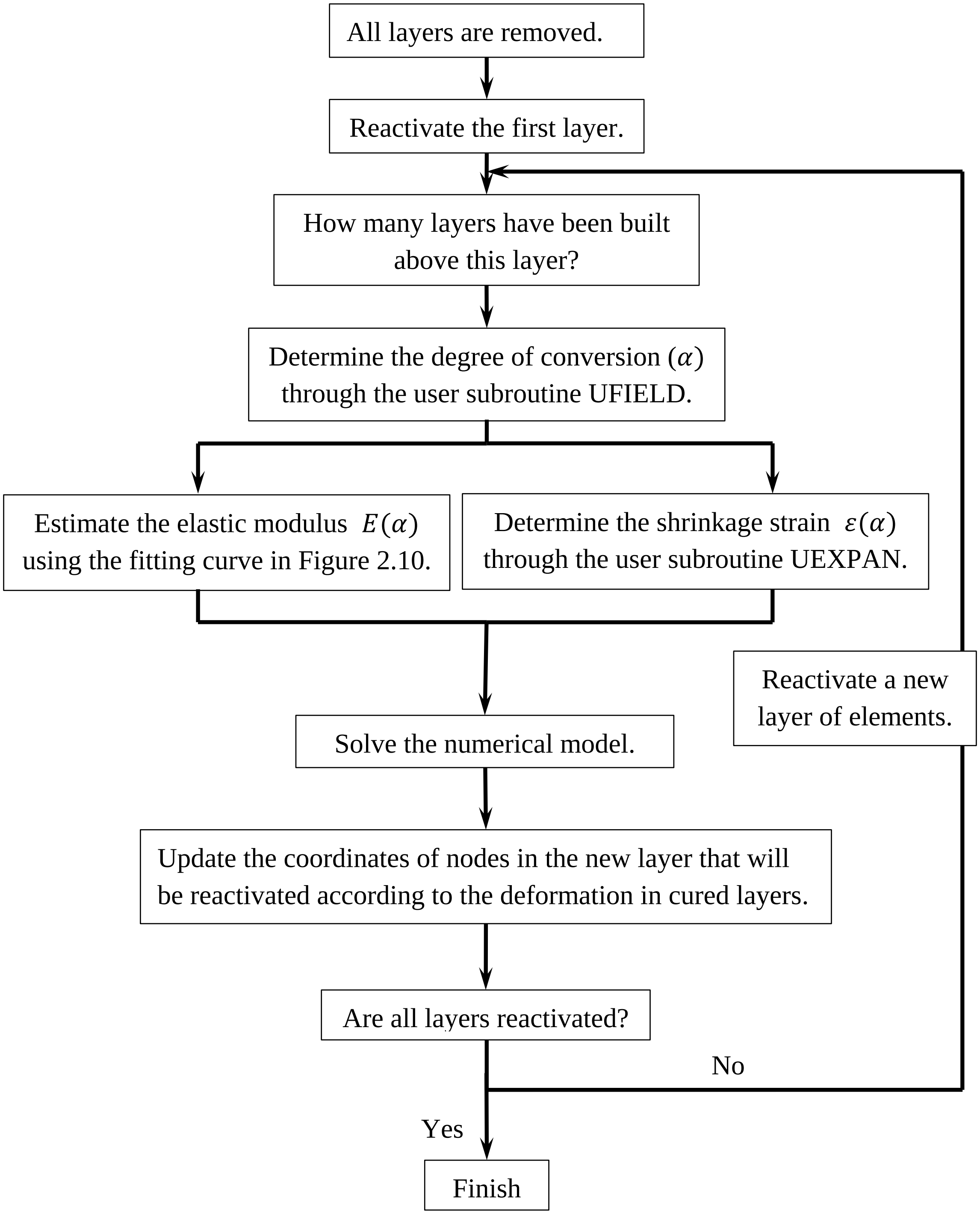

Figure 2.14 Flow chart for the numerical model

In a 3D model, element type C3D20 (20-node quadratic brick) can be mainly used because of its good precision in simulating stress concentration scenarios. However, a few of C3D8 (8-node linear brick) and C3D8R (8-node linear brick, reduced integration) elements may need to be used in some positions to avoid serious distortions of elements. In order to save computation time, simulations are conducted using a 2D finite element model in this section. In the 2D model, four-node quadratic plane strain elements (CPE8) are used. Mechanical properties corresponding to different conversion degrees of the material used in the model are provided in Table 2.5. All of the numerical simulations in this study are conducted with the processing parameter C_d (cure depth) equal to $200\mu m$.

Table 2.5 Cure-dependent mechanical properties used in the numerical model

Number of layers above	0 (1st exposure)	1	2	3	4	>4
Degree of conversion (α)	36.0%	49.4%	52.6%	61.6%	63.0%	63.0%
Young's modulus (MPa)	59.5	152.0	190.2	357.1	393.8	393.8
Poisson's ratio (ν)	0.367					

In order to evaluate its ability to simulate the residual stresses and distortions occurring in LAMP-built parts, the numerical model is used to simulate the warped part in the bridge curvature method (BCM). BCM is a pragmatic method used in several studies [5, 41] to assess the internal stresses in additive manufacturing processes in a simple, fast and still accurate way. As illustrated in Figure 2.15, for using the BCM, a bridge-like part has to be built on a base plate. When the test part is cut off the base plate, the bridge curls because of the relaxation of internal stresses. The planes at the bottom of the pillars of the bridge deviate from their normal position and form a curling angle, β, which is indicative of the residual stresses. Notice that only the residual tensile stresses in the x-direction at the top middle of the part (i.e. at the bridge overhang) cause the bending. The value of β is used as a measure for the amount of stresses in the part after fabrication. Furthermore, BCM can be useful for comparing stress magnitude and for selecting possible build strategies and parameters to reduce stress levels during the layered manufacturing process.

By using BCM, specimens were built through LAMP with the dimensions given in Figure 2.15. The number of layers in the bridge overhang ranges from 10 to 60, and each layer is 100μm thick (thus the height ranges from 1 to 6mm). For each height, a group of five test parts was produced, and for each test part, the curling angle was measured on both sides of the part by using an optical microscope, as shown in Figure 2.16. The results of the measured angles for all specimens are shown in Figure 2.17.

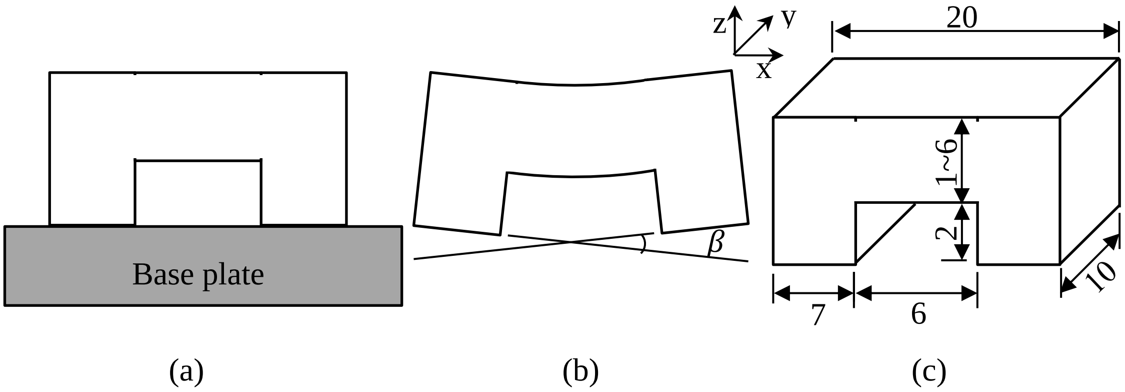

(a) (b) (c)

Figure 2.15 Schematic of the BCM method for identifying the residual stresses in the test parts. (a) Before, and (b) after removal from base plate. (c) Dimensions of the test parts [mm].

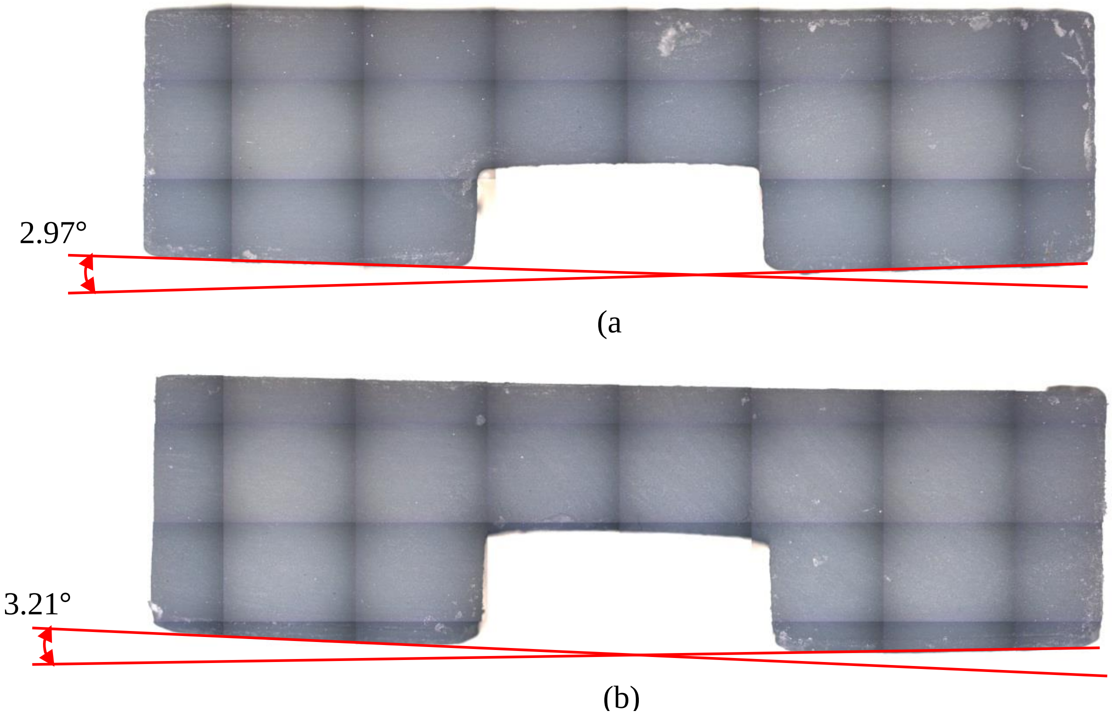

(a

(b)

Figure 2.16 Pictures taken from the font (a) and back view (b) of one specimen (bridge overhang is 3mm thick) with measured angles

A 2D plane strain half symmetric finite element model of the BCM test part is created, as shown in Figure 2.18. The symmetric boundary conditions are applied to the left edge of the model and the nodes at bottom surface are constrained in all degrees of freedom in the steps that simulate the layer-by-layer building process. In the last step, the boundary at the bottom surface is removed, representing that the part is released from the base plate on which it is built. The mechanical properties and dimensions used in this model are given in Table 2.5 and Figure 2.15, respectively. The simulation results for a BCM test part with 3mm thick bridge overhang are shown in Figure 2.19. The curling angles, β, for BCM test parts with different bridge overhang thicknesses obtained from simulations are plotted together with experimental results in Figure 2.17.

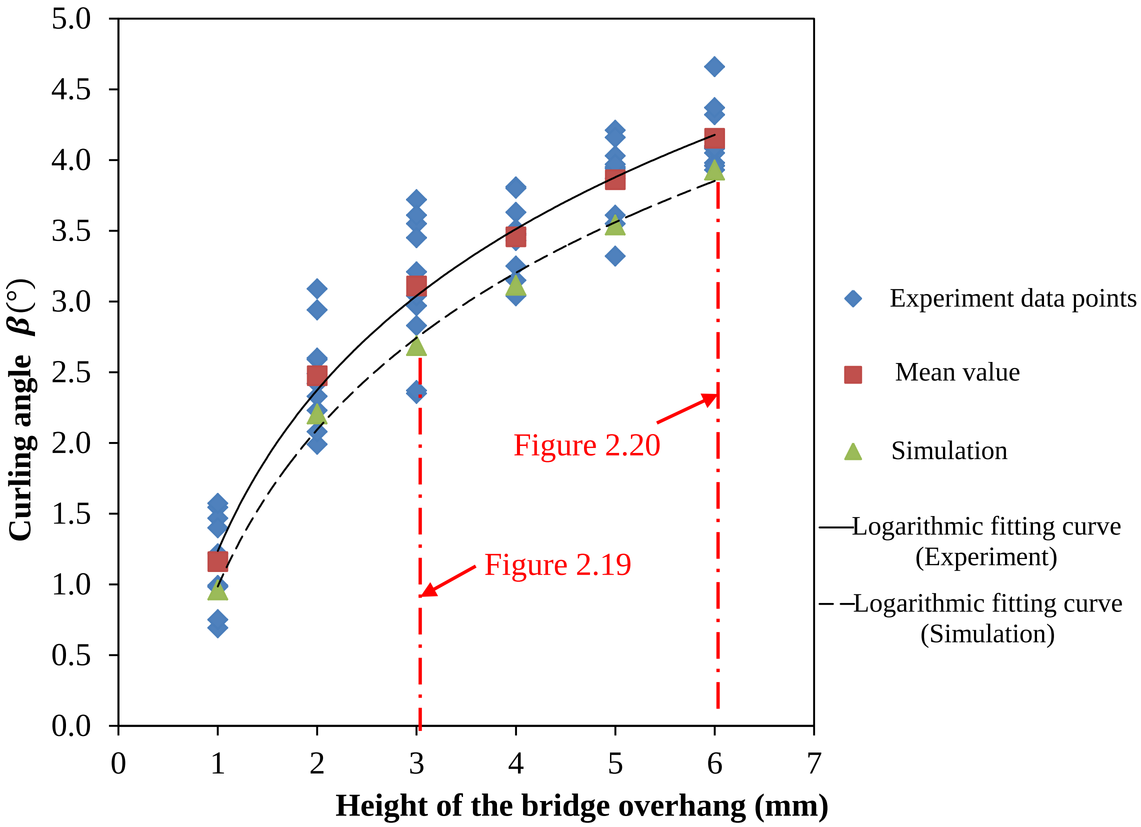

Figure 2.17 Comparison of experiment and simulation results for BCM

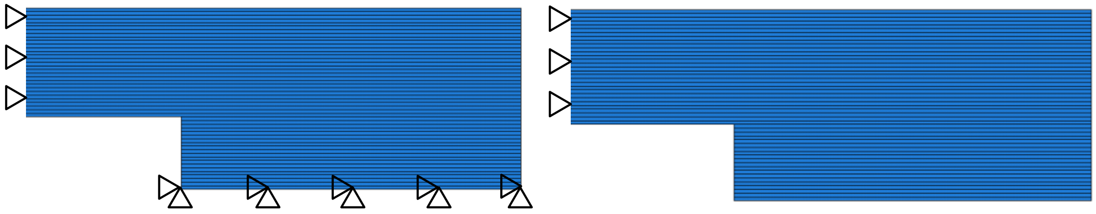

(a) (b)

Figure 2.18 2D plane strain half symmetric finite element model of the BCM test part (a) during the fabrication process and (b) when releasing it from the base plate on which it is built. The boundary conditions are shown.

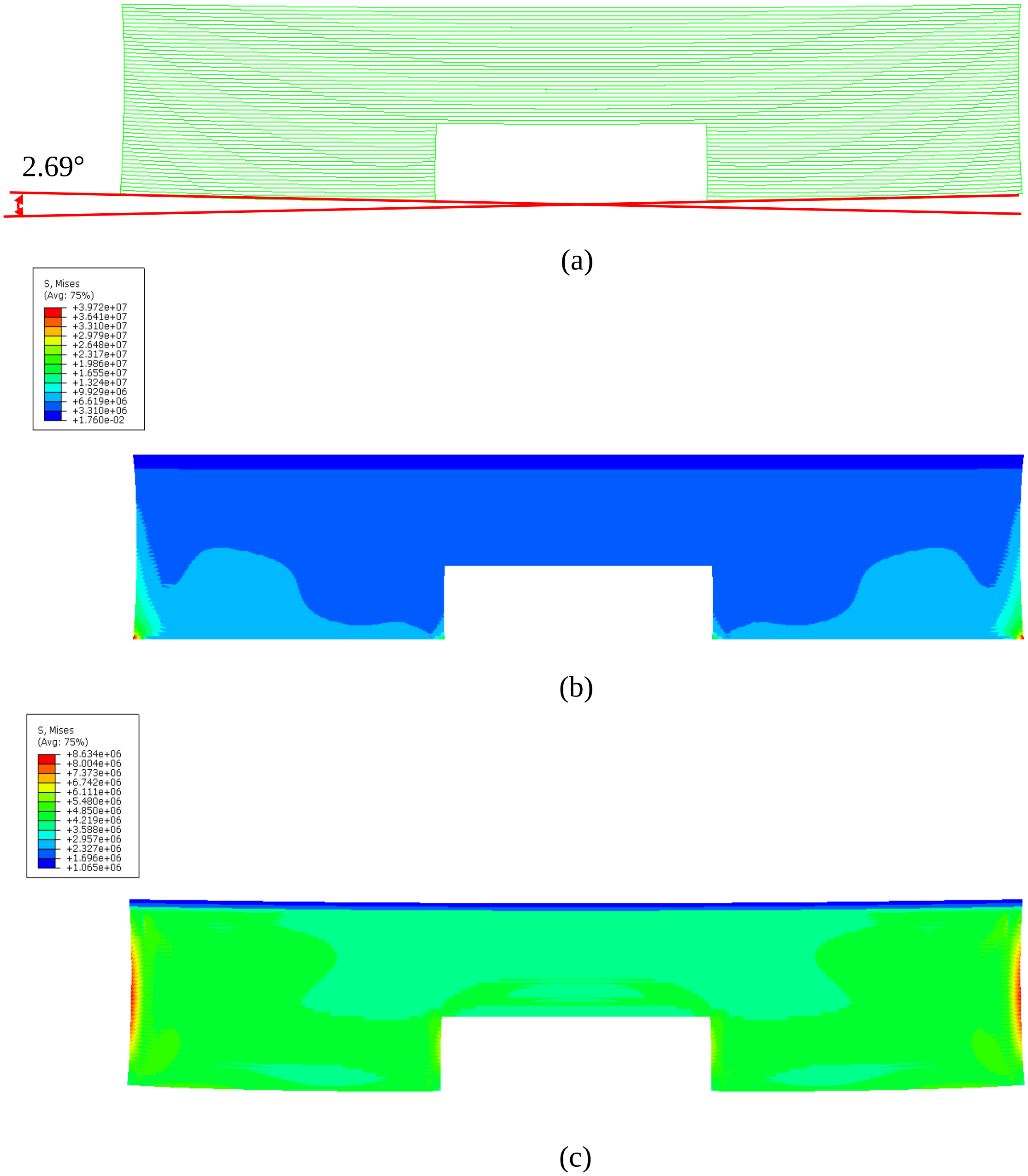

Figure 2.19 Simulation results for BCM test part with 3mm thick bridge overhang. (a) Deformed shape of BCM test part with the angle measured after releasing it from the base plate, (b) Mises stress before releasing, (c) Mises stress after releasing.

It can be seen from Figure 2.19 that the maximum value of Mises stress reduces from 39.7MPa to 8.63MPa after the BCM test part is released from the base plate. Due to this relaxation of internal stresses, the bridge curls, and thus a curling angle is formed between the two planes at the bottom of the pillars of the bridge. In Figure 2.17, both the experimental and simulation results show that the curling angle will go up as the thickness of the bridge overhang increases. This is because the internal stresses accumulated during the layered manufacturing process become larger and larger as the process proceeds and new layers are cured above. Hence, a greater level of internal stresses can be relaxed when removing the part from base plate, as illustrated in Figure 2.20. In this figure, the maximum value of Mises stress in the BCM test part with 6mm thick bridge overhang reduces from 48.3MPa to 10.8MPa after being released from the base plate. Therefore, it can be verified that the curling angle is indeed a measure of the residual stresses in the part after fabrication. Figure 2.17 also shows that the value of curling angle tends to stabilize around a certain value when the overhang thickness is high. In Figure 2.17, the simulation results match well with the experiments. Although there is a small gap between the values of β obtained in the simulations and in the experiments, it can be noted that they have a similar trend and the difference is no more than 0.4°. Therefore, the numerical model developed in this chapter is validated experimentally, and it can be used as an analysis method to investigate the residual stresses and curl distortions formed during the LAMP process, enabling the exploration of possible stress reduction strategies in a fast and easy way.

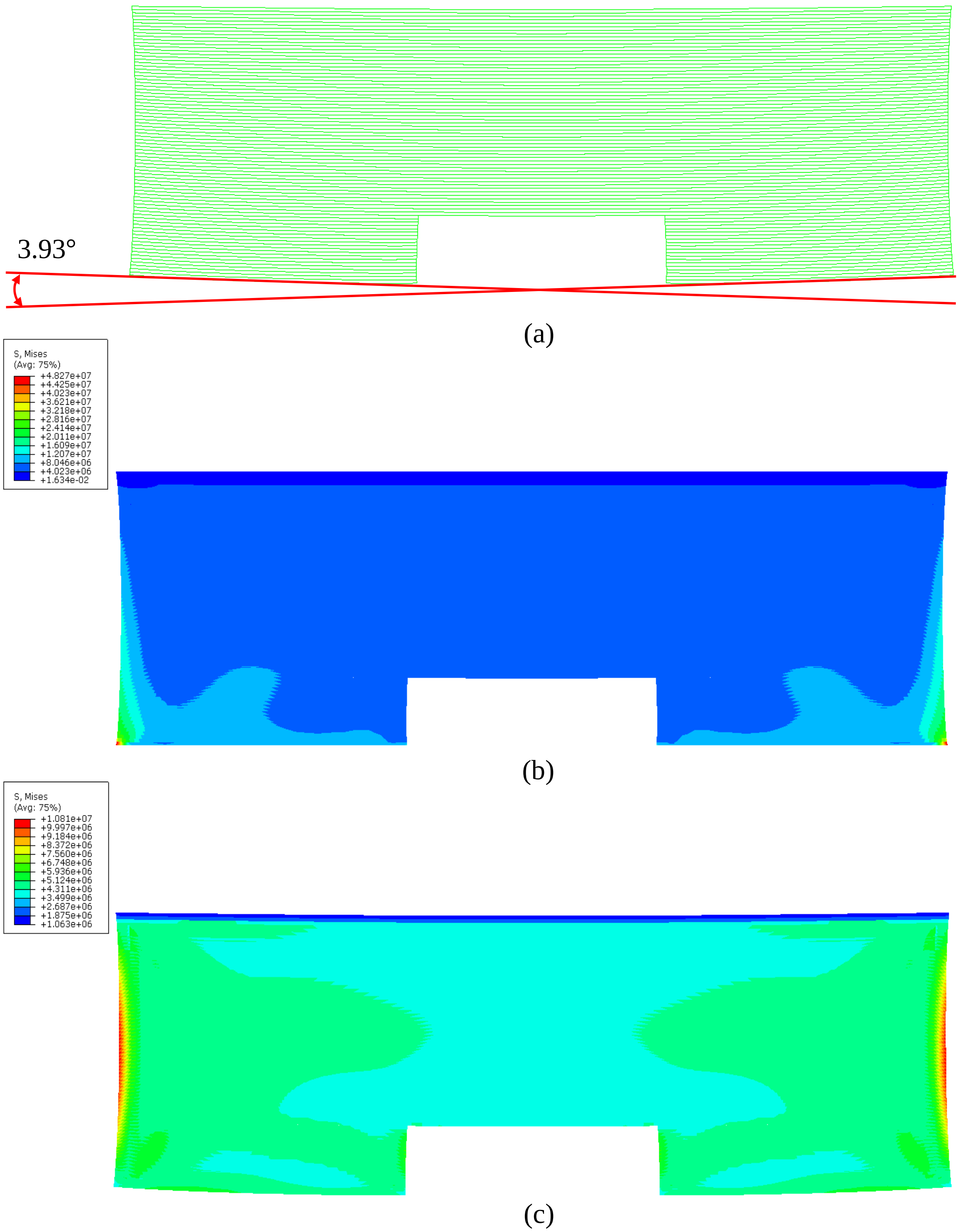

Figure 2.20 Simulation results for BCM test part with 6mm thick bridge overhang. (a) Deformed shape of BCM test part with the angle measured after releasing it from the base plate, (b) Mises stress before releasing, (c) Mises stress after releasing.

CHAPTER 3

INTERLAMINAR FRACTURE CHARACTERIZATION BASED ON LINEAR ELASTIC FRACTURE MECHANICS

3.1 Introduction

Cracking/delamination may occur under three different types of loading, as Figure 3.1 illustrates. Mode I loading, where the principal load is applied normal to the crack plane, tends to open the crack. Mode II loading corresponds to in-plane shear loading and tends to cause one crack face to slide with respect to the other. Mode III loading refers to out-of-plane shear. A cracked body can be loaded in any one of these modes, or there can be a combination of two or three modes [42].

The resistance of a material to crack extension is expressed in terms of fracture toughness, which is generally measured experimentally. A fracture toughness test may yield either a single value of fracture toughness or a resistance curve (R curve), where a toughness parameter such as K (stress intensity factor) or G (energy release rate) is plotted against the crack extension. A single toughness value is usually sufficient to describe a fracture test, especially when the fracture mechanism is unstable. The fracture toughness of a material can be measured for each of the three pure modes or for a mixed mode. A variety of organizations throughout the world have published standardized procedures for fracture toughness measurements under different loading conditions and for different types of materials, including metals, plastics and composites. In this dissertation, only the procedures for interlaminar fracture toughness measurements of composites are studied since cracks occur predominantly at the inter-layer interfaces in the LAMP-built parts.

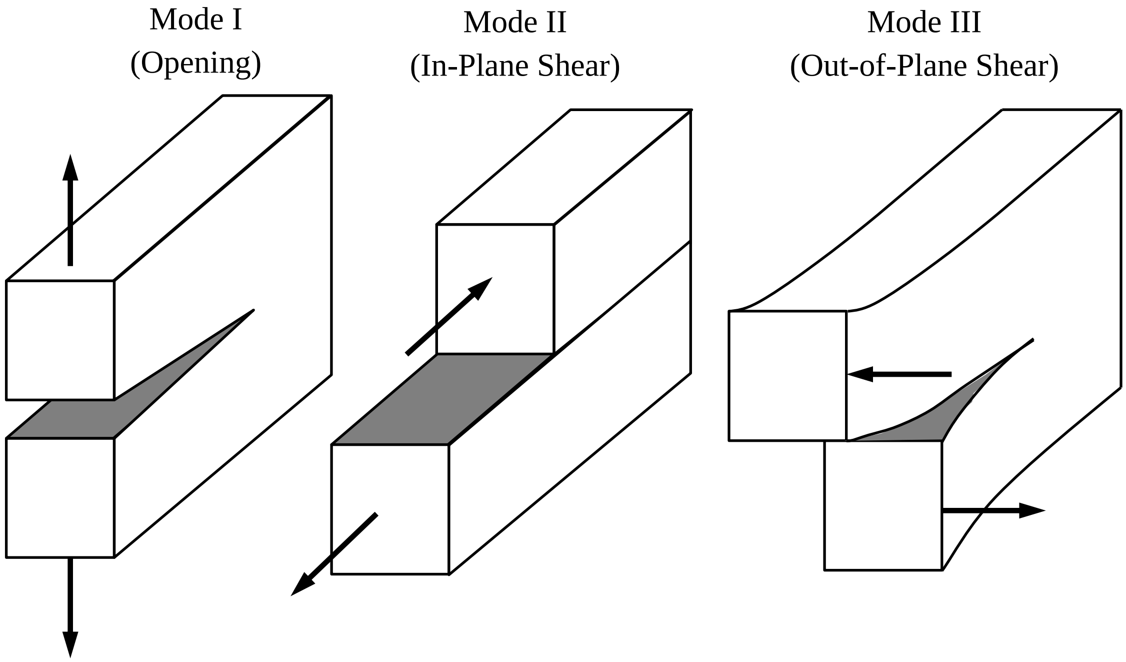

Figure 3.1 The three basic crack/delamination modes

In this chapter, the application of linear elastic fracture mechanics (LEFM) to characterize and predict delamination growth is reviewed first. Both the energy and stress-intensity approaches to linear fracture mechanics are described. Then the typical experimental testing methods for the determination of Mode I and Mode II interlaminar fracture toughness are discussed. Mode III fracture is not considered in this dissertation, since it is negligible in the delamination process for LAMP.

3.2 Fracture Parameters in LEFM

There are mainly two alternative approaches to fracture analysis: the energy and the stress-intensity approaches. These two approaches are essentially equivalent for linear elastic materials. The most fundamental concepts in these two approaches are the two fracture parameters: the energy release rate (G) and the stress intensity factor (K). These two fracture parameters are commonly used for fracture prediction and toughness characterization. The fracture toughness is defined as the critical value of G or K when the crack growth initiates and is an intrinsic material property that can be characterized through experimental testing.

3.2.1 The Energy Approach and Energy Release Rate

The energy approach to fracture mechanics states that fracture occurs when the energy available for crack growth is sufficient to overcome the resistance of the material. The material resistance may include the surface energy, plastic work, or other types of energy dissipation associated with a propagating crack [42]. Griffith [43] was the first to propose the energy approach for fracture, and Irwin [44] developed the present version of this approach. In this approach, the energy release rate G is defined as the change in total potential energy per unit area of crack extension for a linear elastic material, given as

$$\mathrm{G} = -\frac{d\Pi}{dA} \tag{3.1}$$

where A is the area of the new crack face and Π is the potential energy. The potential energy of an elastic body can be given by

$$\Pi = \mathrm{W} - \mathrm{U} \tag{3.2}$$

where W is the work done by external forces and U is the elastic strain energy stored in the body. Irwin found that if the size of the plastic zone around a crack is small compared to the size of the crack, the energy required to grow the crack will not be critically dependent on the state of stress at the crack tip. In other words, a purely elastic solution may be used to calculate the amount of energy available for fracture.

A structure is said to be load-controlled when the load applied on it is fixed at P. Consider a cracked plate that is load controlled. For this case

$$W = P\delta \tag{3.3}$$

and

$$U = \int_0^{\delta} P d\delta = \frac{P\delta}{2} \tag{3.4}$$

where δ is the corresponding displacement at the load point. Therefore

$$\Pi = -U = \frac{P\delta}{2} \tag{3.5}$$

and

$$G = \left(\frac{dU}{dA}\right)_P = \frac{1}{B}\left(\frac{dU}{da}\right)_P = \frac{P}{2B}\left(\frac{d\delta}{da}\right)_P \tag{3.6}$$

where B is the thickness of the cracked plate and a is the crack length. Similarly, when the displacement is fixed at δ, the structure is said to be displacement controlled. Then, for the cracked plate, $W = 0$ and $\Pi = U$. Therefore

$$G = -\left(\frac{dU}{dA}\right)_\delta = -\frac{1}{B}\left(\frac{dU}{da}\right)_\delta = -\frac{\delta}{2B}\left(\frac{dP}{da}\right)_\delta \tag{3.7}$$

The compliance C, which is the inverse of the plate stiffness, is defined as

$$C = \frac{\delta}{P} \tag{3.8}$$

By substituting Equation (3.8) into Equation (3.6) and Equation (3.7) it can be shown that for both load control and displacement control

$$G = \frac{P^2}{2B}\frac{dC}{da} \tag{3.9}$$

Therefore, the energy release rate for crack growth, as defined in Equation (3.1), is the same for load control and displacement control. Also

$$\left(\frac{dU}{da}\right)_P = -\left(\frac{dU}{da}\right)_\delta \tag{3.10}$$

The above equation can also be demonstrated graphically as shown in Figure 3.2. In load control, a crack extension da results in a net increase in strain energy, which is represented by the shaded area in Figure 3.2(a), due to the contribution of the external work

$$(dU)_P = Pd\delta - \frac{Pd\delta}{2} = \frac{Pd\delta}{2} \tag{3.11}$$

In contrast, in displacement control, shown in Figure 3.2(b), the value of external work is zero and a crack extension da causes the strain energy to decrease with the amount of

$$(dU)_\delta = \frac{\delta dP}{2} \tag{3.12}$$

where dP is negative. It can be seen in Figure 3.2 that the absolute values of these energies, which are represented by the two shaded area, only differ by the negligible amount of $dPd\delta/2$. Thus, $(dU)_P = (dU)_\delta$ and Equation (3.10) is proved.

Equation (3.9) is widely used for obtaining the values of energy release rate and fracture toughness. It is valid if the crack advances along the full width of the specimen and self-similar crack growth happens; i.e., a planar crack is assumed to remain planar and to maintain a constant shape as it grows. The compliance in terms of crack length is either calculated theoretically from analyzing the size, geometry and material properties of the cracked body, or it is obtained experimentally from the measured load-displacement curve for the testing specimen. Then, the derivative of compliance to crack length can be calculated or determined graphically.

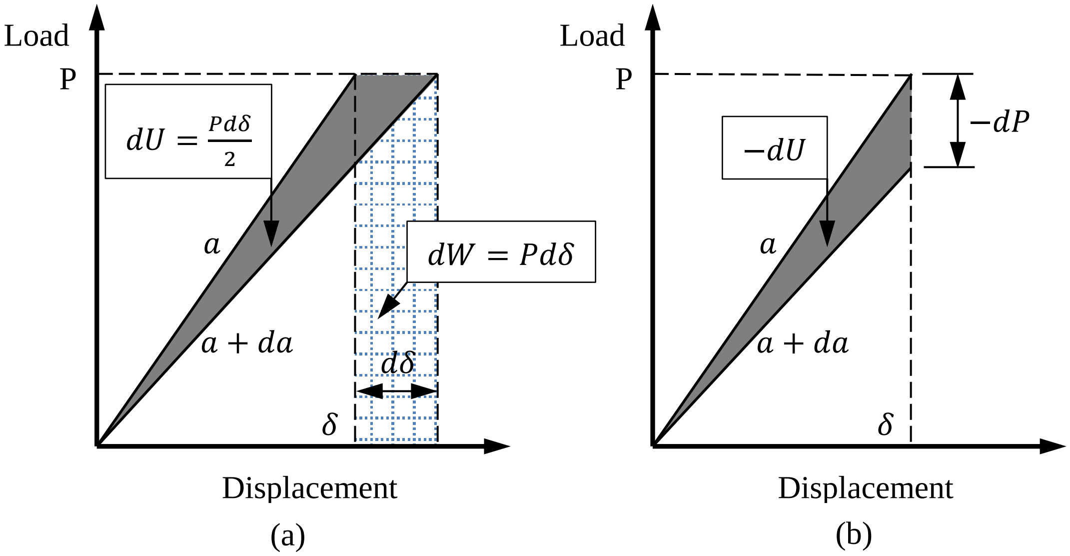

Figure 3.2 The increment of elastic strain energy for an increment of crack growth at a given (a) load P and (b) displacement δ

The critical energy release rate G_c is a measure of fracture toughness, which is the material's resistance to crack growth. The value of G_c can be obtained experimentally, by loading a cracked specimen. One of the fundamental assumptions of fracture mechanics is that fracture toughness is independent of the geometry and size of the cracked body; a fracture toughness measurement of a test specimen should be applicable to an entire structure. As long as this assumption is valid, all configuration effects are taken into account by the driving force G [42]. This assumption is valid as long as the material behavior is predominantly linear elastic. For crack initiation and propagation to occur, the fracture criterion is

$$G \geq G_c \tag{3.13}$$

3.2.2 The Stress-Intensity Approach and Stress Intensity factor

The stress-intensity approach is established based on a crack-tip parameter, K, which is called the stress intensity factor. Irwin [45] found that closed-form expressions for the stresses in the body can be derived for certain cracked configurations subjected to external forces, assuming isotropic linear elastic material behavior. If a polar coordinate system is defined with the origin at the crack tip, as illustrated in Figure 3.3, it can be shown that the stress field in any linear elastic cracked body is given by

$$\sigma_{ij} = \left(\frac{K}{\sqrt{2\pi r}}\right) f_{ij}(\theta) + \sum_{m=0}^{\infty} A_m r^{\frac{m}{2}} g_{ij}{}^{(m)}(\theta) \tag{3.14}$$

where σ_{ij} is the stress tensor and K is a constant defined as the stress intensity factor. $f_{ij}(\theta)$ is a dimensionless function of θ in the leading term. For the higher-order terms, A_m is the amplitude and $g_{ij}{}^{(m)}(\theta)$ is a dimensionless function of θ for the mth term. As $r \to 0$, the leading term approaches infinity while the other terms remain finite or approach zero. Therefore, the stress near the crack tip is proportional to $1/\sqrt{r}$

regardless of the configuration of the cracked body, and the above equation describes a stress singularity around the crack tip.

Note that, in Equation (3.14), the stress near the crack tip is also proportional to a constant K. This constant completely characterizes the crack-tip conditions in a linear elastic material; it is called the stress intensity factor. If K is known, the entire stress distribution at the crack tip can be computed. The stress-intensity approach states that fracture occurs when

$$K \geq K_c \tag{3.15}$$

where K is the stress intensity factor that can be calculated from the geometry and loading. K_c is referred to as the critical stress intensity factor, which is an intrinsic material property. It is an alternate measure of fracture toughness.

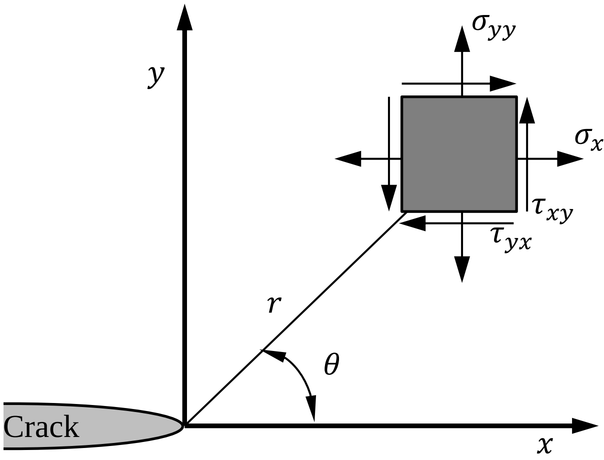

Figure 3.3 Definition of the coordinate axis and stresses near the tip of a crack.

For each mode of loading, the stress intensity factor is denoted as K_I, K_{II} and K_{III} respectively. Thus, the stress fields ahead of the crack tip in an isotropic linear elastic material can be written for each mode as

$$\lim_{r\to 0} \sigma_{ij}{}^{(I)} = \frac{K_I}{\sqrt{2\pi r}} f_{ij}{}^{(I)}(\theta) \tag{3.16}$$

$$\lim_{r\to 0} \sigma_{ij}{}^{(II)} = \frac{K_{II}}{\sqrt{2\pi r}} f_{ij}{}^{(II)}(\theta) \tag{3.17}$$

$$\lim_{r\to 0} \sigma_{ij}{}^{(II)} = \frac{K_{III}}{\sqrt{2\pi r}} f_{ij}{}^{(III)}(\theta) \tag{3.18}$$

The detailed expressions (i.e. the detailed expressions of $f_{ij}(\theta)$) for the singular stress fields for each mode are not shown here, but they can be found in literature [42]. In a mixed-mode condition, the individual contributions to a given stress component are additive according to the principle of linear superposition

$$\sigma_{ij}{}^{(total)} = \sigma_{ij}{}^{(I)} + \sigma_{ij}{}^{(II)} + \sigma_{ij}{}^{(III)} \tag{3.19}$$

For linear elastic materials, individual components of stress, strain and displacement are additive. Similarly, stress intensity factors are additive as long as the mode of loading is consistent. For example

$$K_I{}^{(total)} = K_I{}^{(P1)} + K_I{}^{(P2)} + K_I{}^{(P3)} \tag{3.20}$$

where $K_I{}^{(P1)}$, $K_I{}^{(P2)}$ and $K_I{}^{(P3)}$ are the Mode I stress intensity factors imposed by different external forces $P1$, $P2$ and $P3$, respectively. But, it should be noticed that

$$K_{(total)} \neq K_I + K_{II} + K_{III} \tag{3.21}$$

In contrast, contributions to the energy release rate G from the three modes are additive, because the energy release rate, like energy, is a scalar quantity. Thus when all three modes of loading are present, the total energy release rate is given by

$$G_{(total)} = G_I + G_{II} + G_{III} \tag{3.22}$$

Both of the parameters, G and K, can describe the fracture behavior, although they do so from two different perspectives. The former parameter gives the change in potential energy with an increment of crack extension, and the latter one characterizes the stresses, strains and displacements near the crack tip. The energy release rate describes global behavior, while the stress intensity factor is a local parameter. For linear elastic materials, Irwin [46] proves that these two fracture parameters are related through

$$G_I = \frac{K_I^2}{E'} \tag{3.23}$$

where $E' = \mathrm{E}$ for plane stress conditions and $E' = \frac{E}{1-\nu^2}$ for plane strain conditions. E is the Young's modulus and ν is the Poisson's ratio of the material. Similar relationships between G and K can also be obtained for Mode II and Mode III. Substituting these relationships into Equation (3.22), the total energy release rate in a mixed mode condition is given by

$$G_{(total)} = \frac{K_I^2}{E'} + \frac{K_{II}^2}{E'} + \frac{K_{III}^2}{2\mu} \tag{3.24}$$

where μ is the shear modulus of the material.

3.2.3 Fracture Parameters for Characterizing the Delamination of Composite Laminates

The relationship between G and K demonstrates that these two fracture parameters are essentially equivalent and interchangeable for linear elastic materials. The fracture toughness, i.e. the critical value of G or K, is measured experimentally. The elastic stress analysis of sharp cracks predicts infinite stresses at the crack tip. In real materials, however, stresses at the crack tip are finite, since the crack-tip radius is finite and the inelastic material deformation, e.g. plasticity in metals and crazing in polymers, further relaxes the crack-tip stresses. The elastic stress analysis becomes increasingly inaccurate as the inelastic region at the crack tip grows. Thus, the small scale yielding condition has to be satisfied in order to obtain an accurate measurement of the fracture toughness in terms of the stress intensity factor K. The size of the crack-tip-yielding zone, which can be estimated by the Irwin approach or the strip-yield model [47, 48], must be smaller than the size of K-dominance zone, which is scaled by the characteristic dimension of the problem. For composite laminates, the characteristic dimension is usually on the order of several plies in thickness. The crack-tip-yielding zone, however, may be quite large compared to the thickness [49]. With a relative extensive yielding, in this case, one must apply alternative crack-tip parameters that take nonlinear material behavior into account. The energy release rate, G, is defined based on the energy balance approach and is typically used to measure the fracture toughness for delamination of the composite laminate. This is because the corresponding experimental approaches need few measurements of the material properties, and the increment of new-crack-face area in the definition of G is natural for describing the delamination growth. In the next section, the experimental approaches for measuring the Mode I and Mode II critical energy release rate, G_{Ic} and G_{IIc}, for delamination growth will be reviewed.

3.3 Double Cantilever Beam (DCB) Test for Characterizing Mode I Delamination

3.3.1 Introduction

To characterize the interlaminar fracture of composites, a zone of delamination can be treated as a crack, and the resistance of the material to the propagation of this crack is the fracture toughness. Since the crack is typically confined to the matrix material between plies, the continuum theory is applicable, and the crack growth is self similar [50], i.e., a planar crack is assumed to remain planar and to maintain a constant shape as it grows. Over the past several decades, many experiments [51] have been performed on fiber-reinforced composites to characterize the delamination process. Some of the test methods have been standardized by a variety of organizations throughout the world for interlaminar fracture toughness measurement. The opening Mode I interlaminar fracture toughness, G_{Ic}, is usually measured through the double cantilever beam (DCB) test, which has been universally accepted and standardized for laminated composite materilas by ASTM D 5528 [52]. A schematic of the DCB test specimen is shown in Figure 3.4.

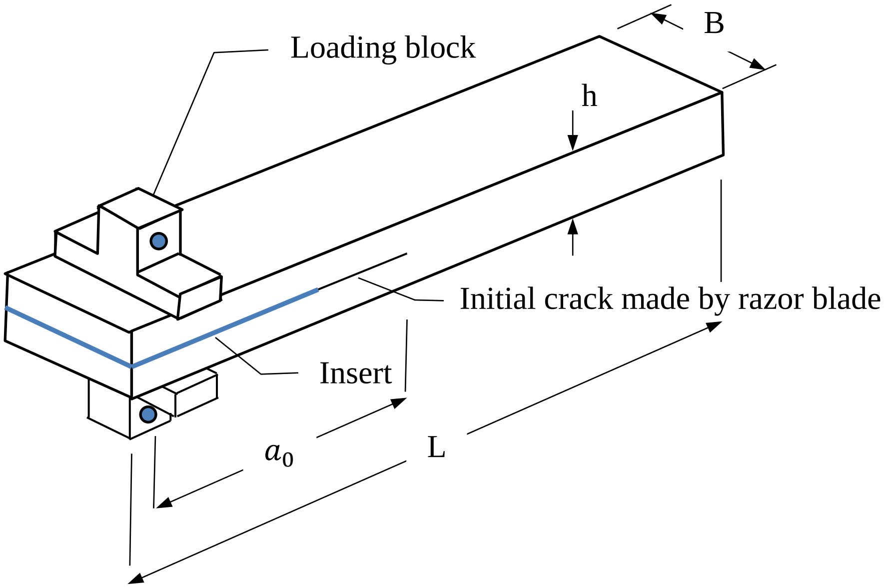

Figure 3.4 Schematic of the double cantilever beam (DCB) specimen with loading blocks

As illustrated in Figure 3.4, the length, width and thickness of the specimen are given by L, B and h, respectively. The crack length is given by a, and a_0 refers to the initial crack length before the test. The DCB specimen usually consists of a rectangular laminated composite with uniform thickness. A thin, non-adhesive insert film is inserted at the midplane of the laminate during the layup process of the specimen to form an initiation site for the delamination. Due to the significant strength of the composite material through the laminate thickness, DCB specimens may experience failures of the beam arms rather than the intended interlaminar failures. In order to further promote crack initiation and prevent failures of the beam arms, a fine razor blade can be used to introduce a precrack ahead of the insert front. After the precrack is cut in the specimen, loading blocks are bonded by adhesives on the upper and lower cantilever beams opposite each other. The initial delamination length a_0 is measured from the load line (center of the pin hole on the loading block) to the end of the precrack. As shown in Figure 3.5, opening forces are applied to the DCB specimen by pins through the holes of loading blocks. Then the ends of the DCB specimen are opened by controlling the crosshead movement, while the load force is recorded. The loading-line displacement δ is measured by the crosshead travel because the compliance of the loading machine is small enough to be ignored.

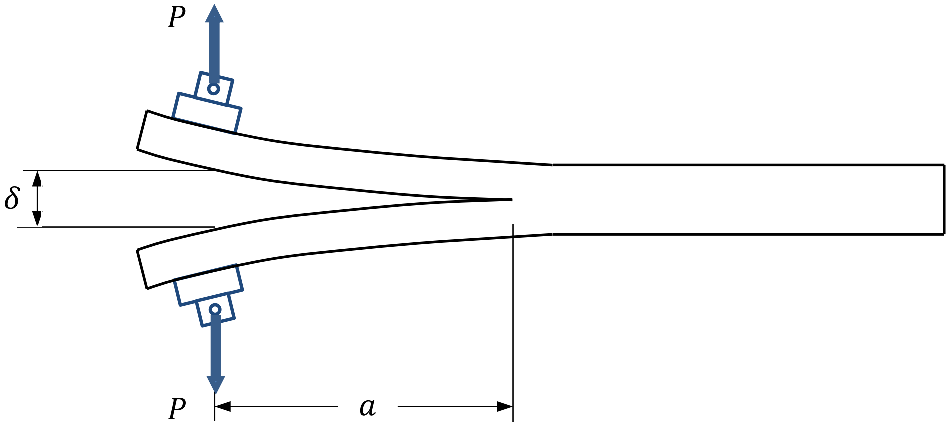

Figure 3.5 Schematic of the double cantilever beam (DCB) test

For the DCB test, stable delamination growth usually occurs under displacement-controlled loading, which makes it possible to continuously measure the fracture toughness as the crack advances. After the load-displacement curve is obtained, the compliance of the specimen can be calculated, and several data reduction schemes can be used to compute the delamination toughness G_{Ic}. These data reduction schemes will be discussed in the next subsection.

3.3.2 Data Reduction Schemes Used for the DCB Test

In this section, three kinds of commonly used data reduction methods for DCB tests to determine the G_{Ic} values are studied. None of the three is clearly superior to the others, since the G_{Ic} values calculated by the three different methods have little difference.

The first kind of data reduction approach derives the compliance in Equation (3.9), which is generally used to compute G, using classical beam theory (BT) or modified beam theory (MBT). For pure Mode I loading, from elastic beam theory

$$\delta = \frac{2Pa^3}{3EI} \tag{3.25}$$

where the inertial moment of the cross-sectional area for the beam is $I = \frac{Bh^3}{12}$.

The elastic compliance is given by

$$C = \frac{\delta}{P} = \frac{2a^3}{3EI} \tag{3.26}$$

Substituting the compliance into Equation (3.9) gives

$$G_{Ic} = \frac{P^2a^2}{BEI} = \frac{12P^2a^2}{B^2h^3E} \tag{3.27}$$

or

$$G_{Ic} = \frac{3P\delta}{2Ba} \tag{3.28}$$

The above two equations are equivalent; they differ only in that the displacement, δ, is involved in Equation (3.28), which is called a Load & Displacement expression. In contrast, Equation (3.27), which is called a Load-only expression, does not involve δ. In practice, these two equations will overestimate G_{Ic}, since the classical beam theory calculates the compliance of a cantilever beam that is perfectly built-in (that is, rigidly fixed at the crack tip) [52]. However, rotation may occur at the delamination front, and one way of correcting for this rotation is to treat the DCB as if it contained a slightly longer delamination, $a + \chi h$, where χh may be determined experimentally by generating a least square plot of the cube root of compliance $C^{1/3}$, as a function of delamination length. When the thickness of the specimen is small or the material has a low flexural modulus or high interlaminar fracture toughness, large deflections of the specimen arms may occur during the DCB test. In this case, the large deflection corrections must be incorporated in the data reduction. An expression accounting for the rotation effects at the crack tip, transverse-shear effects, loading-block effects and large-deflection effects [53, 54] is given by

$$G_{Ic} = F\frac{12P^2(a+\chi h)^2}{B^2h^3E} \tag{3.29}$$

or

$$G_{Ic} = \frac{F}{N}\frac{3P\delta}{2B(a+\chi h)} \tag{3.30}$$

where F and N are correction factors for large deflection and for the local stiffening caused by loading blocks. χh is the added crack length to correct for the rotation at the crack tip and traverse shear. The factor χ can be determined based on the relationship between compliance and crack length. The former equation is a Load-only expression, and the latter one is a Load & Displacement expression. The compliance can be derived from analysis of the DCB test and expressed as a function of crack length [55], given by

$$C = N\frac{8(a+\chi h)^3}{EBh^3} \tag{3.31}$$

A linear relationship between $(\frac{C}{N})^{1/3}$ and a can be derived as

$$(\frac{C}{N})^{1/3} = k_1a + k_2 \tag{3.32}$$

where

$$k_1 = (\frac{8}{EBh^3})^{1/3} \tag{3.33}$$

$$k_2 = k_1\chi h \tag{3.34}$$

Therefore, by generating a least-squares fit of $(\frac{C}{N})^{1/3}$ versus a, the slope k_1 and the intercept k_2 can be obtained. Then the values of modulus E and correction factor χ can be calculated by Equation (3.33) and Equation (3.34). In this approach, the compliance can be determined either from the slope of the load-displacement curve during the unload-reload cycle at different crack lengths or from the ratio of the load point displacement to the applied load, δ/P, in the definition.

The second kind of data reduction method calculates the compliance in Equation (3.9) from experimental data and is referred to as the compliance calibration (CC) method or modified compliance calibration (MCC) method. Similar to the correction procedure in the MBT approach, the compliance can be either determined from the slope of $P-\delta$ curve by unloading and reloading the specimen at various crack lengths or from the ratio δ/P in a continuous loading process. A least-squares fit is performed on the data points of C versus a using an empirical power law of the form [56]

$$C = Ra^n \tag{3.35}$$

where R and n are constants. Substituting the above expression of compliance into Equation (3.9) gives

$$G_{Ic} = \frac{nP^2Ra^{n-1}}{2B} \tag{3.36}$$

or

$$G_{Ic} = \frac{nP\delta}{2Ba} \tag{3.37}$$

Therefore, the energy release rate can be determined by using the exponent n obtained from the least-squares fit of the $C - a$ curve. As before, the former equation is a Load-only expression and the latter one is a Load & Displacement expression.

In a modified compliance calibration method, a least-squares plot of the delamination length normalized by specimen thickness, a/h, as a function of the cube root of compliance, $C^{1/3}$, is generated. The slope of this linear fitted line, A_1, is used to calculate the energy release rate as follows [52]

$$G_{Ic} = \frac{3P^2C^{2/3}}{2A_1Bh} \tag{3.38}$$

The third kind of data reduction approach is called the area method [42, 55]. Figure 3.6 schematically illustrates a typical $P - \delta$ curve, where the specimen is periodically unloaded and reloaded. The loading portion of the curve is typically nonlinear, while the unloading curve is usually linear. The change in strain energy with crack extension of Δa is estimated by the increment area inside the $P - \delta$ curve (the shaded area in the schematic). Thus, the energy release rate can be determined from the ratio of the change in strain energy to the change in crack area

$$G_{Ic} = \frac{\Delta U}{B\Delta a} \tag{3.39}$$

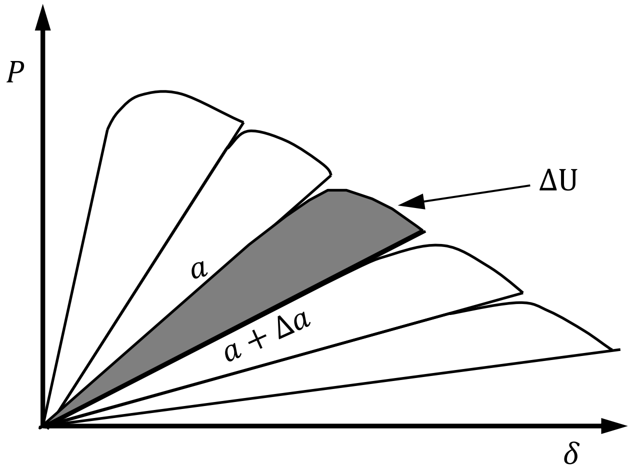

Figure 3.6 Schematic of the load-displacement ($P - \delta$) curve for delamination toughness measurement

It can be seen that the fracture toughness estimated by the area method is actually an average value over some values of crack growth increment, and is therefore not very precise [55]. The area method assumes that all of the strain energy released from the body during crack growth goes into the delamination process. This assumption would be violated if other processes consuming energy, e.g. viscoelastic deformation, occur.

3.3.3 Experimental Results

To estimate the Mode I interlaminar fracture toughness G_{Ic}, DCB tests were carried out using a universal material testing machine, as shown in Figure 3.7. The test machine was operated in a displacement control mode with a constant crosshead rate of $5\mu m/s$. Opening forces were applied to the DCB specimen by means of loading blocks bonded to one end of the specimen. Then ends of the DCB specimen were opened by controlling the crosshead movement, while the load force was recorded. Five groups of DCB specimens were built using five different exposure times, corresponding to the cure depths of 120μm, 150μm, 200μm, 250μm and 300μm respectively. The length, width and thickness of each specimen were 70mm, 10mm and 5.6mm, respectively. A polymer film was inserted at the midplane of the laminate during layup to form a delamination starter. Due to the significant strength of the composite material through the laminate thickness, DCB specimens might experience failures of the beam arms rather than the intended interlaminar failures. In order to further promote crack initiation and prevent failures of the beam arms, a precrack was introduced ahead of the insert front by tapping or sawing a fine razor blade. The material composition has been shown in Table 2.1 and the five exposure times used are given in Table 2.2. Each specimen group corresponds to a value of conversion degree, which has been determined by FTIR analysis and is given in Table 2.3. Therefore, after post-processing the data got from DCB tests for each group of specimens, the change of G_{Ic} with respect to the degree of conversion can be obtained.

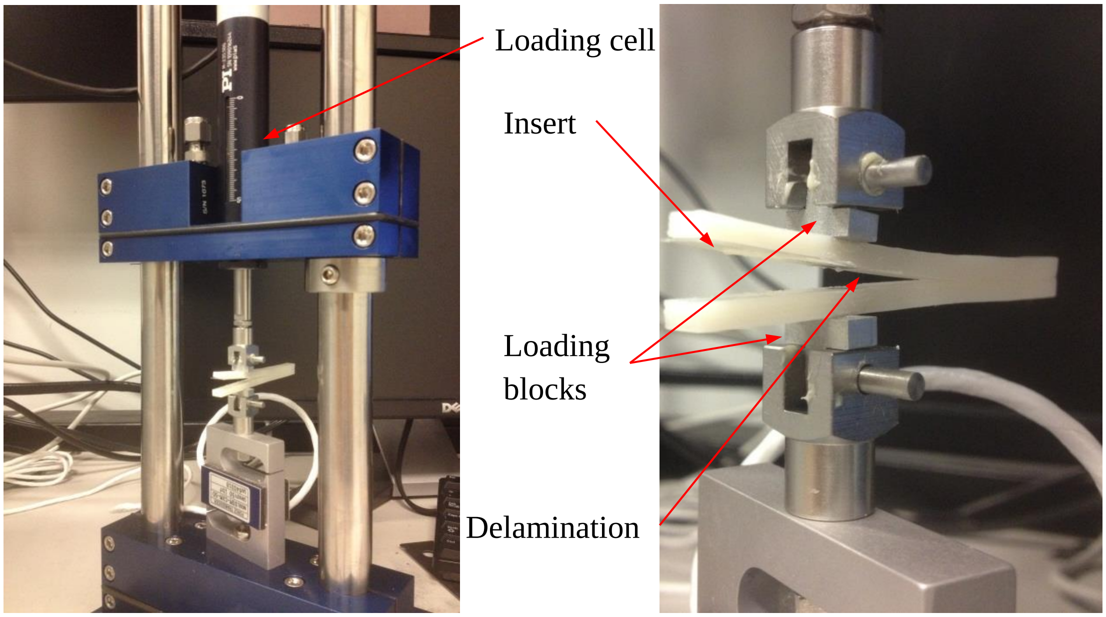

(a) (b)

Figure 3.7 (a) DCB experimental setup and (b) a DCB specimen in loading

Since crack length monitoring is difficult as the testing is in progress, a compliance calibration method is employed to calculate the crack length (a) in this study. To do so, DCB specimens need to be unloaded and reloaded several times during the tests [57]. Figure 3.8 shows a typical load-deflection $(\mathrm{P}-\delta)$ curve obtained from one DCB specimen with the unloading-reloading cycles. As seen, the load force increases with applied displacement and gradually drops when the curve passes a peak load, which indicates the onset of crack propagation. Specimen is then unloaded and the compliance (C) is estimated by the slope of the unloading line (note that the slope represents the stiffness, which is the reciprocal of the compliance). The crack length can be determined using a rearranged form of Equation (3.26) in beam theory

$$a = \sqrt[3]{\frac{3EIC}{2}} \tag{3.40}$$

The Mode I fracture toughness G_{Ic} can be evaluated with Equation (3.27) derived from beam theory

$$G_{Ic} = \frac{P^2a^2}{BEI} = \frac{12P^2a^2}{B^2h^3E} \tag{3.41}$$

where P is the critical load (peak load) of each unloading-reloading cycle at which the $\mathrm{P} - \delta$ curve begins to drop and the crack propagates, a is the crack length computed from the compliance, E is the Young’s modulus of the material, B and H are the width and thickness of the specimen respectively.

The specimen is reloaded, and the unloading-reloading cycle is repeated until the curve becomes flat. It can be seen from Figure 3.8 that the slope of unloading line decreases after each cycle, indicating an increase in the compliance due to the longer crack. For each cycle, a crack length is determined and a value of the fracture toughness G_{Ic} can be obtained. For the DCB specimen with its $\mathrm{P} - \delta$ curve shown in Figure 3.8, the calculation results are summarized in Table 3.1.

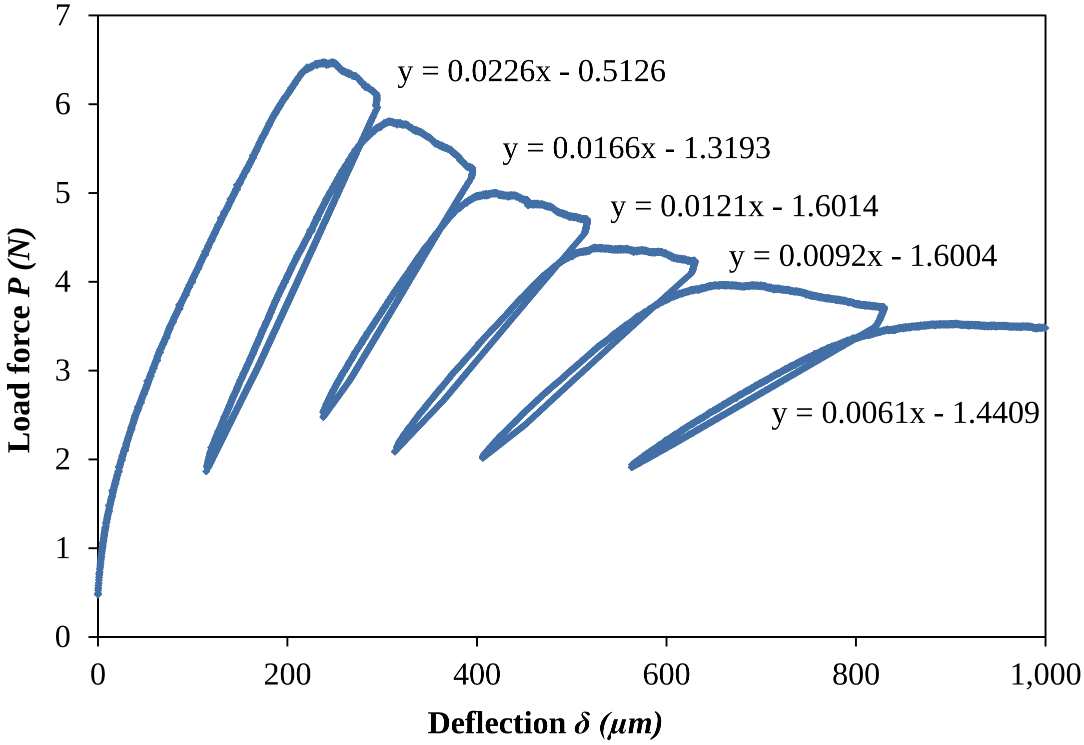

Figure 3.8 A typical $P - \delta$ curve obtained from DCB test

Table 3.1 DCB results summary for one specimen

Stiffness $(N/\mu m)$	Compliance C $(\mu m/N)$	Crack length a (μm)	P (N)	G_{Ic} (N/m)
0.0226	44.25	15184.01	5.81	14.08
0.0166	60.24	16828.80	4.99	12.78
0.0121	82.64	18699.39	4.38	12.12
0.0092	108.70	20487.71	3.96	11.91
0.0061	163.93	23495.21	3.52	12.41
			Average	12.66

The values of G_{Ic} are averaged for each group of specimens. Since each group corresponds to a certain cure depth and conversion degree, the change of G_{Ic} with respect to the degree of conversion can be obtained, as shown in Figure 3.9. As seen, G_{Ic} rises with increasing degree of conversion, as expected, and it rises more rapidly at a relatively high conversion degree. In the graph, an exponential curve is given by fitting the data points. In the numerical simulation for crack prediction, this exponential curve will be used as an input to the cohesive element model.

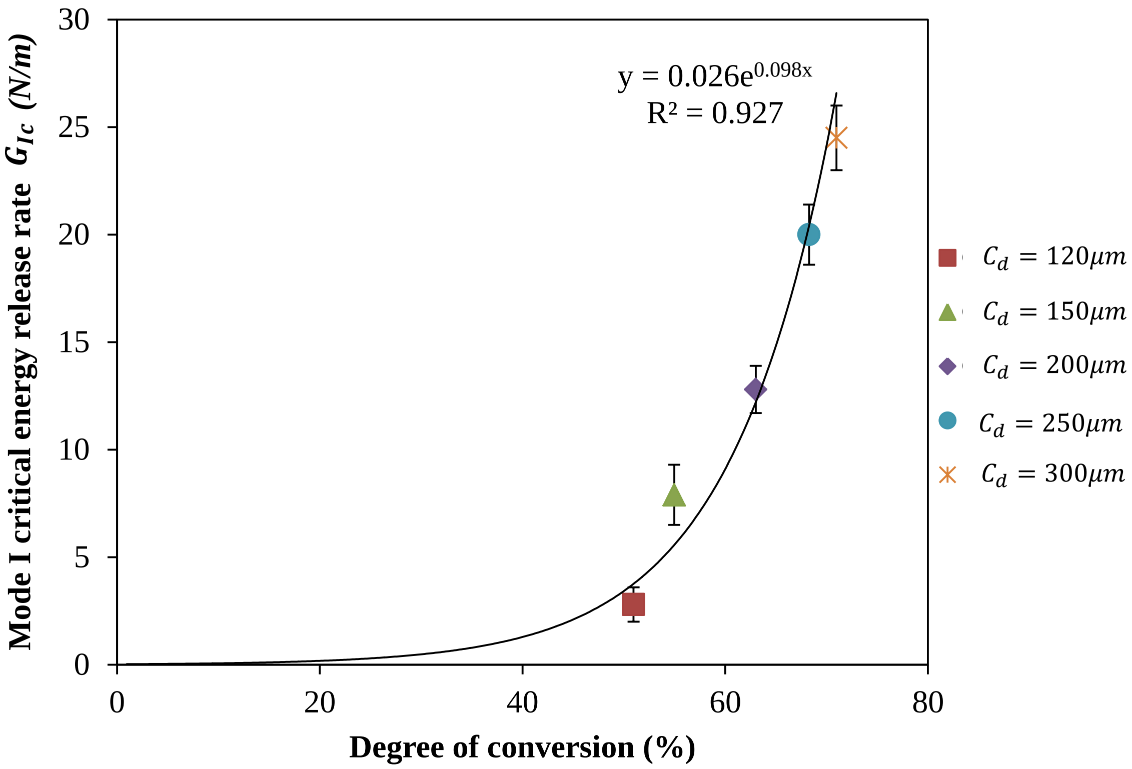

Figure 3.9 Mode I critical energy release rate vs. final conversion degree of the specimen

3.4 End Notched Flexure (ENF) Test for Characterizing Mode II Delamination

3.4.1 Introduction

In addition to Mode I fracture, delamination propagation is also frequently dominated or affected by Mode II fracture. Consequently, interlaminar fracture characterization under Mode II loading is fundamental to accurately predict the susceptibility of the material to delamination. While the Mode I has been extensively studied and the DCB test is universally accepted, the Mode II is not so well studied due to some difficulties inherent to the experimental tests, such as unstable crack propagation and difficulties in crack monitoring during propagation. Over the past several decades, various fracture characterization tests have been developed, among which the end loaded split (ELS) and end notched flexure (ENF) tests are the most popular ones to characterize Mode II fracture in composites. This section gives a brief description for each of them.

A schematic of the ENF test is shown in Figure 3.10. This test was first developed for wood fracture characterization [58]. The ENF specimen has essentially the same geometry as the DCB specimen, but it is loaded in three-point bend loading, which imposes Mode II displacements of the crack faces. Same as the DCB specimen, the ENF specimen contains a non-adhesive insert film on the midplane that serves as a delamination initiator, and a precrack is introduced ahead of the insert front by tapping or sawing a fine razor blade. One disadvantage of the ENF test is the unstable crack propagation during the loading process. A similar test method, named four point end notched flexure (4ENF) test, can be used to evaluate the Mode II energy release rate. As illustrated in Figure 3.11, its only difference from ENF test is that the pre-cracked 4ENF specimen is under four-point bend loading. This test does not require crack monitoring, but involves a more sophisticated setup and larger friction effects were observed [59].

Another alternative test method is based on the cantilever beam configuration, and is referred to as the end loaded split (ELS) test, which is illustrated in Figure 3.12. Although the ELS test involves more complexities relatively to the other tests, it provides a larger range of crack length at which the crack can propagate stably. According to the literature, in order to obtain stable crack propagation, the ELS test requires a_0/L>0.55 [60] whereas a_0/L>0.7 [61] is necessary in the ENF test. However, both of these tests suffer from the common difficulty for crack length measurement during the testing process. In fact, during any Mode II fracture test, the crack tends to close due to the applied load, which hinders a clear visualization of its tip and thereby makes crack length monitoring difficult. This problem, combined with the unstable crack propagation, precludes a rigorous measurement of the Mode II critical energy release rate G_{IIc}.

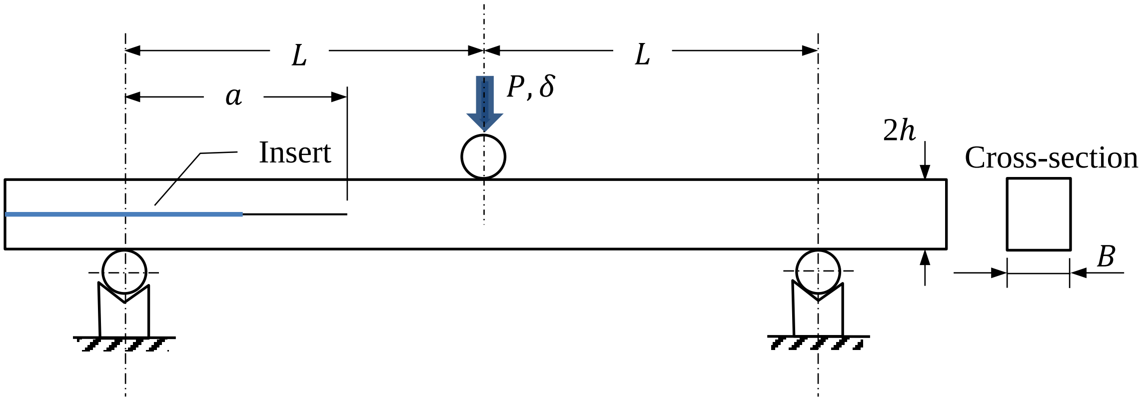

Figure 3.10 Schematic of the end notched flexure (ENF) test

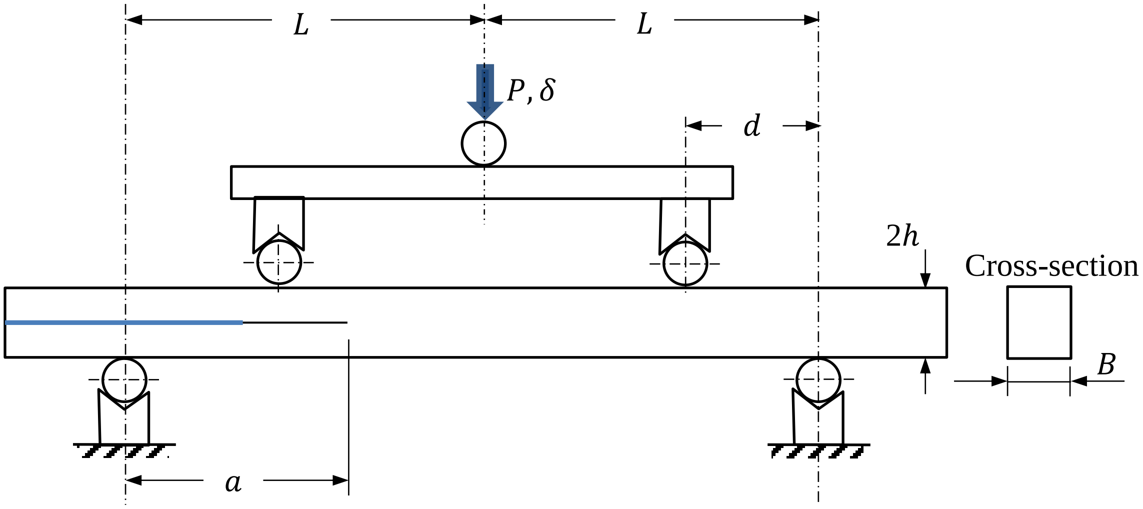

Figure 3.11 Schematic of the four point end notched flexure (4ENF) test

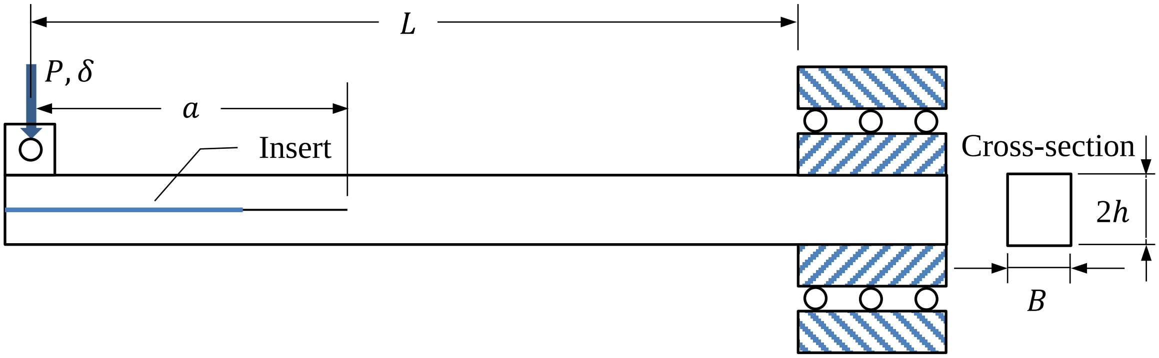

Figure 3.12 Schematic of the end loaded split (ELS) test

In this dissertation, the ENF test is employed as the experimental method for the determination of G_{IIc} owing to its simplicity. During the test, the loading machine is operated with controlled displacement. The applied load force P is recorded and the loading-line displacement δ is measured by the crosshead travel because the compliance of the loading machine is negligible. The obtained $P-\delta$ curve can be used to evaluate G_{IIc} through several data reduction schemes, which will be introduced in the following.

3.4.2 Data Reduction Schemes Used for the ENF Test

Three different data reduction schemes for the ENF test are presented in this section. Although all of them can be used to determine the Mode II fracture toughness G_{IIc}, the compliance based beam (CBB) method, which does not require crack length monitoring, overcomes the difficulties associated to classical data reduction methods, and will be employed in this dissertation.

The first data reduction scheme computes the compliance in Equation (3.9) from experimental data and is referred to as the compliance calibration (CC) method. The values of load, applied displacement and crack length $(P-\delta-a)$ are registered in order to use this method. The compliance (C) is determined from the ratio δ/P in continuous loading process and a cubic relationship is assumed between C and the measured crack length a [62]

$$C = D + ma^3 \tag{3.42}$$

where D and m are constants that can be obtained by performing a least-squares fit on the data points of C versus a. Substituting the above expression of compliance into Equation (3.9) gives

$$G_{IIc} = \frac{3mP^2a^2}{2B} \tag{3.43}$$

It can be seen that this method requires the calibration of the compliance (C) in function of the crack length (a). This can be done by measuring the crack length during propagation or, alternatively, considering several specimens with different initial crack lengths to establish the $C - a$ relation, which is then regressed by the cubic function. The Mode II critical strain energy release rate G_{IIc} is determined using the fitting coefficient m through Equation (3.43). One of the advantages for using this method is that elastic properties (e.g. Young's modulus E) are not required to compute G_{IIc}. However, the requirement for crack length monitoring makes this approach difficult to be implemented.

The second data reduction scheme derives the compliance in Equation (3.9) using classical beam theory (BT) or corrected beam theory (CBT). The compliance given by elastic beam theory for pure Mode II loading [63] is

$$C = \frac{L^3 + 12a^3}{32EBh^3} \tag{3.44}$$

where E is the axial modulus of the material. Substituting the compliance into Equation (3.9) gives

$$G_{IIc} = \frac{9P^2a^2}{16B^2h^3E} \tag{3.45}$$

Similar to the modified beam theory used for the DCB test, a correction of χh can be added to the crack length here. However, for the ENF test, the correction is now only from shear deformation and does not include root rotation, and thereby it is expected to be less than for the DCB test. If the elastic properties of the material are not known, χh can then be determined experimentally by generating a least square plot of the cube root of compliance $(C - C_0)^{1/3}$, as a function of delamination length a. Here C_0 is the compliance when $a = 0$. On the other hand, if the elastic parameters are known, Wang and Williams [64] provide one expression for CBT

$$G_{IIc} = \frac{9P^2(a + \chi h)^2}{16B^2h^3E} \tag{3.46}$$

where

$$\chi = 0.42\sqrt{\frac{E}{11G_{13}}\left[3 - 2\left(\frac{\Gamma}{1+\Gamma}\right)^2\right]} \tag{3.47}$$

$$\Gamma = 1.18\frac{\sqrt{EE_2}}{G_{13}} \tag{3.48}$$

where E_2 and G_{13} are the transverse and shear moduli, respectively. It can be seen that the application of beam theory to the ENF test involves the crack length measurement, which is difficult during the test.

The above two methods require crack length monitoring, which is hard to achieve. In this context, a new data reduction scheme, not depending on the crack length measurements, is proposed by de Moura [65]. This scheme is based on crack equivalent concept and depends only on the specimen compliance. Derived from the strain energy of the specimen and the Castigliano theorem, the displacement at the loading point for a crack length a [66] is

$$\delta = \frac{dU}{dP} = \frac{P(3a^3 + 2L^3)}{8E_f Bh^3} + \frac{3PL}{10G_{13}Bh} \tag{3.49}$$

where E_f is the flexural modulus of the specimen. It can be calculated from the above equation, using the initial compliance C_0 and the initial crack length a_0

$$E_f = \frac{3{a_0}^3 + 2L^3}{8Bh^3}\left(C_0 - \frac{3L}{10G_{13}Bh}\right)^{-1} \tag{3.50}$$

The above equation accounts for several effects not included in beam theory, such as contact between the two arms of the specimen and stress concentration near the crack tip.

It is known that, during propagation, a quite extensive fracture process zone (FPZ) ahead of crack tip exists under mode II loading. In the FPZ, materials may undergo properties degradation by various ways, such as fiber bridging, micro-cracking and inelastic processes. These phenomena dissipate non-negligible amounts of energy, and affect the compliance of the specimen. Thus the FPZ affects the measured toughness and should be taken into account in the Mode II tests. In order to include the FPZ effects, a correction of the real crack length is considered in Equation (3.49) to give the compliance

$$C = \frac{\delta}{P} = \frac{3(a + \Delta a_{FPZ})^3 + 2L^3}{8E_f B h^3} + \frac{3L}{10G_{13}Bh} \tag{3.51}$$

and consequently, the equivalent crack length

$$a_{eq} = a + \Delta a_{FPZ} = \left[\frac{C_{corr}}{C_{0corr}} a_0^3 + \frac{2}{3}\left(\frac{C_{corr}}{C_{0corr}} - 1\right) L^3\right]^{1/3} \tag{3.52}$$

where C_{corr} is given by

$$C_{corr} = C - \frac{3L}{10G_{13}Bh} \tag{3.53}$$

The Mode II fracture toughness, G_{IIc}, can be determined by

$$G_{IIc} = \frac{9P^2 a_{eq}^2}{16B^2 E_f h^3} \tag{3.54}$$

In summary, there are three steps in the application of this data reduction scheme. The first step is to estimate the initial compliance (C_0) from the initial slope of the $P - \delta$ curve. Then, the flexural modulus (E_f) can be determined by Equation (3.50). The second step is to evaluate the equivalent crack length (a_{eq}) in function of the current compliance (C) and the initial compliance (C_0), by using Equation (3.52) and (3.53). In the final step, the R curve can be obtained from Equation (3.54). This data reduction scheme is designated as compliance-based beam (CBB) method by de Moura [66]. In this method, crack measurements are unnecessary while registering the values of applied load and displacement. Thus the difficulty for crack monitoring faced by other schemes is overcome. Furthermore, the FPZ effects, which are pronounced in Mode II tests, are included. Moreover, the flexural modulus, E_f, can be easily calculated from the initial compliance and the initial crack length. In this approach, the only material property needed to be known in advance is G_{13}. However, its effect on the measured G_{IIc} is negligible [67], which means that a typical value can be used, and it is unnecessary to measure it. Attribute to these advantages of CBB method, it will be used to determine the Mode II fracture toughness, G_{IIc}, in this dissertation.

3.4.3 Experimental Results

To evaluate the mode II interlaminar fracture toughness, G_{IIc}, of the LAMP-built laminates, ENF tests were performed using a universal material testing machine, as illustrated in Figure 3.13. The compressive load was applied at the midspan of the specimen at a crosshead speed of $5\mu m/s$ and the loading process would not stop until the specimen was broken. As before, five groups of DCB specimens were fabricated using five different exposure times, corresponding to the cure depths of 120μm, 150μm, 200μm, 250μm and 300μm respectively. The length, width and thickness of each specimen were 70mm, 3mm and 5.8mm, respectively. A polymer film was inserted at the midplane of the laminate during the building process to form a delamination starter, and a precrack was introduced ahead of the insert front with a fine razor blade. Because crack tends to close during the ENF test and measurement of the crack length is quite difficult, the compliance-based beam (CBB) method described before will be used to determine the R-curve and G_{IIc} for each specimen. The initial crack length (a_0), which is a fundamental parameter of the CBB method, was accurately measured using an optical microscope. Since each specimen group corresponds to a certain conversion degree (α), the change of G_{IIc} with respect to the degree of conversion can be obtained.

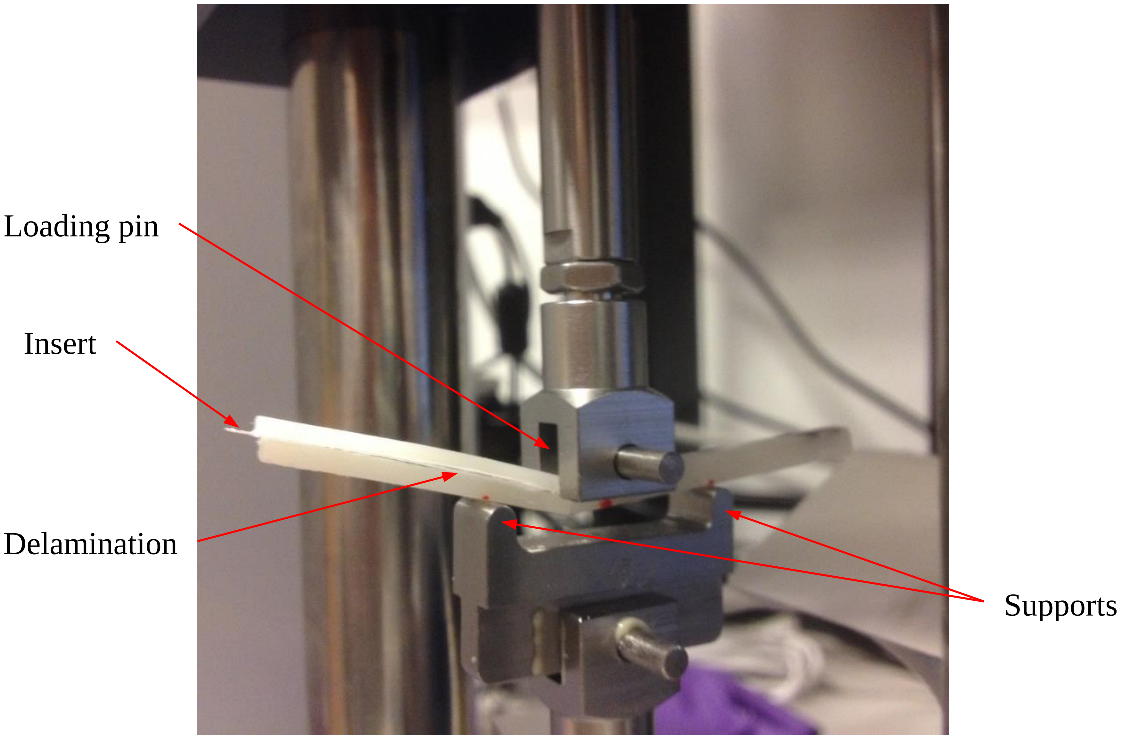

Figure 3.13 Experimental setup for ENF tests (the specimen was loaded until broken)

Figure 3.14 presents a typical $\mathrm{P}-\delta$ curve for one tested ENF specimen. As seen, the load force linearly increases with the applied displacement initially. At a certain point, deviation from linearity occurs, which indicates the damage initiation at the interface. Then the load suddenly drops due to crack propagation. When the crack front reaches the midspan of the specimen, the load force goes up again until the specimen is broken. With the measured $\mathrm{P}-\delta$ curve, a R-curve can be determined using Equations (3.50)~(3.54) in the CBB method, as shown in Figure 3.15. G_{IIini} and G_{IIc} represent Mode II energy release rate at damage initiation and during stable crack propagation, respectively. The damage initiation is defined in the $\mathrm{P}-\delta$ curve as being the point corresponding to the beginning of the nonlinear behavior. The G_{IIini} value corresponds to the onset of fracture process zone (FPZ) development at the precrack tip. The critical value of Mode II energy release rate (G_{II}) is defined by the plateau of the R-curve and it characterizes the self-similar stable crack propagation process. It must be noted that the plateau value corresponds to the input G_{IIc} in the numerical cohesive model. In Figure 3.15, it can be seen that the G_{IIc} value is around 100N/m for this tested ENF specimen.

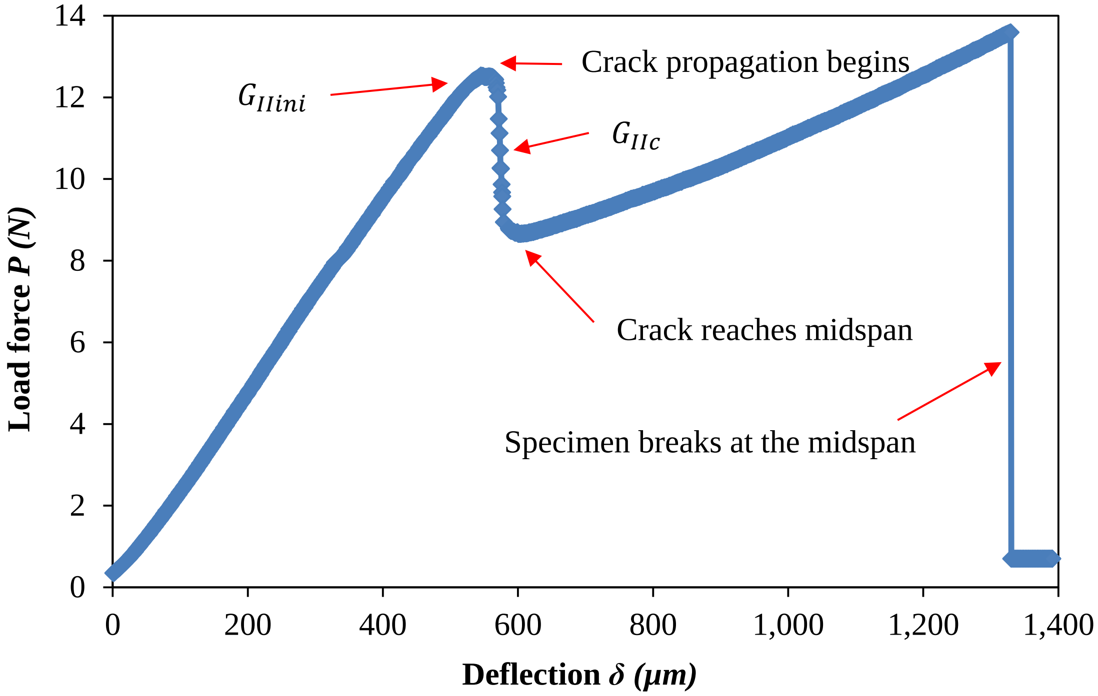

Figure 3.14 A typical $P-\delta$ curve obtained from ENF test

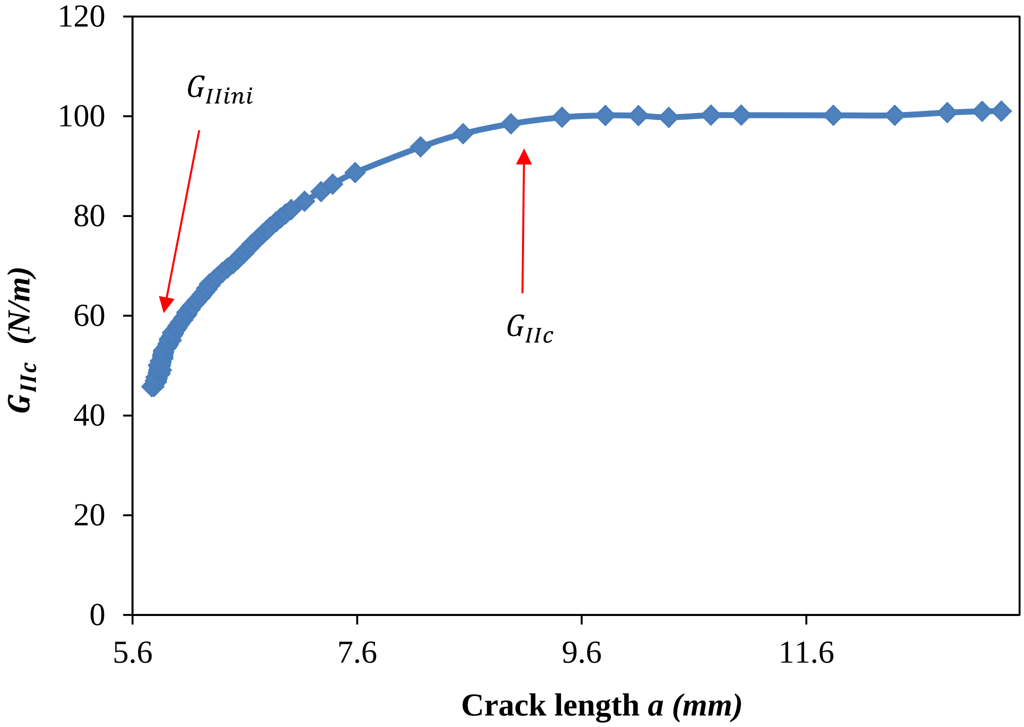

Figure 3.15 Experimental R-curve of one tested ENF specimen

The values of $\mathrm{G_{IIc}}$ are averaged for each group of specimens. Since each group corresponds to a certain cure depth and conversion degree, the change of $\mathrm{G_{IIc}}$ with respect to the degree of conversion (α) can be obtained, as illustrated in Figure 3.16. It can be seen that the value of $\mathrm{G_{IIc}}$ depends on α in a similar pattern as $\mathrm{G_{Ic}}$ and an exponential fitting curve is plotted. In the numerical simulation for predicting crack initiation and propagation in LAMP-built laminates, this exponential curve will be used to characterize the cure-dependent $\mathrm{G_{IIc}}$ in the cohesive element model.

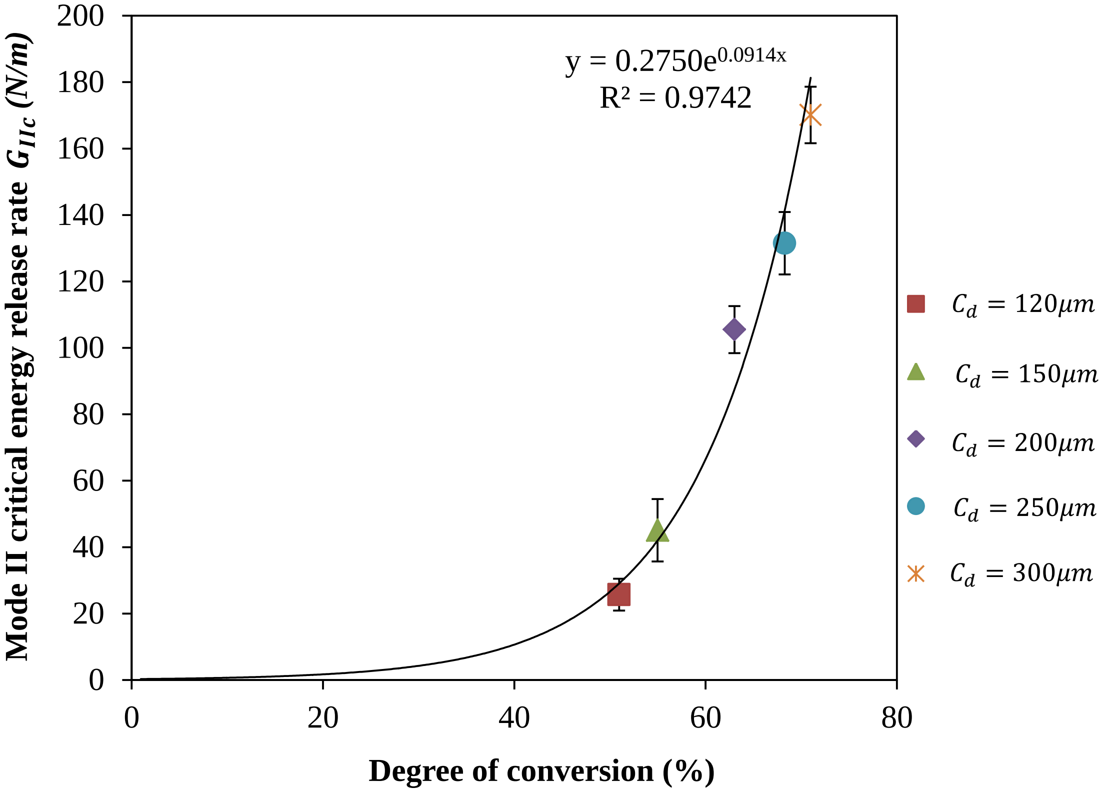

Figure 3.16 Mode II critical energy release rate vs. final conversion degree of the specimen

CHAPTER 4

COHESIVE ZONE MODEL FOR PREDICTING CRACKS AND DELAMINATION IN LAMP

Chapters 2 and 3 presented a linear elastic model for predicting residual stresses and characterized the interlaminar fracture properties, respectively. Due to the accumulated internal stresses and the relatively weak bonding at the layer interfaces, cracking/delamination may occur on parts manufactured through the LAMP process. In order to alleviate these defects and thereby achieve flawless parts, it is necessary to model the interlaminar fracture process and to predict the occurrence of delamination. To do so, a cohesive zone (CZ) model is developed in this chapter. The objective of this model is to provide a convenient, fast and yet accurate approach to analyze process-induced cracks, in order to develop possible mitigation strategies. To achieve this goal, an introduction to the fundamentals of the CZ model is given first. Then, a bilinear traction-separation law is described in detail for characterizing the constitutive behavior of a layered interface. The cohesive zone parameters that will be input to the numerical model are introduced therein. In order to obtain reasonably accurate results from CZ modeling, it is necessary to find appropriate CZ parameters. Hence, a systematic framework for obtaining CZ parameters for the layer interfaces will be presented. Finally, the cohesive zone modeling approach is pursued for LAMP to predict the occurrence of delamination.

4.1 Cohesive Zone Model

4.1.1 Introduction

The cohesive zone model method is based on the Dudgale-Barenblatt cohesive zone approach (strip-yield model), which was proposed independently by Barenblatt [48] and Dugdale [47] in the early 1960s. The strip-yield model assumes a long, slender plastic zone at the crack tip in a non-hardening material, and it approximates elastic-plastic behavior by superimposing two elastic solutions: a through crack under remote tension and a through crack with closure stresses at the tip. Since the stresses in the strip-yield zone are finite, a singularity cannot exist at the crack tip (that is, the stress intensity factor at the tip of the plastic zone must be equal to zero). Hence, the plastic zone length is determined from the condition that the closure stress and the stress intensity factors from remote tension cancel one another [42]. The Dudgale-Barenblatt cohesive zone approach was then used to analyze concrete cracking by Hillerborg [68, 69]; it is now referred to as the cohesive zone (CZ) model (or the fictitious crack model). This model assumes that the traction-separation ($t - \delta$) behavior observed in the cohesive zone is a material property. Fracture can be viewed as a gradual phenomenon in which separation takes place across the cohesive zone and is resisted by cohesive tractions [70]. The integral of tractions with respect to separations in the cohesive zone is equal to the amount of resistance to fracture, or fracture toughness (G_c), of the material. Needleman [71] considered that cohesive zone models are particularly attractive when interfacial strengths are weak when compared with the adjoining material, as is the case in composite laminates. The two adjacent elastic plies (adherends) are considered to be joined by a plane adhesive layer whose thickness is assumed to be negligible compared to both that of the joined plies and to its in-plane dimensions. Thus the adhesive layer can be conveniently schematized as an interface, i.e. a zero-thickness surface entity, which ensures displacement and stress transfer between the adherends [72]. This interface between the plies is numerically modeled by the cohesive elements. These elements are usually embedded along a pre-determined crack path (the interface between plies for composite laminates), and their constitutive behaviors are characterized by the cohesive law, which relates the traction and separation across the cracked surfaces.

Compared with the other methods used in computational fracture mechanics (e.g. the virtual crack extension technique, the energy domain integral technique and the virtual crack closure technique), CZ modeling possesses several advantages. A main advantage is that it can predict both the onset and the propagation of delamination without previous knowledge of the crack location. Hence, a finite size initial crack is not required [73]. Moreover, the CZ approach enables multiple crack paths to be modeled without computationally expensive crack-path following algorithms. In addition, it does not require the direction of crack propagation to be known in advance, and cracks have the potential to propagate along any path where cohesive elements are placed [74].

4.1.2 Bilinear Constitutive Behavior of the Interface

The constitutive behavior of an interface element is governed by the chosen cohesive law, which can be described as a traction-separation curve that relates the element stress (traction) to the relative nodal displacements (separation) at the interface. To accurately simulate the interlaminar fracture process, it is important to choose an appropriate cohesive law in the formulation of the cohesive element. Usually the traction-separation curve consists of the following main features: 1. An initial elastic region is seen in the period before maximum traction is reached; this represents the interfacial strength for damage to occur. 2. A subsequent declining region in the period after maximum traction is reached; this indicates decreasing resistance (the so-called softening behavior) of the damaged element during separation. The cohesive zone can still transfer loads after the onset of damage by following the softening behavior. When the separation reaches a critical value, complete failure of the cohesive element results, and no loads can be transferred across the fracture surfaces. 3. The total area enclosed by the curve is equal to the fracture toughness of the material.

Although a variety of geometric shapes have been proposed for the traction-separation curve (e.g. linear elastic-exponential softening, cubic polynomial, trapezoidal), a bilinear form is commonly implemented to model composite delamination [74] because it is simple to implement. Figure 4.1 illustrates a typical bilinear constitutive material behavior for pure Mode I loading. As can be seen from the figure, a high initial stiffness (penalty stiffness K_n) is used to hold the top and bottom faces of the cohesive element together in the linear elastic range (between point 0 and point 2). Within this linear elastic range, point 1 is subjected to a low tensile load, and no damage occurs. At point 2, the interfacial normal traction, t_n, reaches the Mode I interlaminar strength of the material, t_n^0, and thus damage initiates in the element. As the separation increases at the interface, the cohesive element accumulates damage, and the traction is lower than the strength (point 3). The strain energy, G_I, released at point 3 can be represented by the area of the triangle 0-2-3. If the load were to reverse, point 3 would unload to the origin (point 0). Due to the irreversible damage accumulation (the level of damage is evaluated by the parameter D), the stiffness of the interface drops to $(1-D)K_n$ and cannot be restored to the original value. The portion between point 2 and point 4 on the traction-separation curve is called the softening region, since the stiffness is gradually reduced to zero. At point 4, the separation reaches its critical value, δ_n^f, and complete failure of the cohesive element occurs. Meanwhile, the critical energy release rate G_{Ic} is attained. In other words, all the available interfacial fracture energy has been completely consumed. The area under the traction-separation curve is

$$\int_0^{\delta_n^f} t_n d\delta_n = G_{Ic} \tag{4.1}$$

For bilinear cohesive behavior, the failure separation, δ_n^f, can be obtained as

$$\delta_n^f = 2G_{Ic}/t_n^o \tag{4.2}$$

For any separation larger than point 4, the interface does not carry any load (point 5), and the fracture surfaces completely debond. Note that the delamination tip is not defined explicitly when a softening response is used to model delamination. While the onset of damage occurs at point 2, the delamination tip could be defined as the point where the traction at the interface is zero, which is point 4.

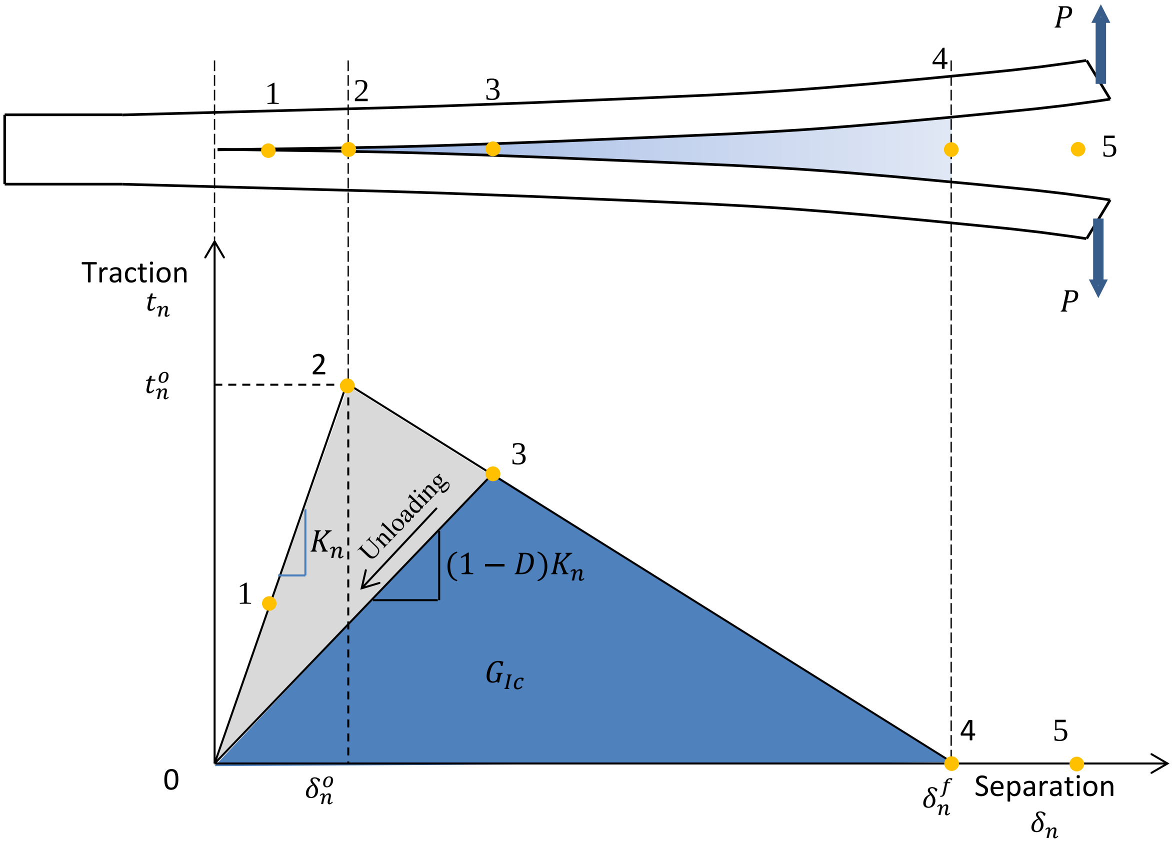

Figure 4.1 Bilinear traction-separation law. The superscripts "o" and "f" refer to onset of damage and failure of element, respectively.

4.1.3 Cohesive Damage Model for Pure Mode I / II

In the previous subsection, the interfacial constitutive law, which takes the form of a bilinear relation between interfacial traction and separation, has been discussed for Mode I fracture. In fact, the same concepts can be applied to the case of Mode II fracture, although the values of CZ parameters are different from those in Mode I. This subsection gives the complete formulation for the cohesive damage model in pure mode. This forms the basis for the formulation of the mixed-mode model.

In order to take into account the irreversibility of damage, the maximum relative displacement attained during the loading history, δ^{max}, is defined as

$$Mode\ I: \qquad \delta_n^{max} = max\{\delta_n^{max}, \delta_n\}, \qquad with\ \delta_n^{max} \geq 0 \tag{4.3}$$

$$Mode\ II: \qquad \delta_s^{max} = max\{\delta_s^{max}, |\delta_s|\} \tag{4.4}$$

where $\delta_n^{max} \geq 0$ because pure compressive deformation does not produce damage.

The irreversible bilinear constitutive behavior shown in Figure 4.1 can be formulated as

$$t_i = \begin{cases} K_i\delta_i & \Leftarrow \quad \delta_i^{max} \leq \delta_i^o \\ (1 - D_i)K_i\delta_i & \Leftarrow \quad \delta_i^o < \delta_i^{max} < \delta_i^f \\ 0 & \Leftarrow \quad \delta_i^{max} \geq \delta_i^f \end{cases} \tag{4.5}$$

$$D_i = \frac{\delta_i^f(\delta_i^{max} - \delta_i^o)}{\delta_i^{max}(\delta_i^f - \delta_i^o)}, i = n, s;\ D_i \in [0,1] \tag{4.6}$$

where, the subscripts “n” and “s” represent Mode I (normal traction and separation) and Mode II (in-plane shear traction and separation), respectively. K_i is the cohesive stiffness and is equal to t_n^o/δ_n^o. The scalar damage variable, D_i, represents the damage in the material for each mode. It initially has a value of 0. If damage evolution is modeled, D_i monotonically evolves from 0 to 1 upon further loading after the initiation of damage.

It can be seen that the properties required to describe the damage model are the cohesive stiffness, K, the fracture toughness, G_c, and the interlaminar strength, t^o, for each pure mode.

4.1.4 Mixed-mode Cohesive Damage Model

In many situations a more complex loading condition is present, and a mixed-mode analysis is necessary instead of a single mode analysis. For the application in LAMP, a mixed-mode damage model including Mode I and Mode II is considered in the following. This mixed-mode model is based on the pure mode model described above.

In the cohesive element, the process of damage begins when the stresses and/or strains satisfy certain damage initiation criteria. Under pure Mode I or Mode II loading, the onset of damage can be determined simply by comparing the traction components with their respective allowables. However, under mixed-mode loading, damage initiation and the corresponding softening process may occur before any of the involved traction components reach their respective allowables. Over the past several decades, various damage initiation criteria have been developed, such as the maximum nominal stress criterion, the maximum nominal strain criterion, and the quadratic nominal strain criterion. In this study, to account for the interaction of traction components, it is assumed that the damage onset at the interface can be predicted using the following quadratic nominal stress criterion [75]

$$\left\{\frac{\langle \mathrm{t_n} \rangle}{\mathrm{t_n^{\mathit{o}}}}\right\}^2 + \left\{\frac{\mathrm{t_s}}{\mathrm{t_s^{\mathit{o}}}}\right\}^2 = 1 \tag{4.7}$$

where t_n and t_s represent the normal and in-plane shear tractions, respectively. The corresponding separations are denoted by δ_n and δ_s, respectively. The quantities t_n^o and t_s^o, which have been introduced before, represent the interfacial strengths for Mode I and Mode II, respectively. The Macaulay bracket $\langle\ \ \rangle$ is used to signify that a pure compressive deformation or stress state does not affect damage onset. In other words,

$$\langle t_n \rangle = \begin{cases} 0 & \Leftarrow \quad t_n \leq 0 \\ t_n & \Leftarrow \quad t_n > 0 \end{cases} \tag{4.8}$$

In order to describe the evolution of damage under a combination of normal and shear separation across the interface, it is useful to introduce a mixed-mode effective displacement [76], δ_m, which is defined as

$$\delta_m = \sqrt{\langle \delta_n \rangle^2 + \delta_s^2} \tag{4.9}$$

For an opening separation δ_n larger than zero, a mode mixity ratio, β, can be defined to quantify the relative proportions of normal and shear deformation in the cohesive zone:

$$\beta = \frac{\delta_s}{\delta_n} \tag{4.10}$$

Then, the mixed-mode effective displacement corresponding to the onset of damage, δ_m^o, can be expressed as the form

$$\delta_m^o = \begin{cases} \delta_n^o \delta_s^o \sqrt{\dfrac{1+\beta^2}{(\delta_s^o)^2 + (\beta\delta_n^o)^2}} & \Leftarrow \quad \delta_n > 0 \\ \delta_s^o & \Leftarrow \quad \delta_n \leq 0 \end{cases} \tag{4.11}$$

The failure criteria used to predict delamination propagation under mixed-mode loading conditions are usually established in terms of an interaction between the energy release rates in the individual (normal and in-plane shear) modes. The power law criterion is the one most widely used and can be expressed as [77]

$$\left\{\frac{G_I}{G_{Ic}}\right\}^{\alpha} + \left\{\frac{G_{II}}{G_{IIc}}\right\}^{\alpha} = 1 \tag{4.12}$$

where G_I and G_{II} represent the energies dissipated during the damage process in Mode I and Mode II, respectively. G_{Ic} and G_{IIc} refer to the corresponding critical energy release rates. It is reported that the power law criterion using $\alpha = 1$ provides reasonable results for the prediction of mixed-mode fracture of composites. Thereby, $\alpha = 1$ will be used in this study.

The mixed-mode effective displacement corresponding to the complete failure of the interface, δ_m^f, can be obtained from the above equations as

$$\delta_m^f = \begin{cases} \dfrac{2(1+\beta^2)}{K\delta_m^o}\left[\left(\dfrac{1}{G_{Ic}}\right)^{\alpha} + \left(\dfrac{\beta^2}{G_{IIc}}\right)^{\alpha}\right]^{-1/\alpha} & \Leftarrow \quad \delta_n > 0 \\ \delta_s^f & \Leftarrow \quad \delta_n \leq 0 \end{cases} \tag{4.13}$$

The constitutive behavior for mixed-mode loading can be formulated as a function of the cohesive stiffness, K, the overall damage variable, D, and the mixed-mode effective displacements corresponding to the damage onset and complete failure, δ_m^f and δ_m^o, as [77, 78]

$$t_i = \begin{cases} K_i\delta_i & \Leftarrow \quad \delta_m^{max} \leq \delta_m^o \\ (1-D)K_i\delta_i & \Leftarrow \quad \delta_m^o < \delta_m^{max} < \delta_m^f \\ 0 & \Leftarrow \quad \delta_m^{max} \geq \delta_m^f \end{cases} \tag{4.14}$$

$$D = \frac{\delta_m^f(\delta_m^{max} - \delta_m^o)}{\delta_m^{max}(\delta_m^f - \delta_m^o)}\ , D \in [0,1] \tag{4.15}$$

where $i = n$ or s denotes the tractions and separations in the normal or shear direction. The quantity δ_m^{max} refers to the maximum value of the mixed-mode effective displacement attained during the loading history, and it is the only state variable used to track the damage at the interface.

The mixed-mode response of cohesive elements can be illustrated in a single three-dimensional map by representing Mode I on the Y-Z plane and Mode II on the X-Z plane, as shown in Figure 4.2. The triangles $0 - t_n^o - \delta_n^f$ and $0 - t_s^o - \delta_s^f$ in the two vertical coordinate planes represent the bilinear behavior under pure normal and pure shear deformation, respectively. All intermediate vertical planes represent the cohesive damage response under mixed-mode conditions with different mode mixes.

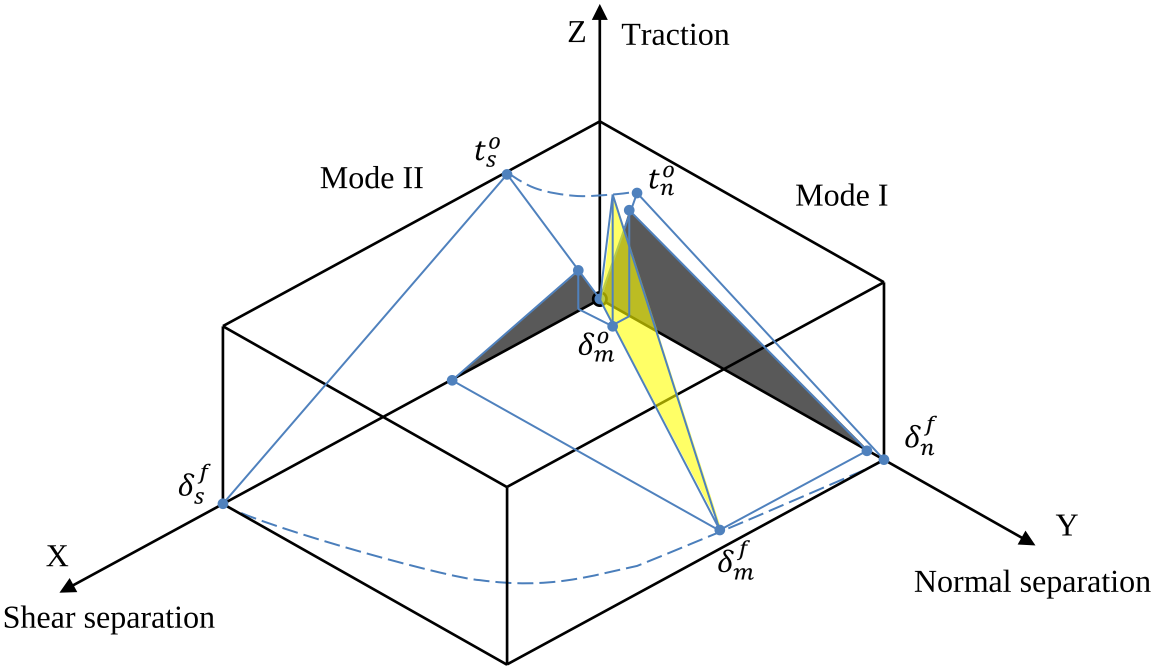

Figure 4.2 Illustration of mixed-mode response in cohesive elements

4.2 Cohesive Parameters

In order to fully characterize the bilinear traction-separation ($t - \delta$) law (Figure 4.1) that governs the behavior of cohesive elements, three independent parameters are required: The critical energy release rate G_c (represented by the area of the triangle enclosed by the $t - \delta$ curve), the interfacial strength t^o (represented by the height of the triangle), and the cohesive stiffness K (represented by the initial slope of the triangle). To establish the mixed-mode damage model, these three cohesive parameters must be determined for both Mode I and Mode II. They will be considered as the input data parameters to the mixed-mode model in numerical simulations. The values of G_c are obtained through experimental tests, i.e. DCB tests for Mode I and ENF tests for Mode II. The other two cohesive parameters, t^o and K are determined by a calibration method [57, 79-82], in which DCB and ENF tests are numerically simulated and the simulation results are matched with the experiment results. Details about this systematic framework to obtain cohesive parameters for each pure mode are presented in this section.

4.2.1 Mode I Cohesive Parameters

In order to determine the Mode I cohesive parameters, a 2D plane strain finite element (FE) model is developed for simulating the DCB test, as shown in Figure 4.3. To simulate the displacement-controlled loading process in an experiment, a displacement boundary condition along the Y-axis is applied to one node at the top surface of the specimen. The reaction force at this node will be recorded together with the displacement, so as to plot a numerical load-deflection ($P - \delta$) curve that can be compared with the values that were obtained experimentally [57, 81]. Another opposing node at the bottom surface is constrained in all degrees of freedom. A precrack is introduced at the middle plane of the specimen. Ahead of the precrack tip, a layer of cohesive elements is placed along the interface between the two DCB arms. In this section, all of the experimental tests are conducted for specimens built with the processing parameter C_d (cure depth) equal to $200\mu m$. The final conversion degree of the bulk material is 63.01%, and the corresponding elastic mechanical properties can be found in Figure 2.10. Note that the specimen is built in 56 layers, which is sufficient for the conversion degree and thereby cure-dependent mechanical properties to be considered as constants for the entire specimen during the DCB test. The value of the Mode I fracture toughness, G_{Ic}, is $12.8N/m$, obtained from experiments. A plane strain element of four nodes (CPE4) is used to model the sublaminates, and four-node cohesive elements COH2D4 are used for the initially uncracked interface. As mentioned before, the cohesive elements are characterized by a bilinear cohesive law, for which the cohesive parameters will be determined in the following.

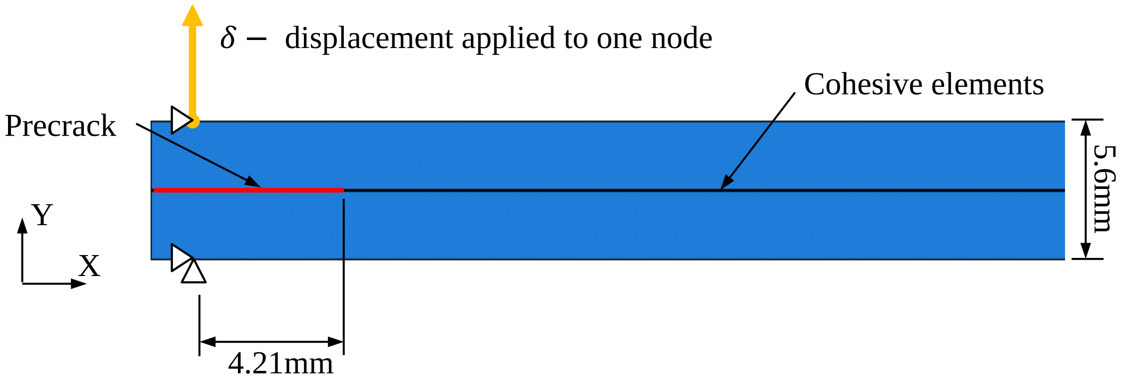

Figure 4.3 Schematic of 2D plane strain finite element model for the DCB test

The cohesive element size along the length direction of the beam is held at the same value as the bulk element. The aspect ratio of the bulk element is controlled to be constant and within acceptable limits. In order to determine an appropriate value for the element size, a mesh convergence study is conducted on this DCB model by changing the mesh density (i.e. by changing number of rows of elements in each DCB arm). The width of the DCB specimen modeled here is 8mm, and the other dimensions of the specimen can be found in Figure 4.3. In Figure 4.4, the load-deflection ($P - \delta$) curves obtained with different mesh densities are illustrated. For each $P - \delta$ curve, it can be observed that the load increases rapidly in an approximately linear manner up to a peak load, and then gradually drops due to crack propagation. Obviously, it is not sufficient to have only one row of elements in each DCB arm, because of the zigzag-shaped curve during crack growth that indicates instability. Note that for the other models with different mesh densities, there are small differences in the initial slopes and the peak loads of the $P - \delta$ curves. The maximum variation in the slope and the peak load is 9.6% and 8.7%, respectively. Here, the peak load is used as the convergence parameter, and Figure 4.5 shows the mesh convergence results.

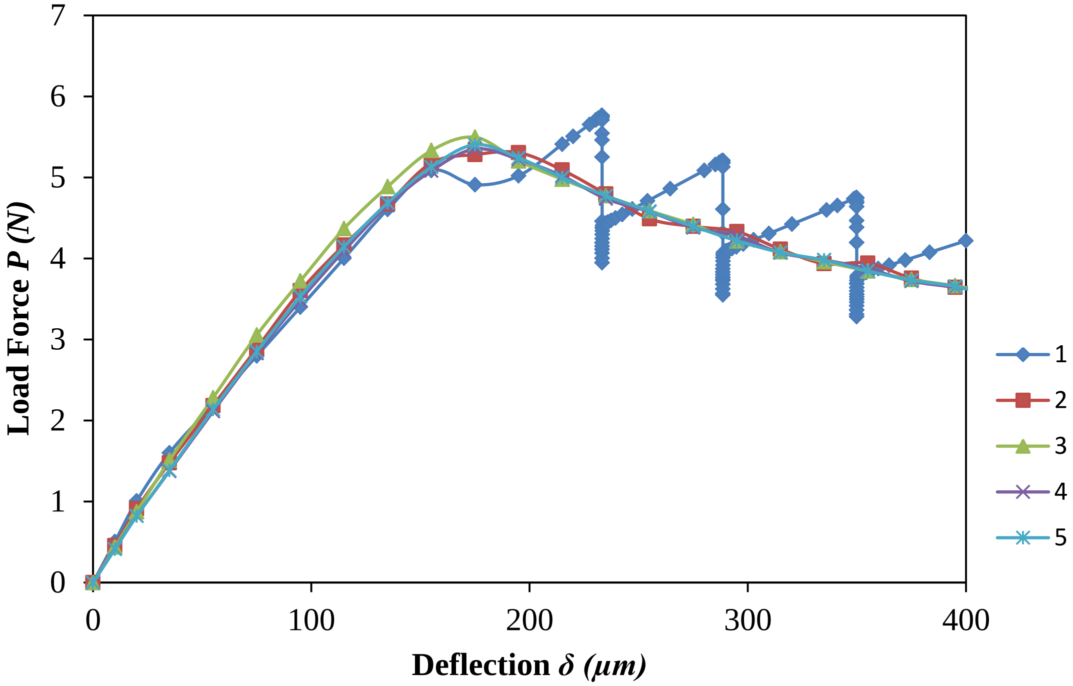

Figure 4.4 Numerical $P-\delta$ curves for different mesh densities (different numbers of rows of elements in one DCB arm)

In this figure, the relative difference in percentage is computed for two adjacent data points of peak load. It can be seen that, for the FE models with four and five rows of elements in one DCB arm, the relative difference of peak loads is within 1%. Therefore, the present FE model with five rows of finite elements in each DCB arm has a good convergence property and stability, and it will be used to search for appropriate cohesive parameters.

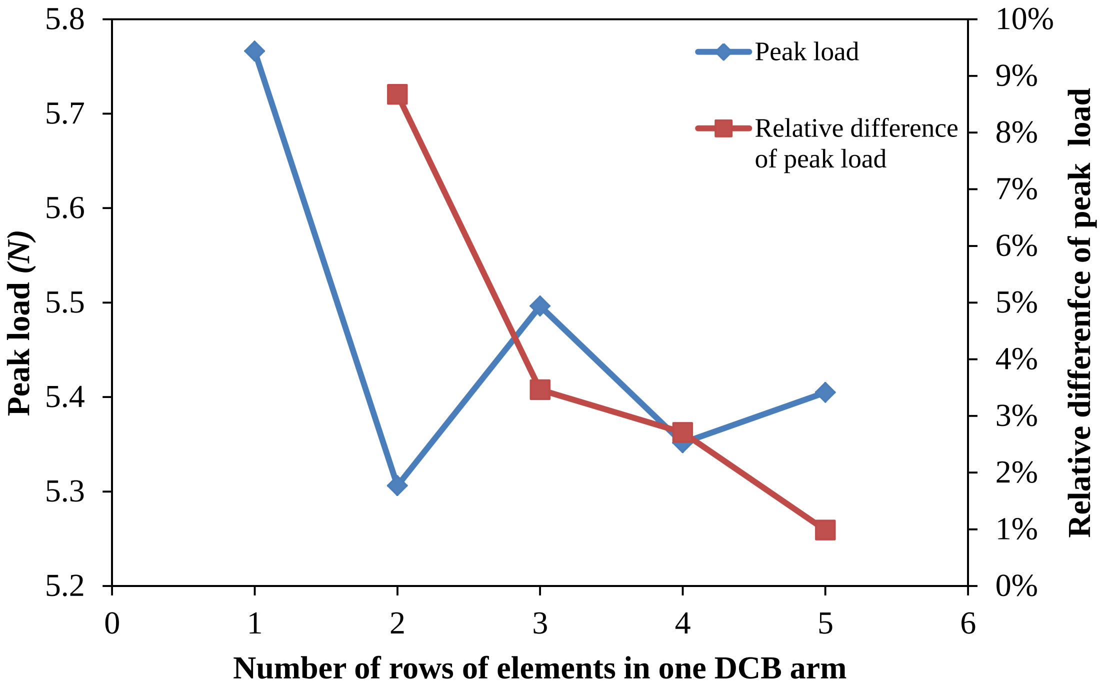

Figure 4.5 Mesh convergence study for the FE model of DCB test (“Peak load” is the maximum value of applied force in the $P-\delta$ curve; “Relative difference of peak load” is the relative difference in percentage between two adjacent data points of peak load

Mode I cohesive parameters, t_n^o and K_n, can be obtained by simulating the DCB test and matching the numerical load-deflection $(P-\delta)$ curves with experimental ones. By doing so, the correctness of the experimentally measured fracture toughness can also be verified. Figure 4.6 illustrates several numerical load-deflection $(P-\delta)$ curves obtained from DCB models with different interfacial normal strength (maximum normal traction t_n^o) of the cohesive element. It can be seen that increasing t_n^o results in greater critical force (peak load), at which the crack begins to propagate. Moreover, t_n^o determines the point of deviation from linearity in the $P-\delta$ curve, which corresponds to the damage initiation of cohesive elements. When the value of t_n^o becomes too large (in this case, 4MPa), the zigzag-shaped $P - \delta$ curve during propagation indicates the numerical instability and convergence difficulty for solving the FE model. For values of t_n^o smaller than 0.1MPa, a peak indicating the crack growth cannot be observed. Therefore, the range for seeking an appropriate value of t_n^o is from 0.1MPa to 4MPa.

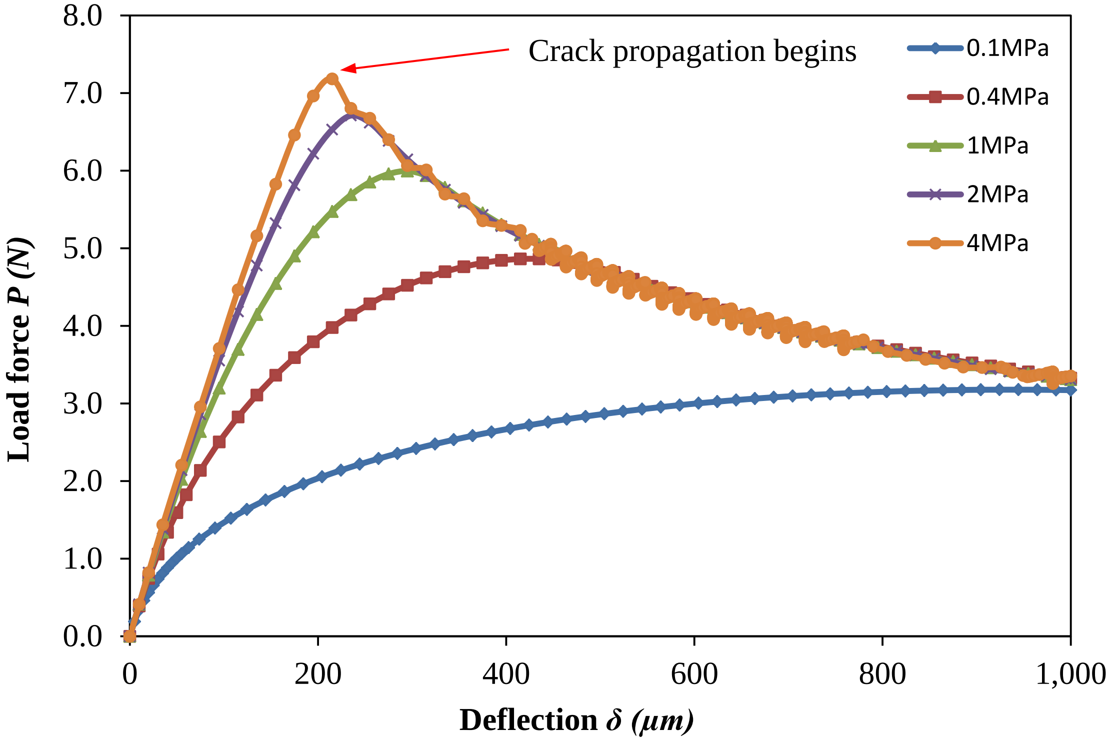

Figure 4.6 Numerical $P - \delta$ curves for DCB models with different interfacial strengths t_n^o

On the other hand, Figure 4.7 shows the $P - \delta$ curves obtained for the same test but now the interface stiffness is changed and the interfacial strength is fixed at $t_n^o =$ 2MPa in the FE model. As seen in this figure, increase in the cohesive stiffness (K_n) increases the initial slope of the $P - \delta$ curve before crack propagation. For the values of

K_n lager than $10^5 \mathrm{N/mm^3}$, one cannot identify any difference because the curves are too close. When K_n becomes smaller than $50 \mathrm{N/mm^3}$, numerical problems occur, and the results cannot converge during crack propagation. Thus the appropriate value of K_n falls between $50 \mathrm{N/mm^3}$ and $10^5 \mathrm{N/mm^3}$.

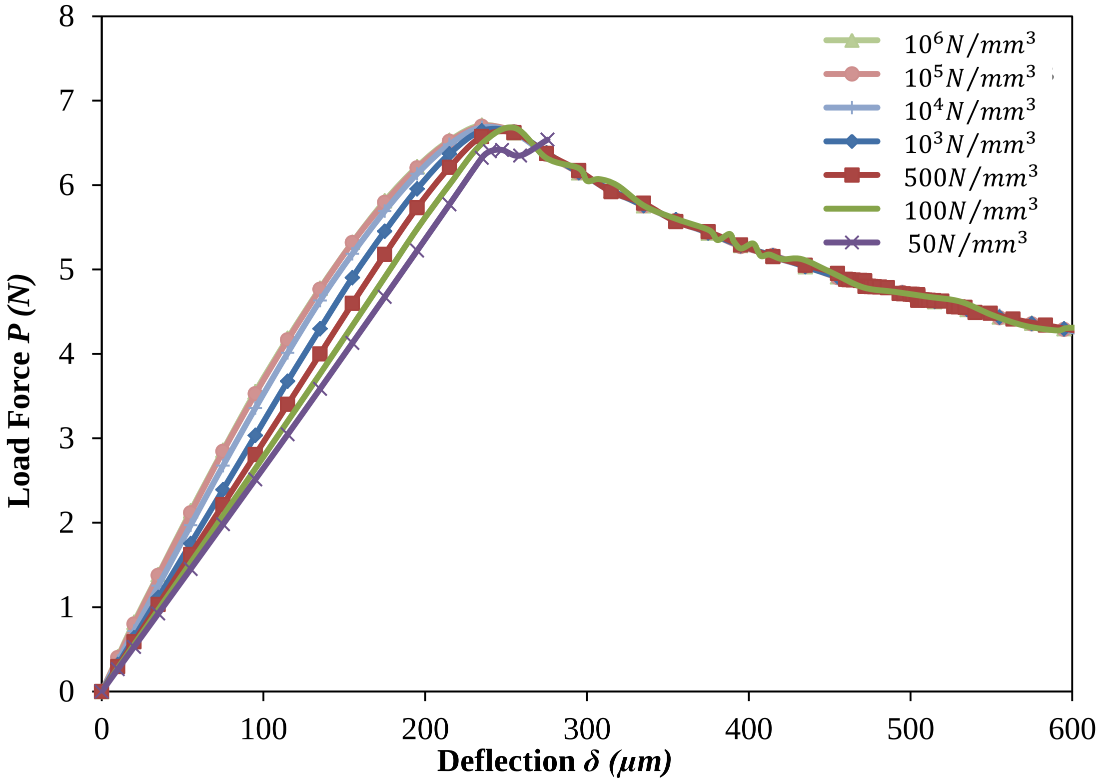

Figure 4.7 Numerical $P-\delta$ curves for DCB models with different cohesive stiffness K_n

Hence, by matching the slope of the initial straight line and the peak load to the experimental values in the $P-\delta$ curves with the lowest error, appropriate values of these two cohesive parameters can be determined. This process begins with simulations in which t_n^o is kept constant while K_n is varied. Once the initial slope of the numerical $P-\delta$ curve is matched with the experimental one, t_n^o is varied until the peak load value matches experimentally obtained values. It can be seen from Figure 4.8 that, when K_n is equal to $8\times10^3\mathrm{N/mm^3}$ and t_n^o is equal to 1.7MPa, the simulation results agree with experiments. Moreover, good consistency between the numerical and experimental curves also testifies to the correctness of the experimentally measured G_{Ic}.

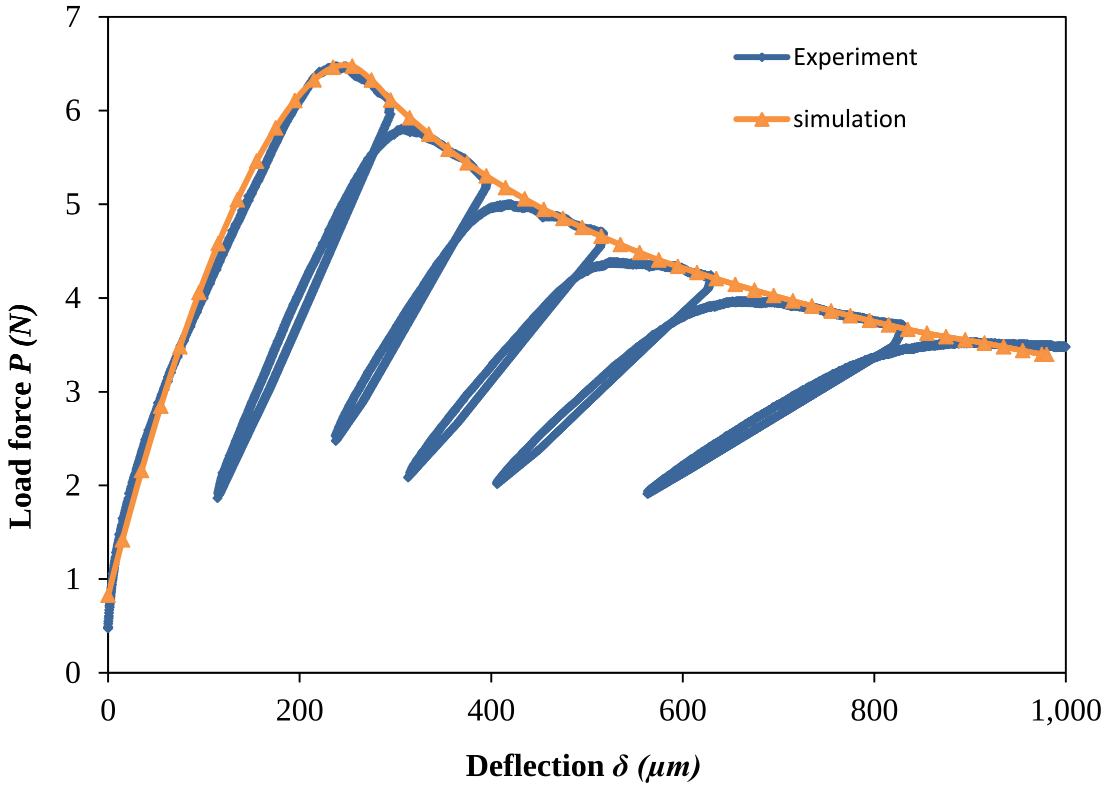

Figure 4.8 Comparison of experiments with simulation results, for which $K_n = 8\times10^3\mathrm{N/mm^3}$ and $t_n^o = 1.7\mathrm{MPa}$ in the corresponding cohesive element model.

4.2.2 Mode II Cohesive Parameters

By employing the experimentally obtained Mode II fracture toughness G_{IIc}, numerical simulations using FEM with cohesive elements are performed to analyze the delamination propagation process of ENF specimens and to determine the Mode II cohesive parameters. As seen in Figure 4.9, a 2D plane strain model is created to simulate the ENF test. Two analytical rigid circles are used to act as the support pins and another one is used to simulate the roller pin for loading the specimen. On each support, the displacement is constrained in the vertical direction, and a downward displacement is applied on the load pin (actuator). Contact conditions are imposed to simulate the interaction between the actuator/supports and the ENF specimen, and they are also defined at the interface to avoid interpenetration of the specimen arms. A precrack is introduced at the mid-plane of the model, and cohesive elements are placed at the un-cracked region. Four-node plane strain elements (CPE4) and four-node cohesive elements COH2D4 are used to model the arms and the initially uncracked interface, respectively. As before, a bilinear cohesive law governs the constitutive behavior of these cohesive elements. The width of the ENF specimen modeled here is 3mm, and the other major dimensions of the specimen can be found in Figure 4.9. Since the ENF specimens are produced with the same procedures and parameters as those of the DCB specimens, the elastic mechanical properties are of the same values too. Note that the Mode II fracture toughness, G_{IIc}, is $105.5 N/m$, obtained from experiments.

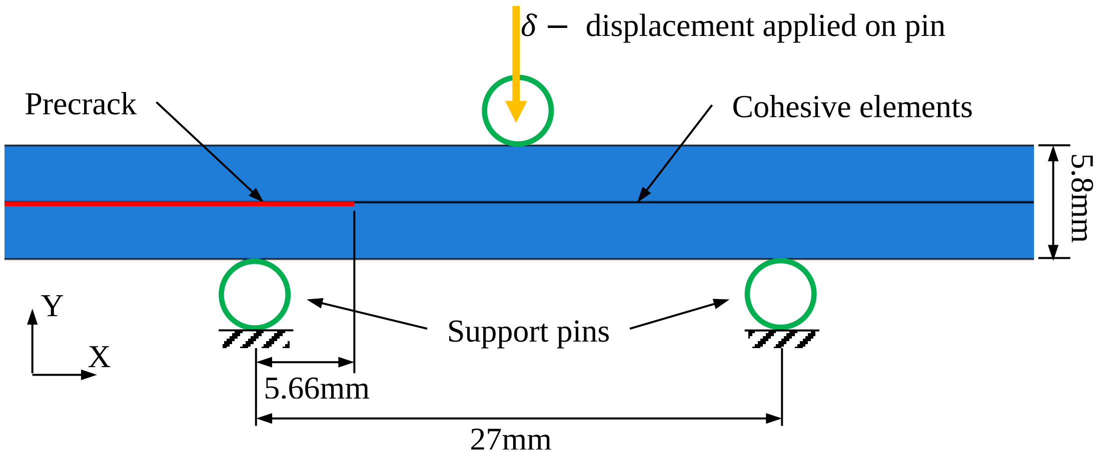

Figure 4.9 Schematic of 2D plane strain finite element model for the ENF test

A typical contour graph showing the Mises stress in a loaded ENF specimen is shown in Figure 4.10. Note that the geometrical mismatch between the left edges of two ENF arms is evidence of Mode II in-plane shear at the interface. As before, in order to examine the mesh convergence of the FE model, simulations are conducted with different mesh densities, by changing the number of rows of elements in one ENF arm while keeping the aspect ratio of elements constant. The obtained load-deflection $(P - \delta)$ curves are shown in Figure 4.11. For each $P - \delta$ curve, it can be observed that the load increases with applied displacement in an approximately linear way up to a peak load and then suddenly drops when the crack begins to propagate. Obviously, it is not sufficient to have only one row of elements in each ENF arm, since the corresponding $P - \delta$ curve has a large deviation from the other curves. Note that for the FE models with different mesh densities, there are small differences in the initial slopes and the peak loads of the

$P-\delta$ curves. The maximum variation in the slope and the peak load is 8.0% and 7.7%, respectively. Here, the peak load is used as the convergence parameter for different mesh densities, and the results are shown in Figure 4.12.

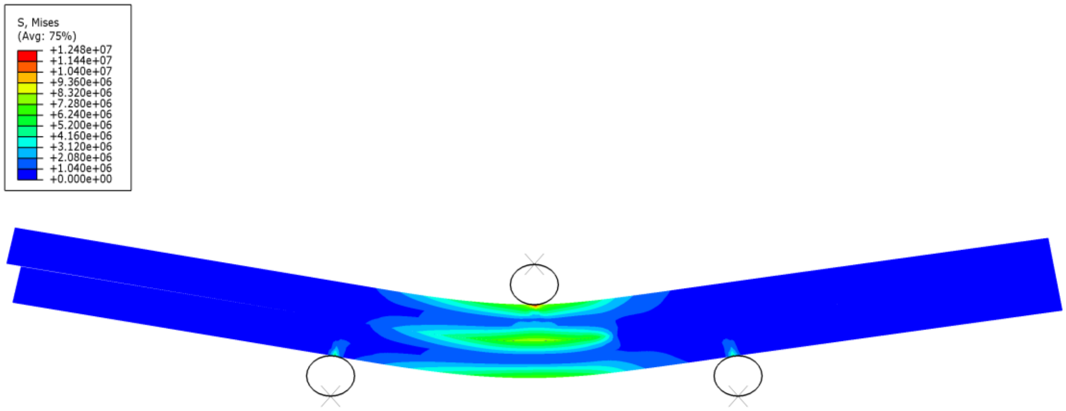

Figure 4.10 Simulation results of the Mises stress in an ENF specimen

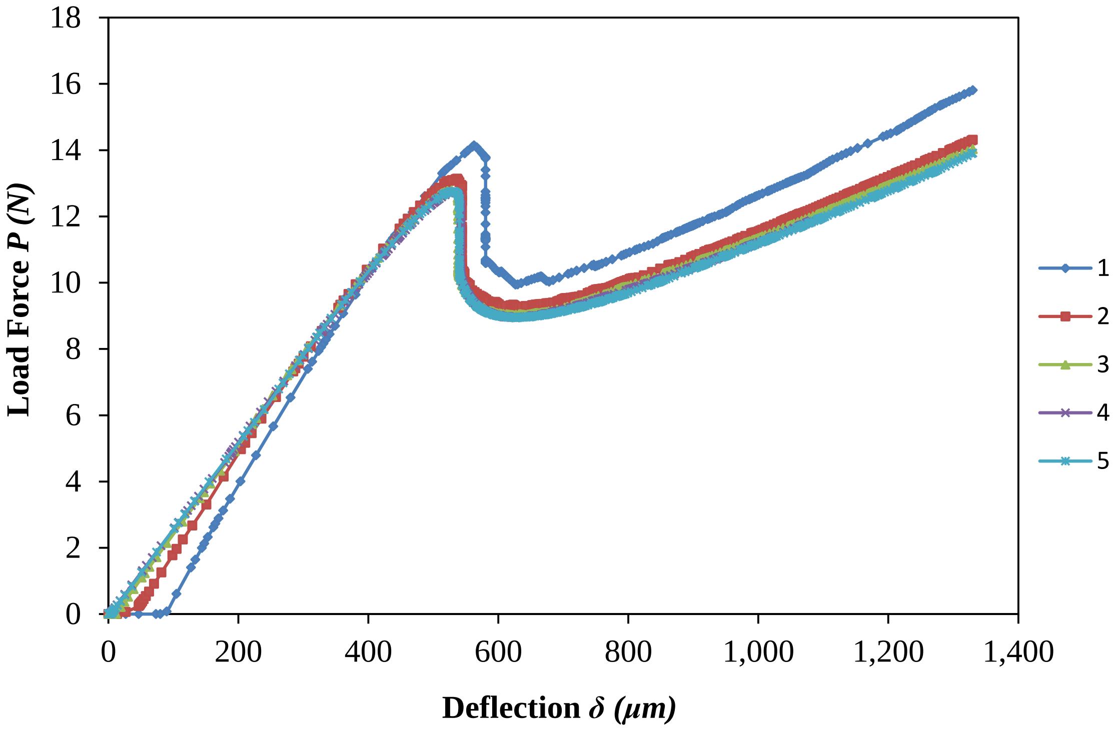

Figure 4.11 Numerical $P-\delta$ curves for different mesh densities (different numbers of rows of elements in one ENF arm).

As seen in Figure 4.12, the relative difference of peak load drops to within 1% when the FE model has more than four rows of elements in one ENF arm. Therefore, at least four rows of finite elements are required in each ENF arm for the ENF simulation results to converge.

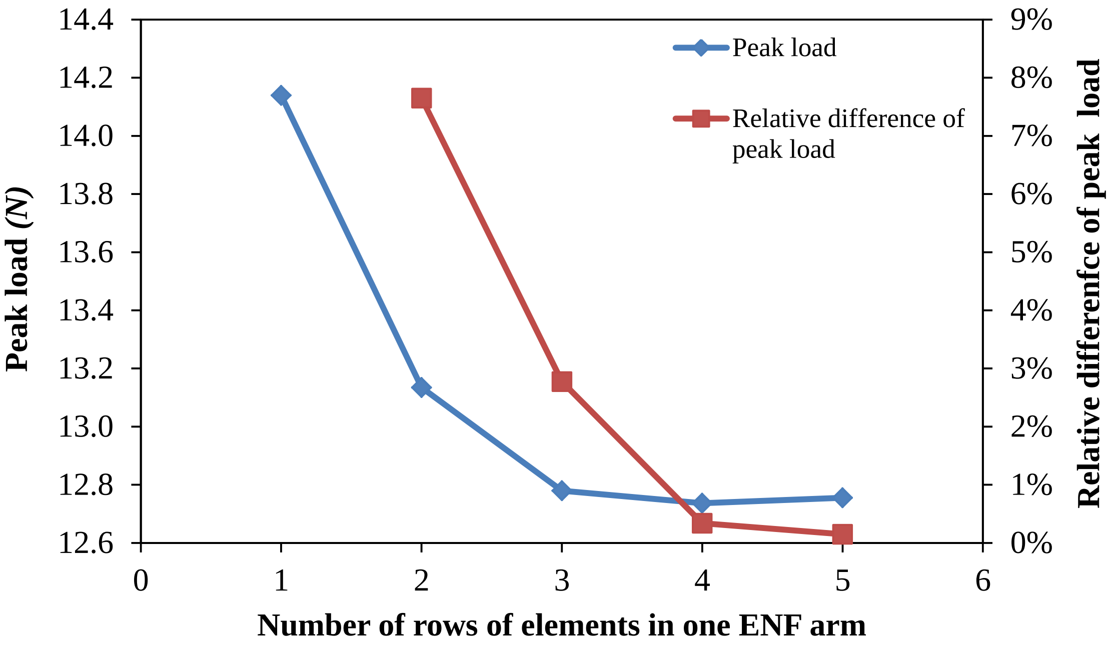

Figure 4.12 Mesh convergence study for the FE model of ENF test (“Peak load” is the maximum value of applied force in the $P-\delta$ curve; “Relative difference of peak load” is the relative difference in percentage between two adjacent data points of peak load

Appropriate cohesive parameters for Mode II delamination, the interfacial shear strength t_s^o and the interfacial shear stiffness K_s, can be determined by matching the load-deflection $(P-\delta)$ curves obtained from simulations with experimental data. As illustrated in Figure 4.13, the value of peak load, which indicates delamination growth, would go up if t_s^o were increased. Furthermore, t_s^o determines the point at which the $P-\delta$ curve becomes nonlinear, corresponding to the onset of damage in cohesive elements. When t_s^o becomes larger than 5MPa, there exists a convergence difficulty for solving the FE model. When t_s^o is less than 1MPa, the deviation from linearity occurs very early in the curve, and it is not possible to observe the peak indicating the crack propagation. Hence, the appropriate value of t_s^o should be between 1MPa and 5MPa.

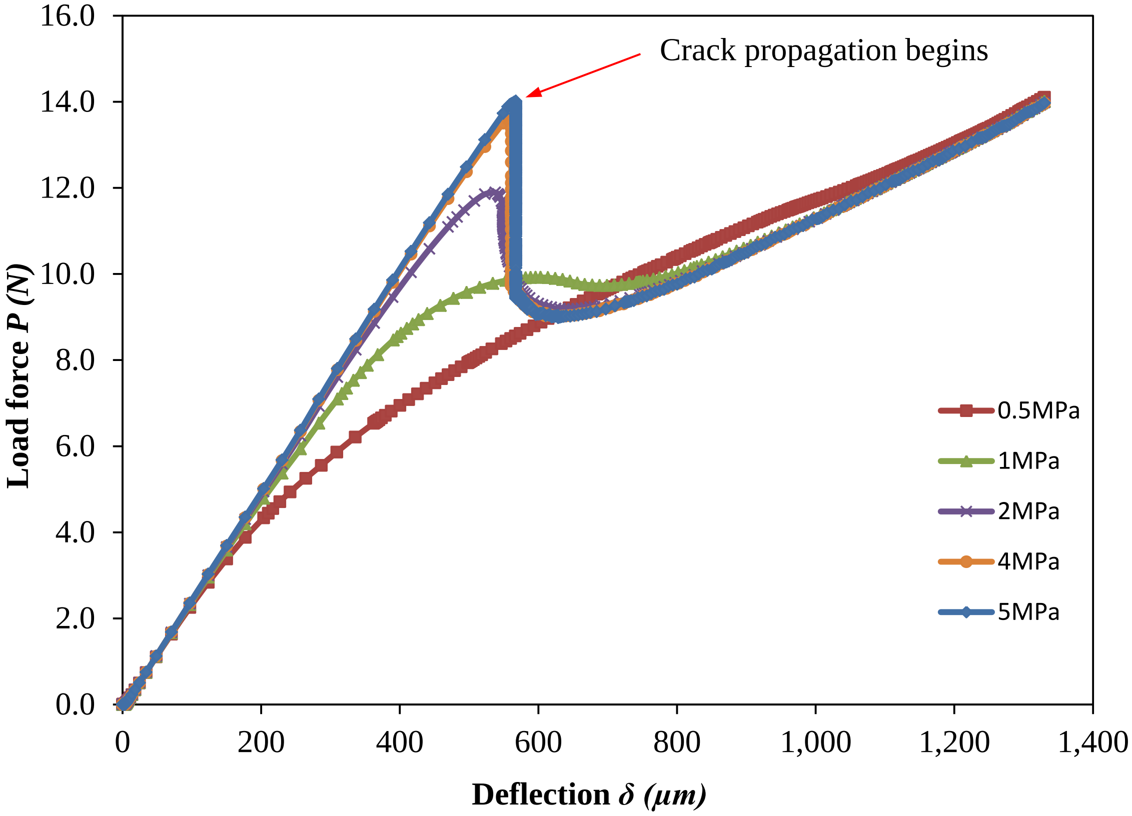

Figure 4.13 Numerical $P-\delta$ curves for ENF models with different interfacial strengths t_s^o

In contrast, by changing the interface stiffness K_s while keeping the interfacial shear strength t_s^o constant, $P-\delta$ curves can be obtained for the same test, as illustrated in Figure 4.14. It can be seen that with increasing K_s, both the initial slope and peak load of the $P-\delta$ curve increase. For the FE models with K_s greater than $10^4\mathrm{N/mm}^3$, the $P-\delta$ curves are too close for differences to be observed. When K_s is less than $50\mathrm{N/mm}^3$, the curves will flatten out, and no peak load can be identified. Hence the appropriate value of K_s will be sought in the range of $50\mathrm{N/mm}^3$ to $10^4\mathrm{N/mm}^3$.

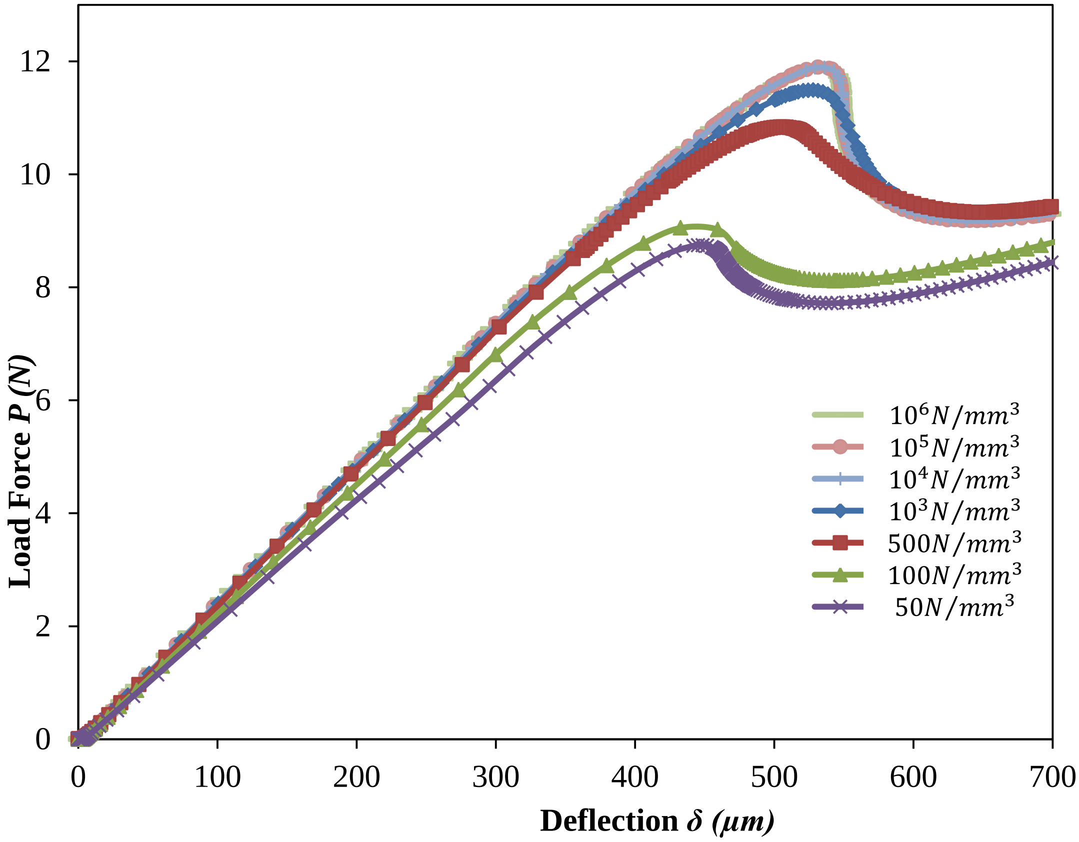

Figure 4.14 Numerical $P-\delta$ curves for ENF models with different cohesive stiffness K_s

Appropriate values of the Mode II cohesive parameters, t_s^o and K_s, can be estimated by matching the slope of the initial straight line and the peak load to the experimental ones in the $P-\delta$ curves. A procedure similar to that used for Mode I is adopted. t_s^o and K_s are varied until the simulation matches the experimental results. As seen in Figure 4.15, when K_s is equal to 7.5× $10^2\text{N}/\text{mm}^3$ and t_s^o equals 4.6MPa, the simulation results agree with the experiments. After the delamination propagates, the numerical $P-\delta$ curve deviates slightly from the experimental results, indicating that a small error may exist for the experimentally measured Mode II fracture toughness G_{IIc}. However, this small deviation is acceptable and thus the correctness of the measured G_{IIc} is verified.

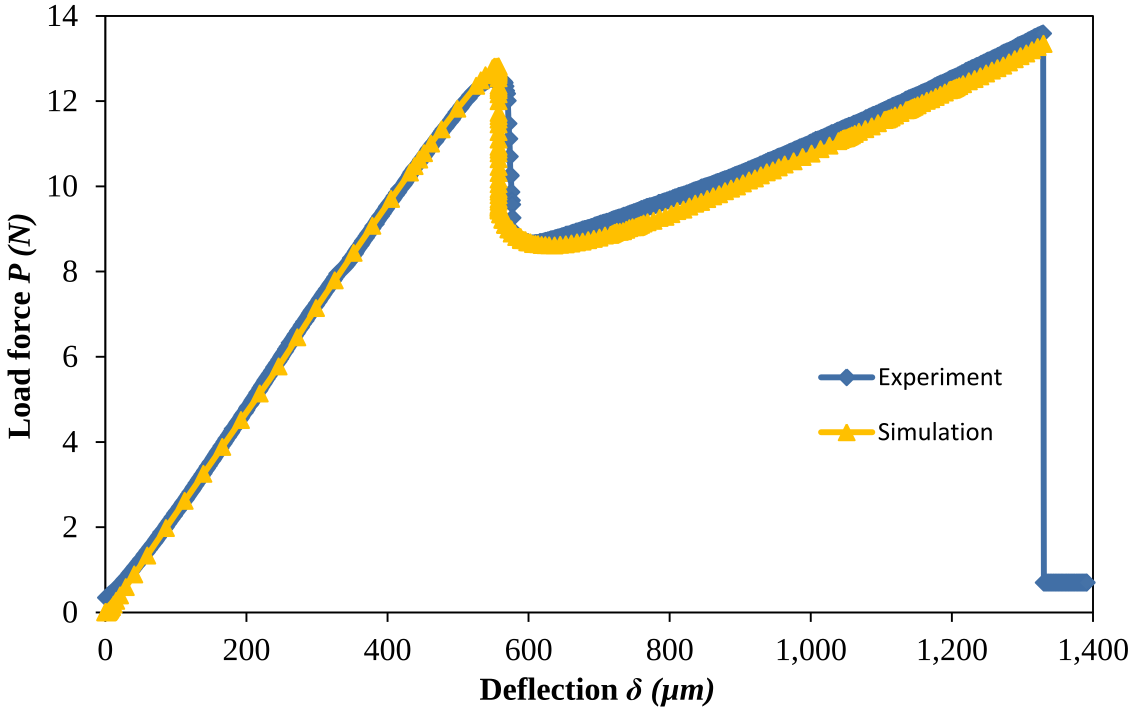

Figure 4.15 Comparison of experiments with simulation results, for which $K_s = 7.5 \times 10^2\text{N}/\text{mm}^3$ and $t_s^o = 4.6\text{MPa}$ in the corresponding ENF cohesive element model.

4.3 Cohesive Zone Modeling for Crack Prediction in LAMP

4.3.1 Three-dimensional Cohesive Element Model

In order to predict the development of cracks in the part built using the LAMP process, a three-dimensional cohesive element model is developed. Eight-node solid elements C3D8 are used to represent the bulk behavior of laminates, and cohesive elements COH3D8 are used to capture the potential delamination at the interfaces between layers. In the same manner as the numerical modeling for process-induced stress, ABAQUS user subroutines UFIELD and UEXPAN are used to achieve the evolving field of conversion degree and field dependent shrinkage strain. Each pair of bulk material layer and cohesive interface is reactivated sequentially to simulate the layer-by-layer manufacturing process. Details about this element reactivation scheme can be found in Section 2.4. Contact is defined between the top and bottom faces of the cohesive interface to avoid penetrations if the faces are compressed against each other during the analysis. By employing the experimentally obtained Mode I and Mode II fracture toughness (G_{Ic} and G_{IIc}), and the numerically calibrated cohesive parameters (t_n^o and K_n for Mode I, t_s^o and K_s for Mode II), the bilinear constitutive behavior of the cohesive elements can be fully described. Thereby, the mixed-mode cohesive damage model can be formulated, as described in Section 4.1.4.

To investigate the feasibility of this model, a part with the geometry of a hollow cylinder is analyzed first. Figure 4.16 illustrates this hollow cylinder model with labeled dimensions and boundary conditions. The layer thickness is 100 microns, and 100 layers are built.

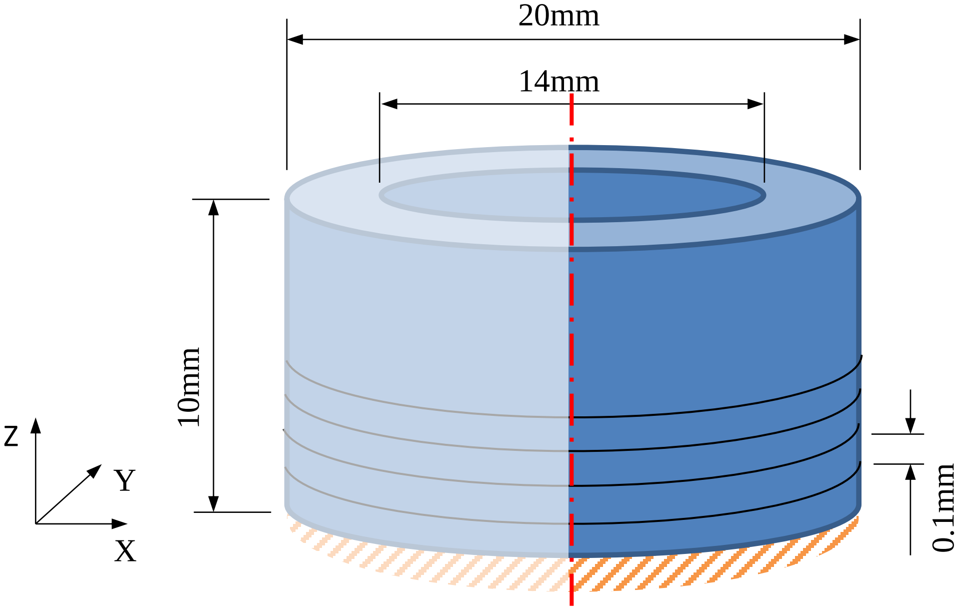

Figure 4.16 Schematic of the hollow cylinder model with dimensions and boundary conditions

It is assumed that the part is strongly bonded to the base plate during the building process (as the first step, several all-white layers are cured with long exposure times to ensure a good bonding between part and base plate during the real LAMP process). Due to the symmetric geometry, only half of the specimen is modeled in ABAQUS. The part is built with exposure time corresponding to 200μm cure depth. The corresponding print-through curve, cure-dependent elastic modulus and fracture parameters have been presented earlier. For each layer, there exist four rows of finite elements to capture bending effects. The aspect ratio between the horizontal and vertical size of the solid element is three. The mesh of the cohesive layers matches with that of the bulk layers. In other words, the element sizes along the horizontal direction are same for the solid elements and the cohesive elements. In order to conduct an accurate delamination analysis, the mesh must be sufficiently fine to ensure that enough interface elements exist within the cohesive zone length at the point of crack propagation. Otherwise, convergence will be difficult during the problem solving process. Therefore, a calculation of the anticipated cohesive zone length is conducted, and the number of elements within the cohesive zone is checked.

The length of the cohesive zone l_{cz} is defined as the distance from the crack tip to the point where the maximum cohesive traction is attained. It can be expressed as

$$l_{cz} = ME\frac{G_c}{(t^o)^2} \tag{4.16}$$

where E is the Young’s modulus of the material, G_c is the critical energy release rate, t^o is the interfacial strength, and M is a parameter that depends on each cohesive zone model. Rice’s model [83, 84] is used in this analysis, and the corresponding value for M is $\frac{9\pi}{32}$. This equation can be applied to the case of Mode I or Mode II to obtain the corresponding cohesive zone length.

In order to obtain accurate results, the tractions in the cohesive zone must be represented properly by the finite element spatial discretization [77]. When the cohesive zone is discretized by too few elements, the distribution of tractions ahead of the crack tip is not represented accurately. Therefore, a minimum number of elements, N_e, is needed in the cohesive zone to obtain reliable finite element results. According to the literature, at least three elements in the cohesive zone are required in order to successfully predict the propagation of delamination. Therefore, the maximum element size, l_e, along the layer interface is

$$l_e = l_{cz}/N_e = \frac{9\pi E G_c}{32 N_e (t^o)^2} \tag{4.17}$$

For Mode I fracture, the values of mechanical parameters and the calculation results are shown in Table 4.1. Since the actual element size (l_{actual}) used is smaller than the maximum acceptable size (l_e), the mesh is verified to be sufficiently fine to ensure that sufficient elements exist within the cohesive zone. Similar verification can also be made for Mode II.

Table 4.1 Calculation of maximum acceptable element size

E	t_n^o	G_{Ic}
414.2MPa	1.7MPa	12.8N/m
N_e	l_e	l_{actual}
3	0.54mm	0.075mm

4.3.2 Simulation Results

Simulations were conducted for the three-dimensional cohesive zone model described above. The Mises stresses and curl distortions obtained after additively building 100 layers of the hollow cylinder part are shown in Figure 4.17 and Figure 4.18, respectively.

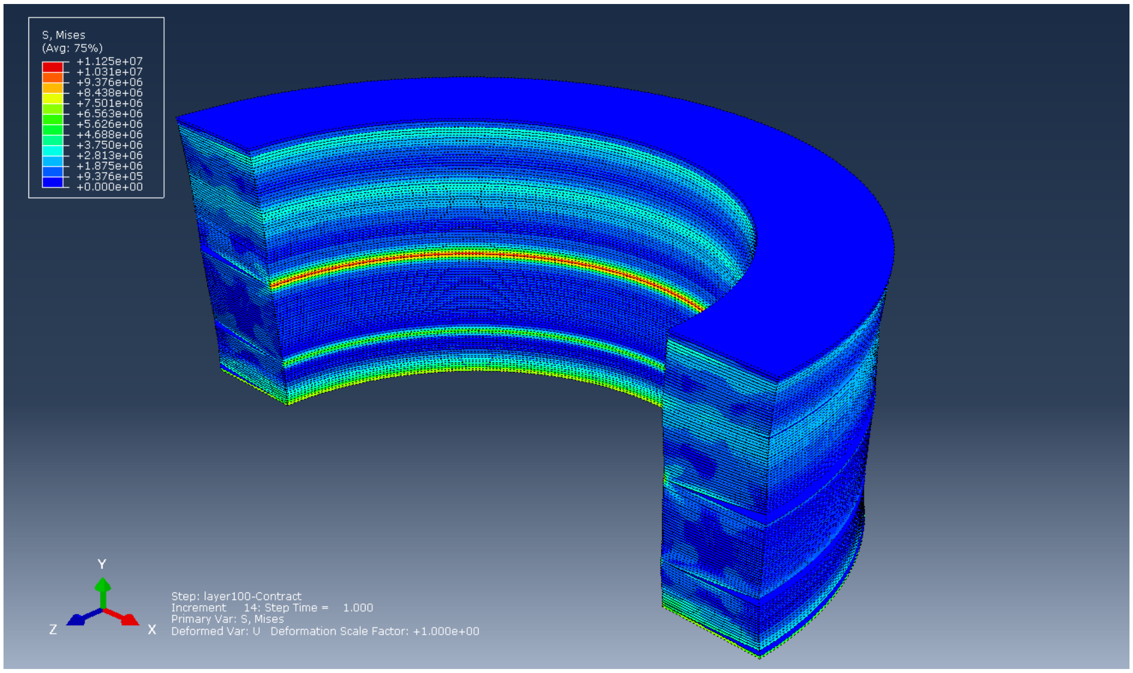

Figure 4.17 Mises stress contour obtained for the 3D cohesive element model after building 100 layers.

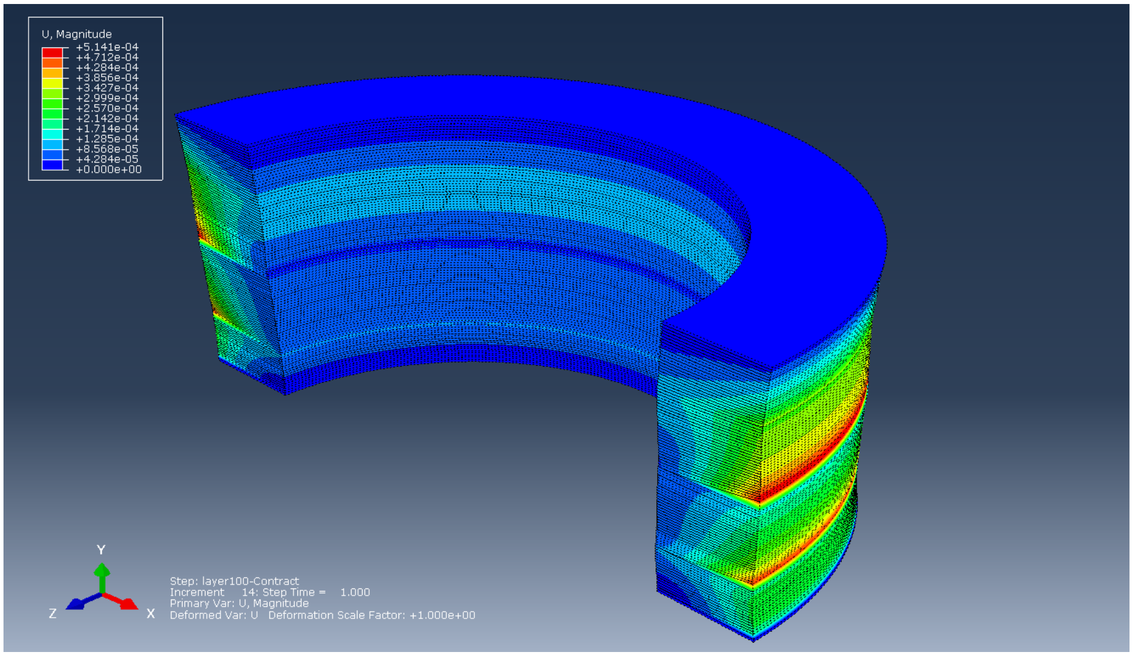

Figure 4.18 Displacement contour obtained for the 3D cohesive element model after building 100 layers.

It can be seen that the highly stressed regions are at the portions of inner surface where cracks are propagating along the corresponding layer interface. The maximum value of Mises stress occurs ahead the tip of the crack with the largest opening. Curl distortions occur at the outer surface of the cylinder due to the crack openings. In order to clearly observe the cracks on the part, contour plots of the damage variable (D) are shown in Figure 4.19 and Figure 4.20. As introduced earlier, the damage variable measures the degradation level of the cohesive elements when cracks initiate or propagate. In these figures, shades of red indicate damage to the layer interface, and the extent of crack opening can be visually estimated. As seen, free-edge cracks initiate from the outer surface of the hollow cylinder and propagate forward along the interfaces. The cracks with large openings occur every 25 layers approximately, and relatively severe curl distortions are induced accordingly. Between two of the severe cracks, cracks with smaller, medium-sized openings occur in a periodic mode with intervals of every 4 to 8 layers approximately. The periodicity can be seen more clearly in Figure 4.21, where the final crack face openings are plotted against the numbering of layer interface. This phenomenon corresponds to the periodically appearing cracks found on the surface of the mold shown in Figure 1.6. Moreover, Figure 4.22(a) illustrates a green body mold of the test cylinder, which was internally illuminated by fiber optics to enhance the detection of defects. Figure 4.22(b) shows an expanded view for a portion of the surface with enhanced contrast to demonstrate the fissures. It can be seen that there are numerous horizontal fissures which propagate throughout the circumference of the cylinder, and a similar periodicity to the mold shown in Figure 1.6 develops in the test cylinder. In addition to the fissures, a “shuffle line” can be observed, which is related to the serpentine path traversed in LAMP during large area exposure. The good consistency between numerical and experimental results validates the physics employed in the development of the cohesive element model. However, compared to results obtained experimentally, the openings of the severe cracks seem to be exaggerated in the simulation. This is probably because during the LAMP building process, the part is surrounded by slurry, and thus residual monomers may fill the openings once cracks are formed. The residual monomers will be partially cured and thereby retard the opening of crack faces. Moreover, they are usually difficult to wash away when the part is rinsed with developer, and this further blocks the observation of cracks on the part's surface. Therefore illumination is required to enhance the observation of cracks.

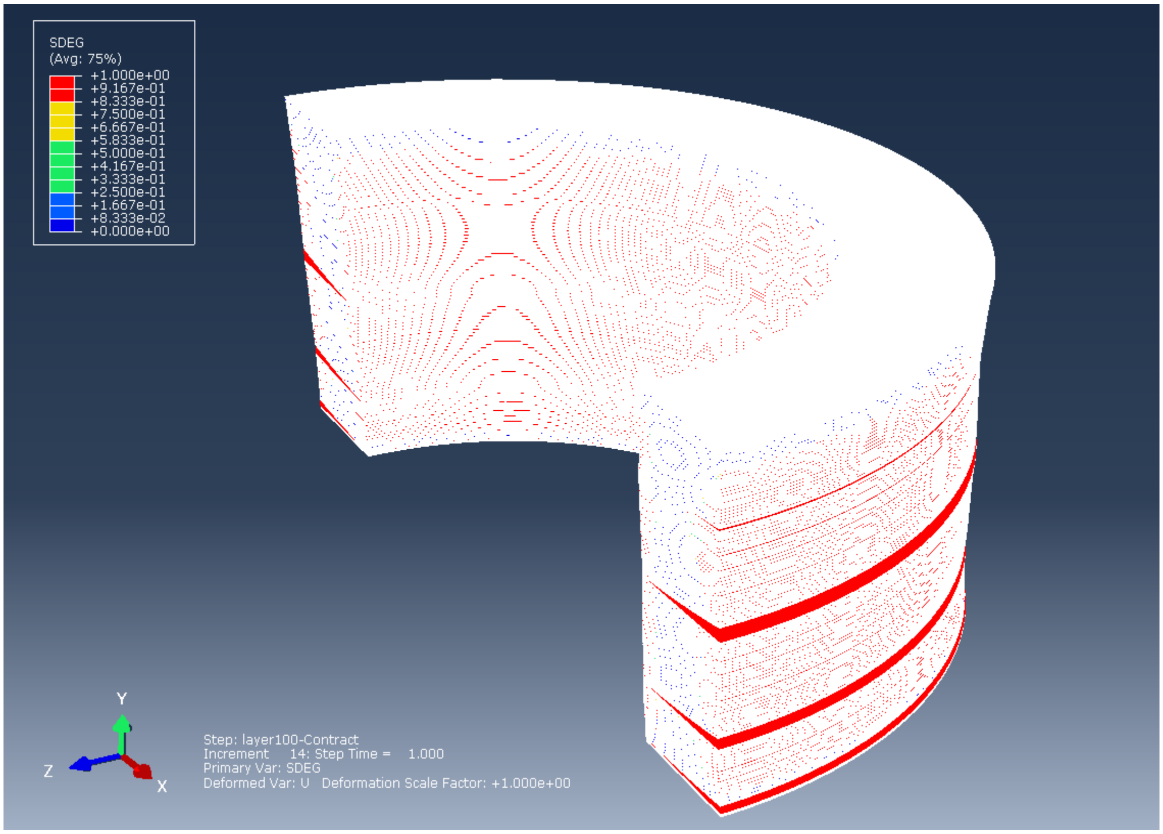

Figure 4.19 Damage contour obtained for the 3D cohesive element model after building 100 layers.

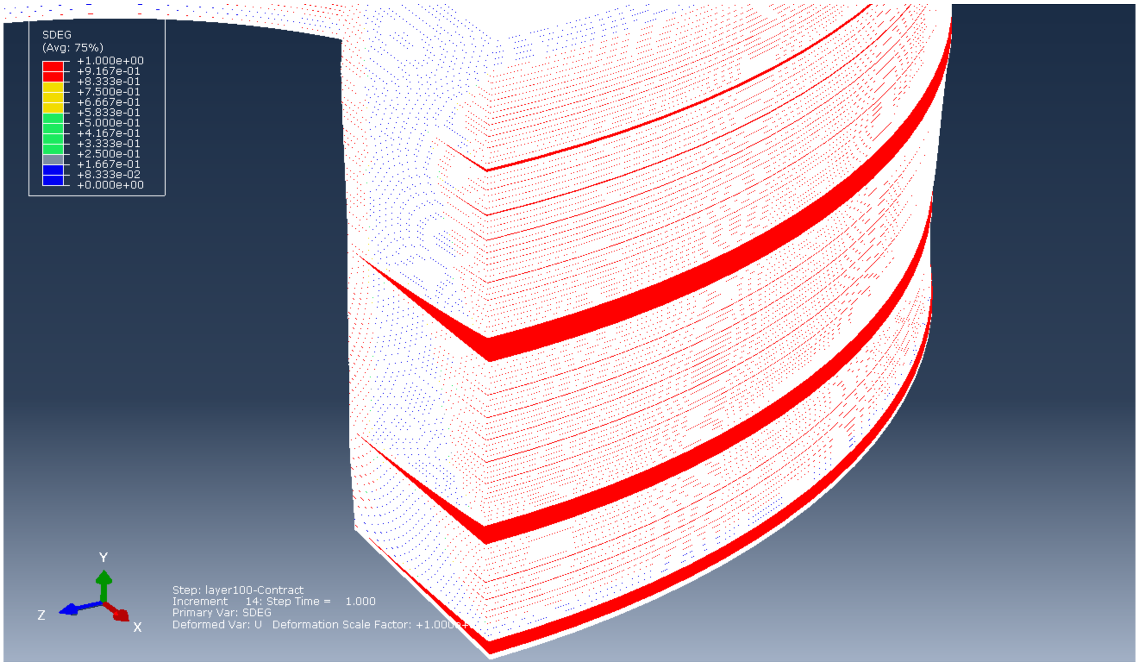

Figure 4.20 A close view of the damage contour obtained for the 3D cohesive element model after building 100 layers.

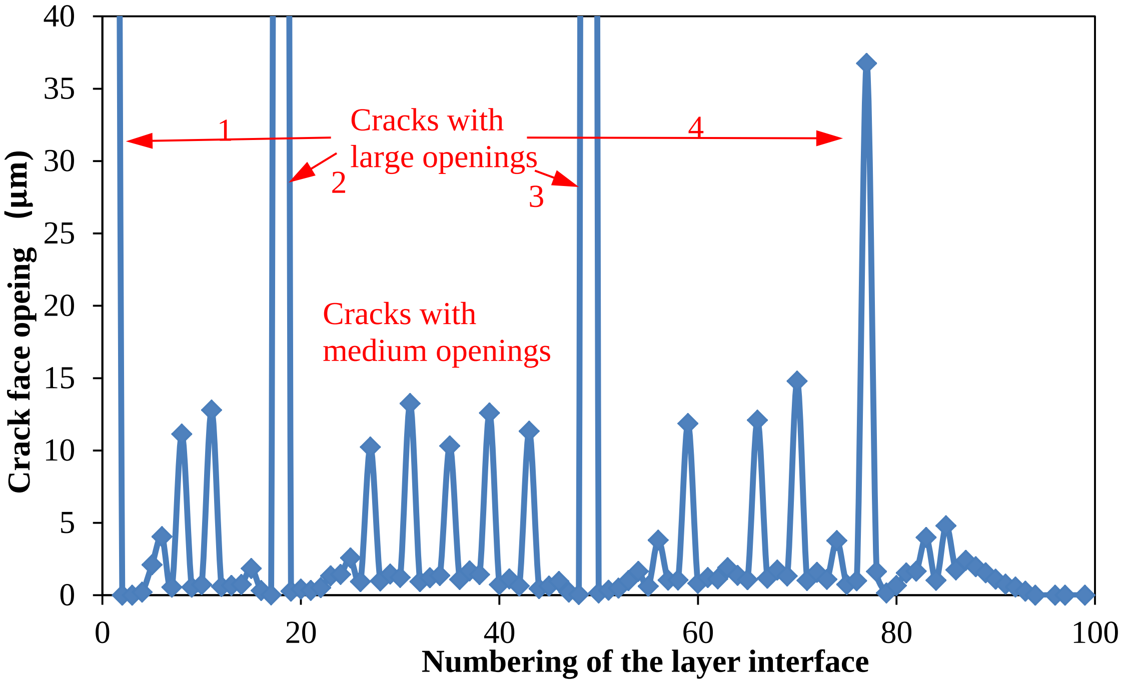

Figure 4.21 Crack face openings at the layer interfaces

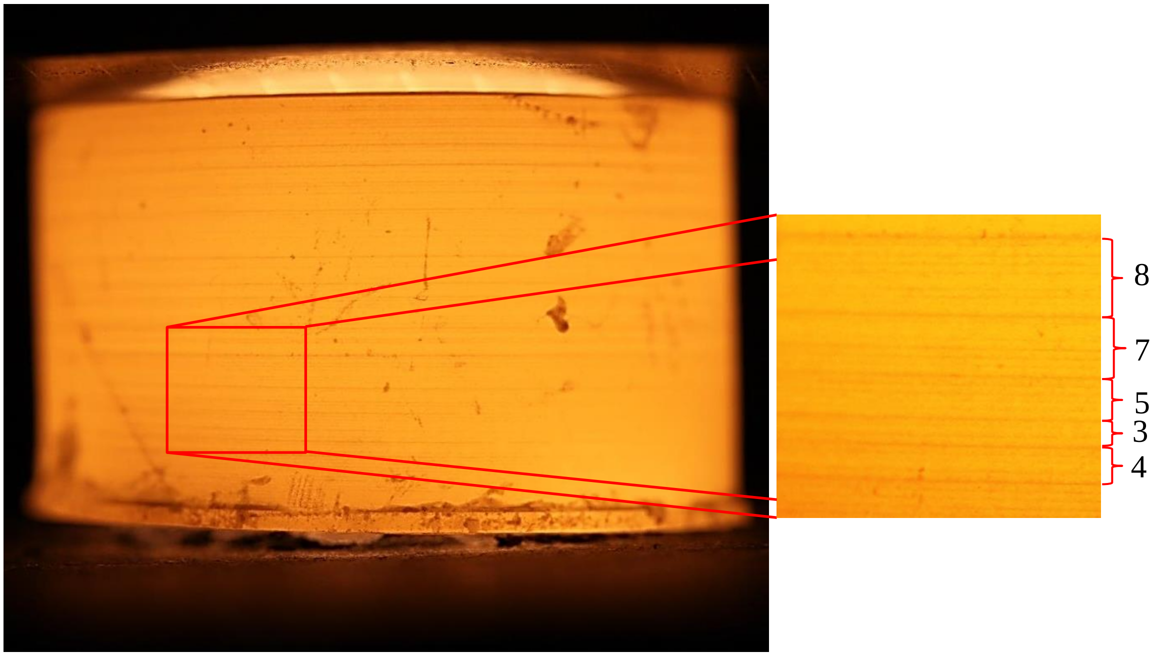

(a) (b)

Figure 4.22 Test cylinder with illumination. (a) shows the side view, (b) shows an expanded view for a portion of the surface (numbers of layers between fissures are shown).

Figure 4.23 illustrates the evolution processes of damage variables (D) at the interfaces where free-edge cracks occur. The value of D represents the level of damage in the cohesive element and the element is totally damaged if D equals one. As seen in the figure, the evolution of D presents a regular pattern. For the first interface, the value of D reaches one after 4 additional layers have been built above. For the other large and medium-sized crack openings, the values of D reach one and cracks initiate at the edges after 7 layers are built above.

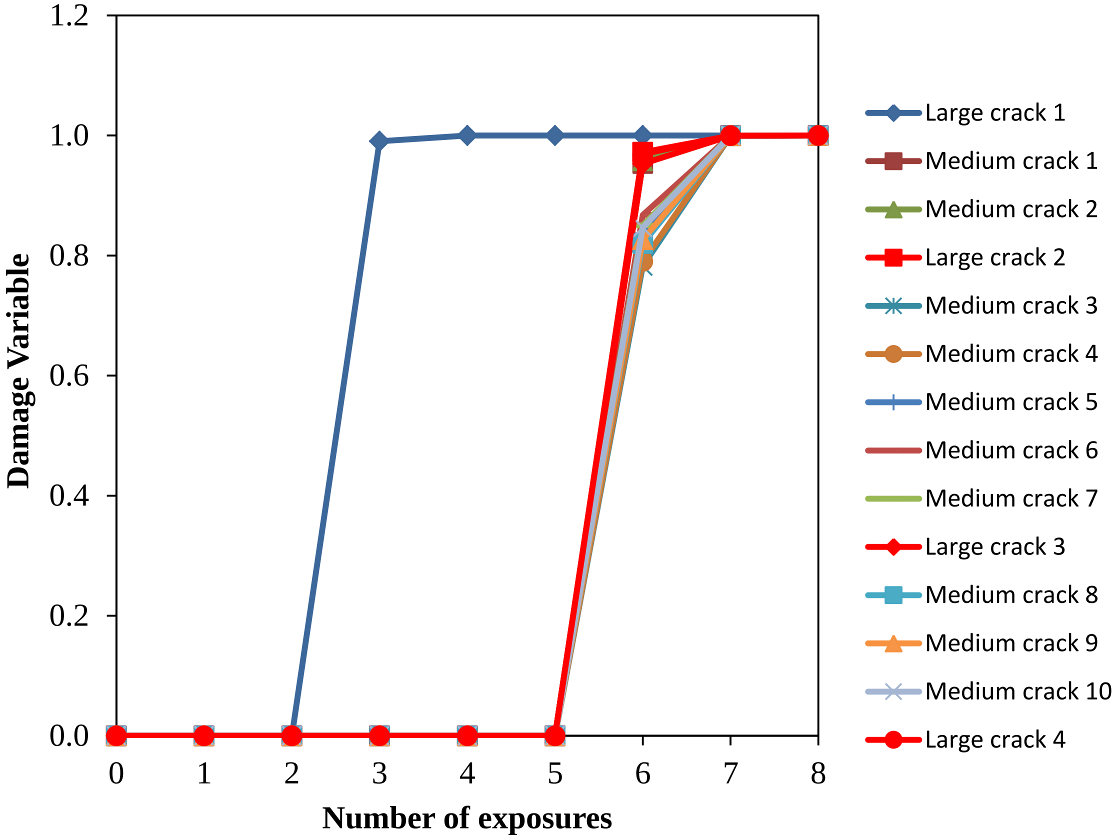

Figure 4.23 Evolution curves of damage variables (D) in cohesive elements at the free-edge of interfaces with large and medium openings.

The crack face openings of the four severe cracks are plotted against the total number of layers built during the LAMP process, as shown in Figure 4.24. It can be seen that each crack keeps opening incrementally for about 40 layers, and the opening will not decrease until another growing crack opens drastically above it (as indicated by the red vertical dash line). This is due to the fact that during the propagation process of the newly formed crack, the stresses and the tendency to curl in the body beneath will be relieved.

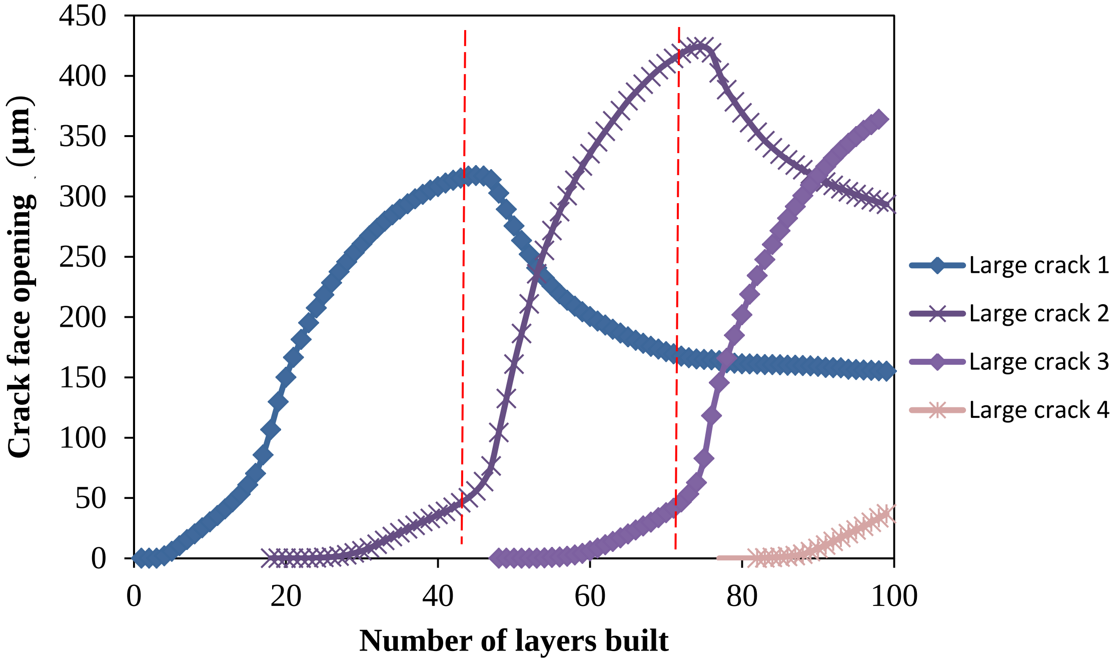

Figure 4.24 Evolution curves of crack face openings for the large-opening cracks (the horizontal axis is the total number of layers built during the LAMP process).

Similar patterns can be found for the evolutions of medium-sized crack openings, as seen in Figure 4.25 and Figure 4.26. Each crack keeps opening increasingly for about 20 layers, and the opening will not decrease until another crack grows above it and the stresses in the cracked body are relaxed. The crack face opening will then stabilize at a value of around 10 to 14 microns.

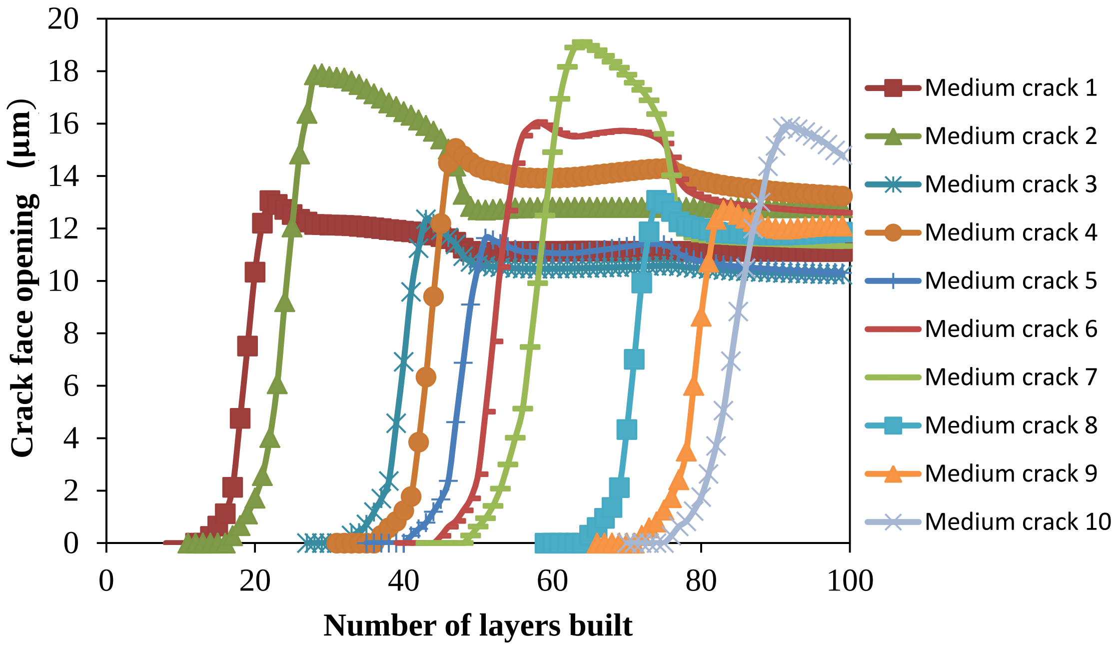

Figure 4.25 Evolution curves of crack face openings for the medium-opening cracks (the horizontal axis is the total number of layers built during the LAMP process).

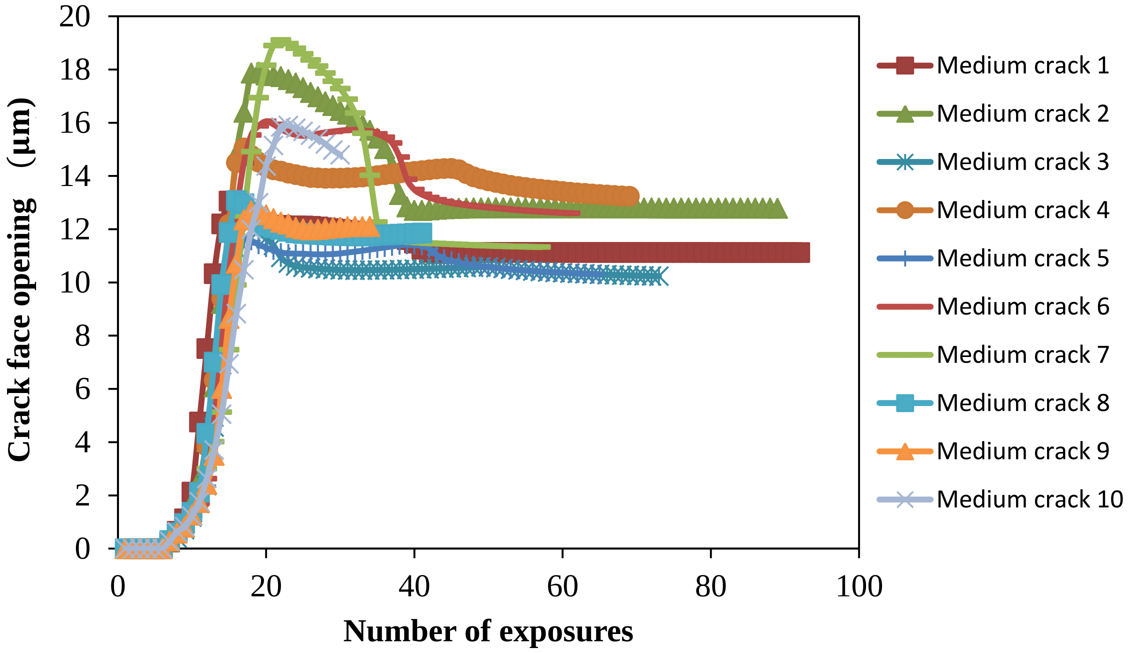

Figure 4.26 Evolution curves of crack face openings for the medium-opening cracks (the horizontal axis is the number of exposures above a certain interface).

CHAPTER 5

POSSIBLE STRATEGIES TO ALLEVIATE STRESSES AND CRACKS

Upon production through LAMP, the polymer-ceramic composite parts are subjected to post-processing steps of binder burnout and sintering, ultimately resulting in fully ceramic parts that can be used as cores and shell molds for investment casting of metal components. Some of the key requirements for castability to be satisfied by such parts are their mechanical properties in the fired state, their structural integrity, and the lack of flaws such as cracks or delaminations. However, due to polymerization shrinkage during the layer-by-layer curing process in LAMP, stresses are accumulated that can give rise to cracks and delaminations along the interfaces between adjacent layers. Cracks or delaminations present in the polymer-ceramic composite "green state" are known to propagate and manifest during the subsequent post-processing steps, resulting in unacceptable parts.

In the above chapters, based on the experimental characterization of elastic and interlaminar fracture properties, finite element models have been developed to investigate the evolution of residual stresses, and to predict the initiation and propagation of cracks in the LAMP-built parts. In this chapter, several possible strategies to reduce residual stresses and cracks are introduced and discussed. The models developed before provide a pragmatic method for simple, fast and still accurate analyses of these strategies. To save the computation time, the simulations were conducted for building 40 layers instead of 100 layers.

5.1 Reduction of Volumetric Shrinkage

Intuitively, an approach to stress mitigation could involve the overall volumetric shrinkage, since it is the root cause of residual stress. Figure 5.1 shows effects of the reduced shrinkage value on the maximum values of crack face opening and residual stress. Note that the simulations are based on the assumption that the final value of shrinkage is varied without any changes to other parameters.

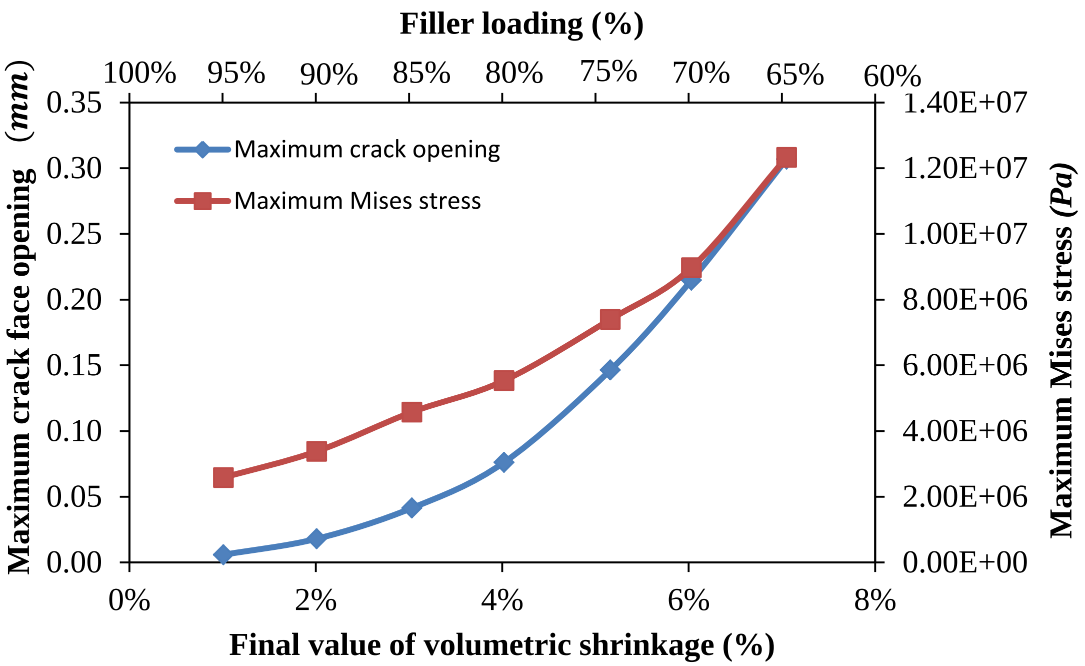

Figure 5.1 Effects of the reduced shrinkage value on the maximum values of crack face opening and residual stress

As seen in the figure, both the maximum crack face opening and the maximum Mises stress decrease with decreasing volumetric shrinkage. For the current LAMP material system (65% filler loading) and curing parameters, the overall volumetric shrinkage of the final part produced is about 7.05%. When the shrinkage value is reduced to 4%, the maximum crack face opening will be less than 0.1mm and the maximum value of Mises stress will be only 5.5MPa. From Equation (2.11), it is known that the volumetric shrinkage is directly related to the degree of conversion and particle loading percentage of the material. Therefore, lower polymerization shrinkage can be achieved by increasing the filler loading percentage, which is marked with values on the secondary horizontal axis (above the plot area). For instance, a volumetric shrinkage value of 4%

may result from the 80% filler loading. Similarly, a lower degree of conversion in the final part may reduce the polymerization shrinkage. However, due to the green strength considerations for the LAMP-manufactured part, the degree of conversion needs to be maintained as high as at least 60%. Thus, increasing the filler loading percentage is a more desirable way to reduce the overall shrinkage value. It is necessary to experimentally investigate the extent to which the filler loading can be raised, since the viscosity of slurry cannot be too high for uniformly dispensing thin layers of materials during the LAMP process. Moreover, the volumetric shrinkage may also be reduced by developing a new resin matrix. As a summary, reducing the overall polymerization shrinkage is indeed a feasible strategy to alleviate the stresses and cracks in LAMP-built parts.

5.2 Effects of Different Print-through Curves on Residual Stresses and Cracks

Due to light penetration through the upper layers, almost all of the layers, except for the topmost ones, are incrementally cured as subsequent layers above them are being exposed. This phenomenon is referred to as print-through. For each layer, the degree of conversion keeps increasing for several successive layers until no more curing occurs and a final value of conversion degree is reached. The print-through curve, which demonstrates the evolution of conversion degree in a certain layer, can be characterized through FTIR. Figure 2.7 has shown the print-through curves corresponding to five different cure depths. By conducting simulations with the cohesive model introduced earlier, the effects of various cure depths on residual stresses and cracks in LAMP-built parts are shown in Figure 5.2. It can be seen that both the maximum crack face opening and the maximum Mises stress greatly decrease with decreasing cure depth. Figure 5.3 illustrates the comparison of deformed shapes and cracking conditions for the parts produced with different cure depths. The figure clearly shows that the distortions and delaminations are significantly mitigated when using a cure depth of 120 μm. It seems that a lower cure depth is desirable for alleviating the defects in the parts. However, the degree of conversion in a newly exposed layer is only 24.2% when using the exposure time corresponding to the cure depth of 200μm. Such a lower conversion degree may cause the newly exposed layer to be swept away by the recoating arm during the material dispensing process for the next layer to be cured. Therefore, a compromise needs to be reached between strengthening the interfacial bonding after the first exposure of a newly dispensed layer and alleviating delamination in the final parts.

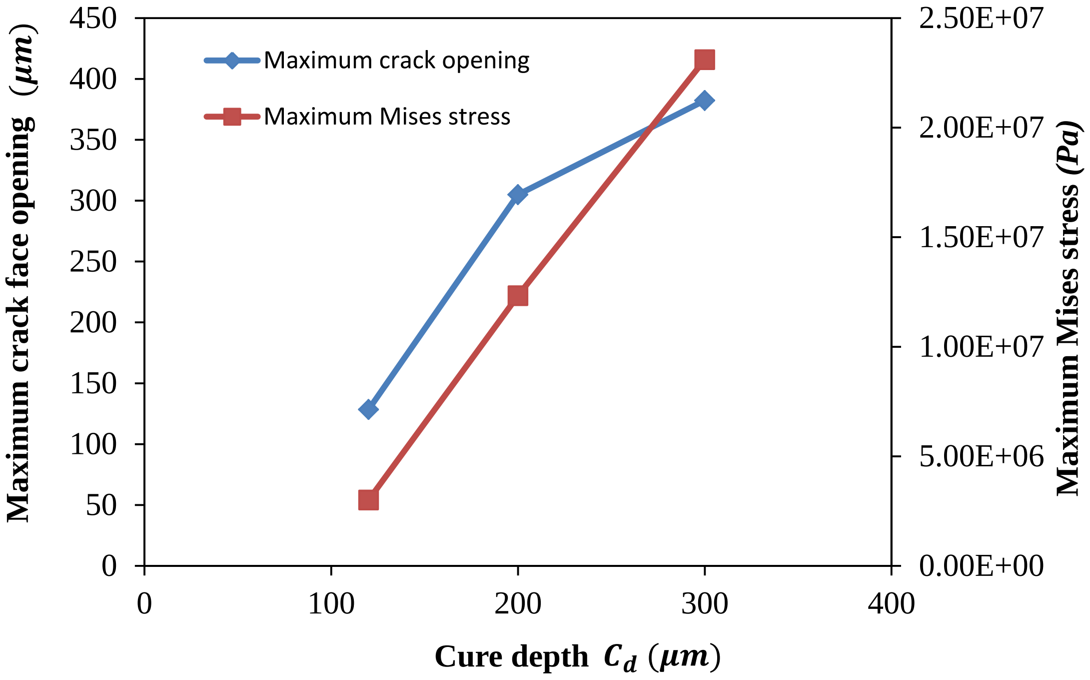

Figure 5.2 Effects of different cure depths ($120\mu m$, $200\mu m$ and $300\mu m$) on the maximum values of crack face opening and residual stress

Residual stresses result from the fact that different layers shrink by different extents during one exposure and each layer always suffers from the constraint of the layer beneath. If the material system is designed appropriately and the print-through phenomenon can be controlled well so that layers have smaller differences in volumetric shrinkage during one exposure, then the resulting residual stresses and cracks may be mitigated. Figure 5.4 and Table 5.1 shows various print-through curves that will be used here to investigate their effects on stresses and cracks.

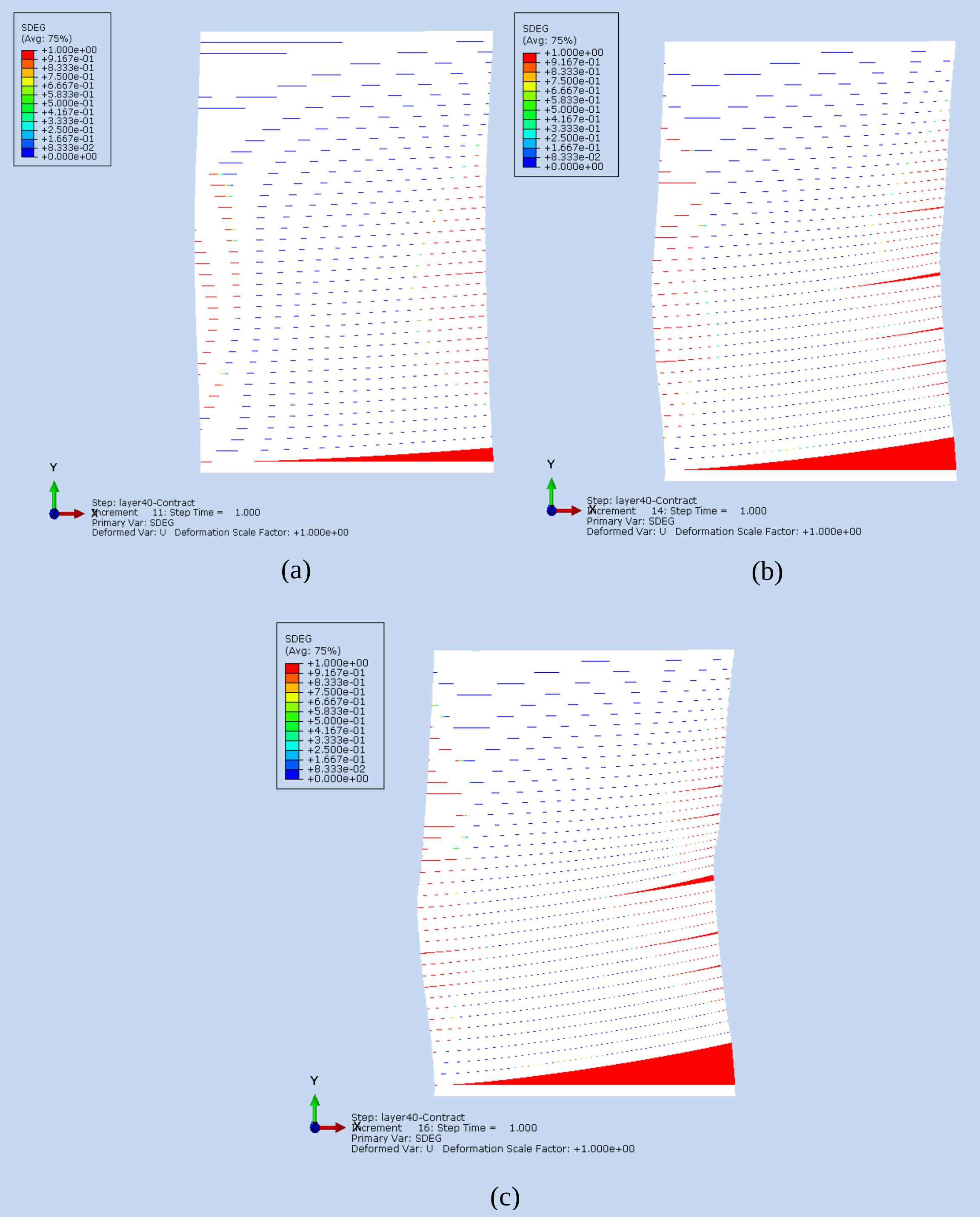

Figure 5.3 Cross-section views of the cracked parts produced using three different cure depths: (a) 120µm, (b) 200µm and (c) 300µm

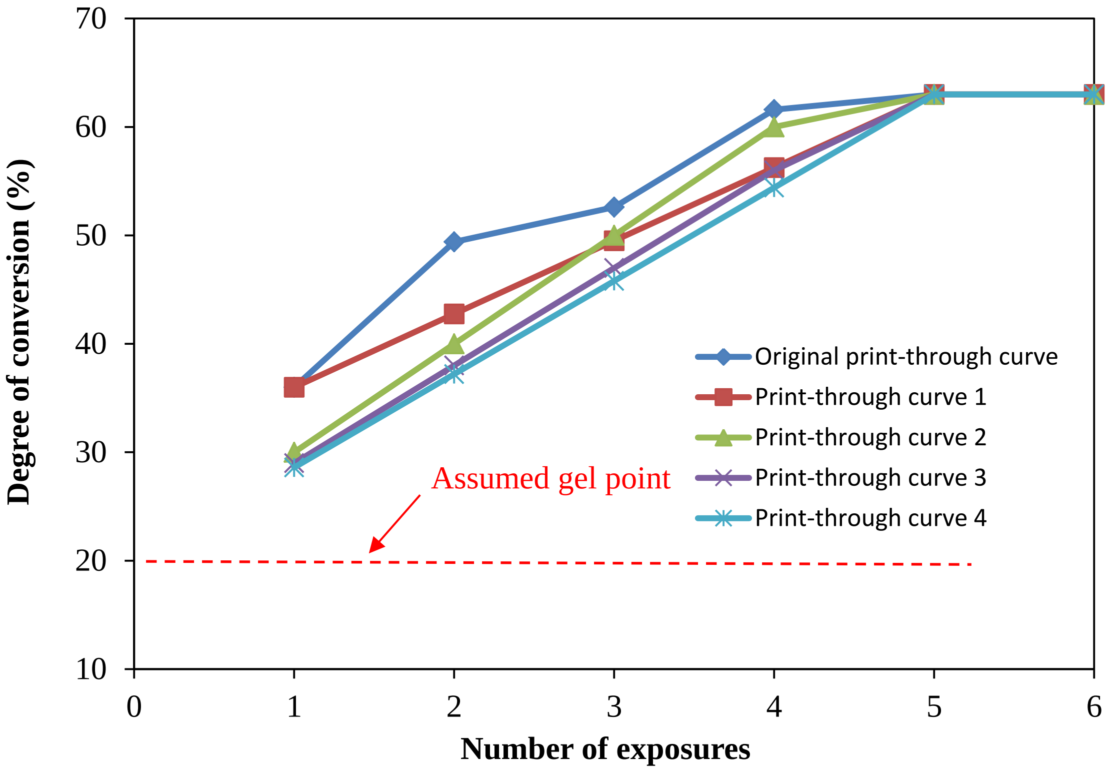

Figure 5.4 Various print-through curves

Table 5.1 Detailed values of the conversion degrees in print-through curves

Print-through curve	Conversion degree at the gel point (%)	Degree of conversion (%) after N times of exposures					
		$N = 1$	$N = 2$	$N = 3$	$N = 4$	$N = 5$	$N = 6$
Original	20	36	49.4	52.6	61.6	63	63
1	20	36	42.75	49.5	56.25	63	63
2	20	30	40	50	60	63	63
3	20	29	38	47	56	63	63
4	20	28.6	37.2	45.8	54.4	63	63

Note that all of the print-through curves investigated here have the same final value of conversion degree, so as to eliminate the effects of change in overall volumetric shrinkage. Without changing the first and final values of conversion degree, the intervals of conversion degree between any two sequential exposures are 6.75% in the first print-through curve. However, the difference between the conversion degree at the gel point and at the first exposure is 16%. In the fourth print-through curve, the intervals of conversion degree between any two sequential exposures and the difference between the conversion degree at the gel point and at the first exposure are all equal to 8.6%. Therefore, the fourth print-through curve has the highest uniformity in the conversion as a result of UV light penetration. By conducting simulations with the cohesive model introduced earlier, the effects of different print-through curves on residual stresses and cracks are shown in Figure 5.5.

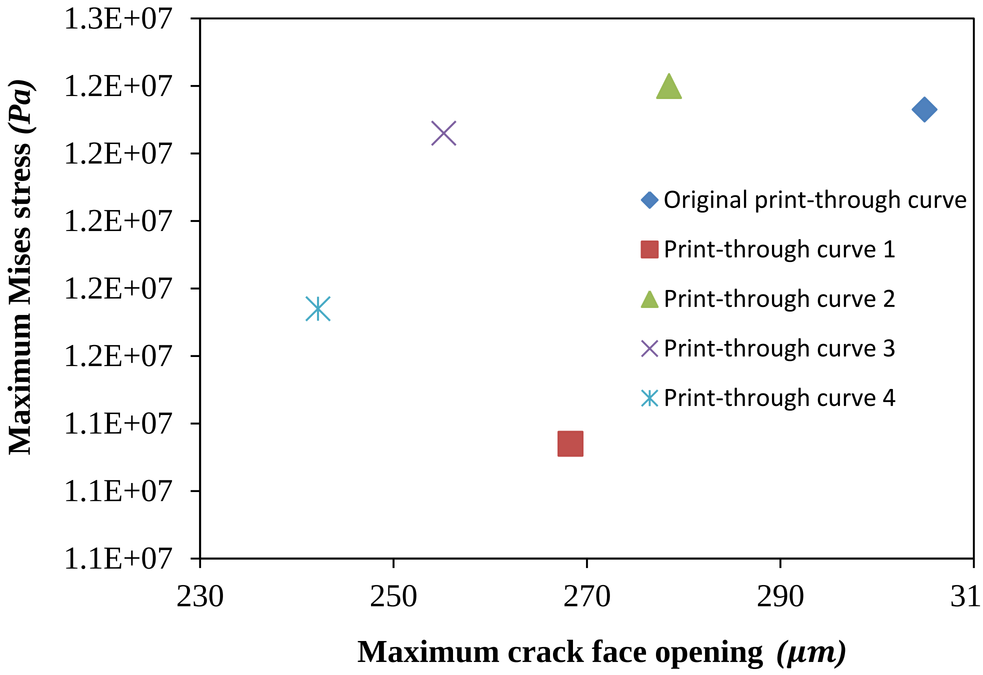

Figure 5.5 Effects of different print-through curves on the maximum values of crack face opening and residual stress.

As seen in the figure, the value of maximum Mises stress is lowest for the case using the first print-through curve. Compared to the case using the original print-through curve, the maximum values of crack opening and Mises stress decrease by 12% and 8% respectively. On the other hand, the smallest value of maximum crack opening is achieved when using the fourth print-through curve. The values of maximum crack opening and maximum Mises stress decrease by 21% and 5% respectively, compared to the case of the original print-through curve. Hence, a print-through curve with lower non-uniformity in conversion can indeed mitigate the residual stresses and cracks occurring in LAMP-built parts.

5.3 Delay of Gelation in Resin Composite

During the photopolymerization process in LAMP, the resin composite is transformed from a viscous fluid to an elastic gel at the gel point. Before the gel point, stress might be negligible since the material in pre-gel state can flow between the free surfaces and the bonded surface in a newly exposed layer. As viscosity of the developing polymer is still low, shrinkage stress can thus be rapidly compensated. At gel point, a space-spanning, load-bearing network forms, and stress starts to develop at the layer interface since the newly exposed material is constrained by adhesion to the solid layers beneath. Hence, it is rational to consider delaying the gelation of resin composite as a possible strategy to reduce the shrinkage stress and hence lessen the damage at the adhesive layer interface. Figure 5.6 shows the simulation results obtained by changing the degree of conversion at gel point in the numerical model. It can be seen that both the values of maximum crack opening and maximum Mises stress decrease drastically when the gel point is delayed (i.e. a higher conversion degree is required for gelation). Compared to the case that the resin composite gels at a conversion degree of 20%, the maximum crack opening and the maximum Mises stress reduce by 67% and 47% respectively when the gelation occurs at a conversion degree of 35%. Figure 5.7 illustrates the comparison of deformed shapes and cracking conditions for the parts produced with two different gel points. It clearly shows that the distortions and delaminations are significantly mitigated when using a delayed gel point.

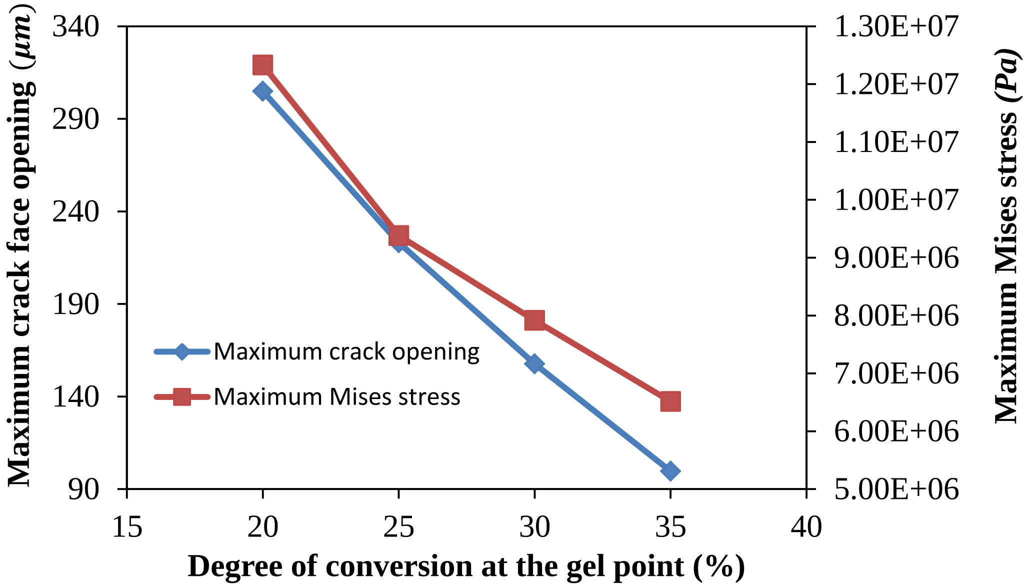

Figure 5.6 Effects of the delayed gel point on the maximum values of crack face opening and residual stress.

Both the choice of monomers in the photocurable material system and the curing conditions have the potential to affect the gel point to modest degrees. The number of reactive functional groups in a monomer also influences the gel point. Using a lower-functionality monomer tends to promote a later gel point conversion due to the less statistical likelihood of crosslink formation. Therefore, the material system can be carefully designed to obtain an appropriate gel point.

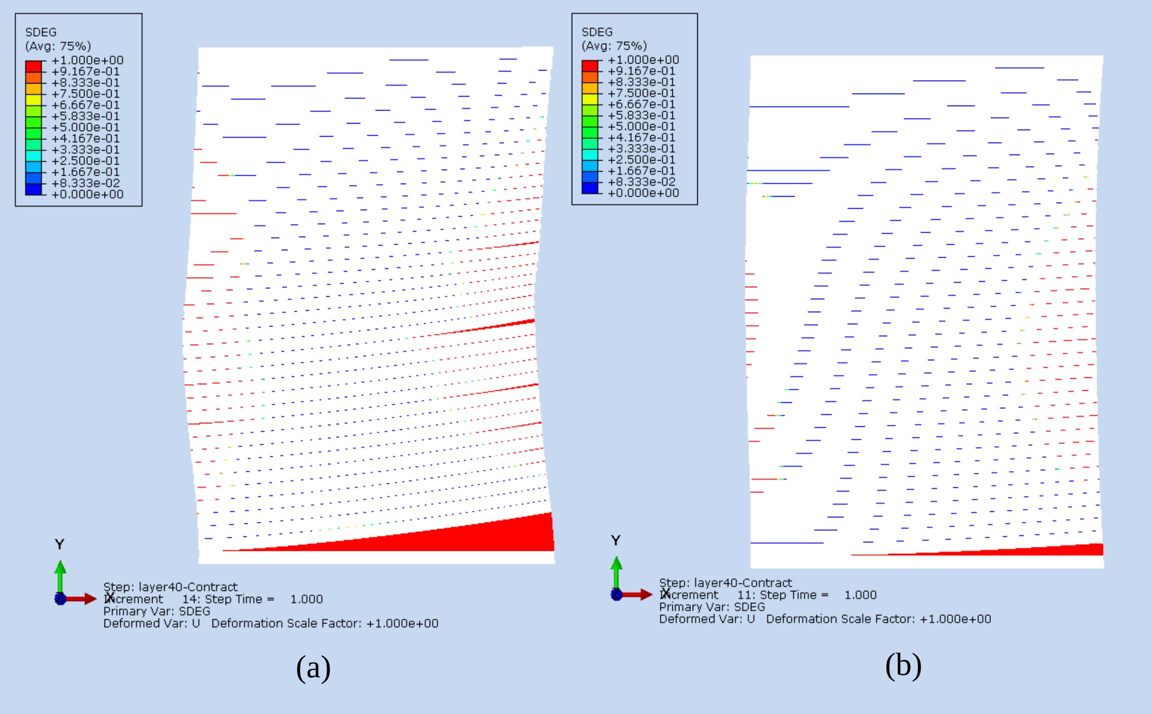

(a) (b)

Figure 5.7 Cross-section views of the cracked parts produced using gel points at the conversion degree of (a) 20% and (b) 35%

CHAPTER 6

CONCLUSION

Large Area Maskless Photopolymerization (LAMP) is a disruptive additive manufacturing technology developed for the fabrication of ceramic cores and integral-cored ceramic molds for the investment casting of turbine blades, with both high speed and fine feature resolution. Some of the key requirements for castability to be satisfied by such parts are their mechanical properties in the fired state, their structural integrity, and the lack of flaws such as cracks or delaminations. However, due to polymerization shrinkage during the layer-by-layer curing process, stresses are accumulated that can give rise to cracks and delaminations along the interfaces between adjacent layers. Cracks or delaminations present in the polymer-ceramic composite "green state" are known to propagate and manifest during the subsequent post-processing steps, resulting in unacceptable parts. The work presented in this dissertation addressed the needs for developing a feasible approach to characterize and predict the delamination process in LAMP. Fourier Transform Infrared Spectroscopy (FTIR) was used to measure the double bond conversion degree of the cured material and to characterize the print-through phenomenon. The polymerization shrinkage strain in each exposed layer was calculated on the basis of the theoretical relationship between the volumetric shrinkage as a function of double-bond formation and the degree of conversion. The cure-dependent elastic modulus of the material was also characterized. Then a finite element model was developed for predicting the evolution of residual stresses and distortions in parts built with LAMP. This model was validated by comparing the experimentally measured curvatures of bridge-shape parts with the numerical results. Moreover, the Mode I and Mode II interlaminar fracture toughness of the LAMP-built laminates were characterized, using the double cantilever beam (DCB) test and the end notched flexure (ENF) test, respectively. The Mode I and Mode II cohesive parameters, interlaminar strength and penalty stiffness, were estimated by matching the numerical load-deflection curves to the experimental ones. A mixed-mode cohesive element model was then developed for predicting crack initiation and propagation in LAMP-built parts. Finally, several possible strategies for reducing residual stresses and cracks were investigated by conducting simulations with the developed cohesive element model. In this chapter, a summary of the unique contributions made in this dissertation and the scope for future research is given.

6.1 Summary of Unique Contributions

A summary of the unique contributions made in this dissertation are listed as follows.

(a) The print-through phenomenon in LAMP was characterized using FTIR. Due to light penetration through the upper layers, almost all of the layers, except for the topmost ones, are incrementally cured as subsequent layers above them are being exposed. For each layer, the degree of conversion keeps increasing for several successive layers until no more curing occurs and a final value of conversion degree is reached. In this study, FTIR was used to characterize the print-through process and to determine the extent to which a particular layer is being cured additionally due to this phenomenon. Print-through curves (degree of conversion versus number of exposures) were obtained for the additively building processes using five different cure depths.

(b) The elastic modulus of the cured resin composite is strongly cure dependent, i.e. its value relies on the degree of conversion (α) of the resin. A convenient α-mixing rule model was presented for a theoretical description of the cure-dependent modulus. Three-point bending tests were conducted to experimentally evaluate the elastic modulus of the material with respect to the degree of conversion. The experimental results were compared with the theoretical values. Since the theoretical equation cannot capture the hardening effect of the cured resin at a higher degree of conversion, the experimental results of the cure-dependent modulus were considered as the direct input data to the numerical models.

(c) A finite element model was developed for predicting the evolution of residual stresses and distortions in the parts. To simulate the LAMP process, the degree of conversion, cure-dependent modulus and shrinkage strain were designated the three primary inputs for the numerical model. In this model, the elements of each layer were sequentially reactivated so as to simulate the layer-by-layer building process. This model was validated by comparing the experimentally measured curvatures of bridge-shape parts with the simulation results, showing good agreement.

(d) The Mode I and Mode II interlaminar fracture toughness ($G_{Ic}\ and\ G_{IIc}$) of the LAMP-built laminates were characterized, using the double cantilever beam (DCB) test and the end notched flexure (ENF) test, respectively. To compute the values of $G_{Ic}\ and\ G_{IIc}$ from the experimentally obtained load-deflection ($P - \delta$) curves, a beam theory method and a compliance-based beam method were used as the data reduction schemes for the DCB test and the ENF test, respectively. By fabricating specimens with different cure depths, $G_{Ic}\ and\ G_{IIc}$ were estimated for various degrees of conversion.

(e) In order to predict the crack initiation and propagation occurring in a LAMP-built part, a mixed-mode cohesive element model was developed. In the model, cohesive elements were placed along every layer interface of the laminates. The Mode I and Mode II cohesive parameters, interlaminar strength and penalty stiffness, were estimated by matching the numerical $P - \delta$ curves to the experimental ones obtained from the DCB tests and the ENF tests respectively, and they were used as the inputs to the model for describing the bilinear constitutive behavior of the cohesive elements. This model successfully predicted the periodic occurrence of delamination that has been observed on the mold's surface. Similar modeling schemes can be applied to any other additive manufacturing techniques for predicting the evolution of residual stresses and cracks.

(f) The presented cohesive element model enables analyses of possible stress and crack mitigation strategies in a fast and easy manner. Several possible strategies were investigated, including reduction of the overall polymerization shrinkage in the final parts, optimization of the print-through curve and delaying the gel point of resin composite.

6.2 Scope for Future Research

To improve the quality of a final part built with LAMP, there is a tremendous scope for pursuing further research. Some potential directions for future research are presented in this section.

In this dissertation, it is assumed that the conversion degree of the cured materials is homogeneous in one layer. The depth profile of double bond conversion as a function of film depth can be studied using confocal Raman microscopy [85], and thus a more complex inhomogeneous model can be made for each layer. Moreover, in the numerical model, the gel point is assumed to be at the conversion degree of 20 percent. In future work, it can be experimentally characterized through experimental methods such as real-time FTIR analysis.

In the developed cohesive element model used for prediction of cracking in LAMP, the cohesive parameters, interlaminar strength and penalty stiffness, are constant values corresponding to the final degree of conversion in the laminates. Similar to the cure-dependent fracture toughness, the values of these two cohesive parameters can be obtained for different degrees of conversion and then inputted to the model.

The characterization of interlaminar fracture properties and the developed cohesive element model are based on linear elastic fracture mechanics (LEFM). A basic assumption concerning its applicability is that crack growth is the only process in the body that dissipates energy. If other processes not associated with crack advance occur, such as viscoelasticity, then the energy release rate needs to be determined from a local analysis around the crack tip and viscoelastic fracture mechanics needs to be used in the prediction of delamination growth.

This dissertation provides several possible strategies for reducing the stresses and cracks. To achieve these strategies, the material system may be carefully designed through the adjustment of the types and amounts of the resin monomers, ceramic particles, photoinitiators and UV absorbers. Lots of experiments need to be conducted systematically to make continuous changes in the material system, so as to achieve the desired volumetric shrinkage, print-through curve and polymerization gel point.

Besides the strategies discussed in this dissertation, another promising method to mitigate the residual stresses and cracking involves the use of grayscale exposure. In pixelated grayscale exposure, the grayscale exposure image is converted into a distribution of black (unexposed) and white (exposed) pixels. This technique is similar to that used in the printing industry and is referred to as screening where the grayscale image is achieved through “half-tone” unit cells. The primary motivation for using grayscale exposure in usual applications is due to its ability to control the light intensity distribution within a single exposure [86, 87]. As a result, the cure depth can be controlled and three-dimensional patterns can be obtained within a single layer using a constant exposure time. Shrinkage stress has been studied extensively by the dental community due to the use of resin composites as dental restorations [88-91] and grayscale exposure is also considered as a scheme to achieve stress relief for photopolymerized composites. For LAMP, grayscale exposure may discretize the cured area and disconnect the network of polymeric shrinkage in one layer, and thus offer a possible way for stress relief and crack mitigation. The potential of grayscale exposure for mitigating stresses and cracks for LAMP needs to be investigated using the numerical models developed in this dissertation.

REFERENCES

[1] N. Chantarapanich, *et al.*, "Study of the Mechanical Properties of Photo-cured Epoxy Resin Fabricated by Stereolithography Process," *Songklanakarin Journal of Science & Technology,* vol. 35, p. 91, 2013.

[2] R. F. Smart and P. R. Beeley, *Investment Casting (Materials Science)*. Maney Materials Science, 1995.

[3] J. C. Han, *et al.*, "Heat Transfer and Pressure Drop in Blade Cooling Channels with Turbulence Promoters," *Final Report Texas A&M University, College Station, Department of Mechanical Engineering,* 1984.

[4] P. Dodge, "Cracks in Large Area Maskless Polymerization Molds," *MSE 280 Final Report,* vol. University of Michigan, 2011.

[5] J. P. Kruth, *et al.*, "Assessing and Comparing Influencing Factors of Rresidual Stresses in Selective Laser Melting Using a Novel Analysis Method," *Proceedings of the Institution of Mechanical Engineers Part B-Journal of Engineering Manufacture,* vol. 226, pp. 980-991, Jun 2012.

[6] G. Bugeda, *et al.*, "Numerical Analysis of Stereolithography Processes Using the Finite Element Method," *Rapid Prototyping Journal,* vol. 1, pp. 13-23, 1995.

[7] P. F. Jacobs, "Rapid Prototyping and Manufacturing: Fundamentals of Stereolithography," 1992.

[8] B. Evans and P. Jacobs, "The Development of Photopolymer Modulus with Actinic Exposure," *Proceedings of 2nd International Conference on Rapid Prototyping,* pp. 69–85, 1991.

[9] Y. Xu, "Studies on Curing Process of Photopolymer in Stereolithography," *Doctoral Thesis,* 1997.

[10] S. Kuriyama, *et al.*, *Development of FE Simulation Code for Stereolithography of Resin Cured by U.V. Ray*, 2001.

[11] Y. M. Huang and C. P. Jiang, "Curl Distortion Analysis During Photopolymerisation of Stereolithography Using Dynamic Finite Element Method," *International Journal of Advanced Manufacturing Technology,* vol. 21, pp. 586-595, 2003.

[12] Y. M. Huang and C. P. Jiang, "Numerical Analysis of a Mask Type Stereolithography Process Using a Dynamic Finite-element Method," *International Journal of Advanced Manufacturing Technology,* vol. 21, pp. 649-655, 2003.

[13] Y. M. Huang, *et al.*, "Increased Accuracy by Using Dynamic Finite Element Method in the Constrain-surface Stereolithography System," *Journal of Materials Processing Technology,* vol. 140, pp. 191-196, Sep 2003.

[14] Y. M. Huang, *et al.*, "Fundamental Study and Theoretical Analysis in a Constrained-surface Stereolithography System," *International Journal of Advanced Manufacturing Technology,* vol. 24, pp. 361-369, 2004.

[15] Y. M. Huang and H. Y. Lan, "Compensation of Distortion in the Bottom Exposure of Stereolithography Process," *International Journal of Advanced Manufacturing Technology,* vol. 27, pp. 1101-1112, Feb 2006.

[16] B. Wiedemann, *et al.*, "Investigation into the Influence of Material and Process on Part Distortion," *Rapid Prototyping Journal,* vol. 1, pp. 17-22, 1995.

[17] M. Vatani, *et al.*, "Distortion Modeling of SL Parts by Classical Lamination Theory," *Rapid Prototyping Journal,* vol. 18, pp. 188-193, 2012.

[18] D. Karalekas and D. Rapti, "Investigation of the Processing Dependence of SL Solidification Residual Stresses," *Rapid Prototyping Journal,* vol. 8, pp. 243-247, 2002.

[19] J. L. Beuth and S. H. Narayan, "Residual Stress-Driven Delamination in Deposited Multi-layers," *International Journal of Solids and Structures,* vol. 33, pp. 65-78, Jan 1996.

[20] S. H. Narayan and J. L. Beuth, "Axisymmetric Delamination in Deposited Multi-layers," *International Journal of Solids and Structures,* vol. 34, pp. 4617-4631, Dec 1997.

[21] M. Alimardani, *et al.*, "On the Delamination and Crack Formation in a Thin Wall Fabricated Using Laser Solid Freeform Fabrication Process: An Experimental-numerical Investigation," *Optics and Lasers in Engineering,* vol. 47, pp. 1160-1168, Nov 2009.

[22] M. Alimardani, *et al.*, *Effect of Preheating on the Delamination and Crack Formation in Laser Solid Freeform Fabrication Process*, 2009.

[23] M. L. Pitel, "Low-shrink Composite Resins: A Review of Their History, Strategies for Managing Shrinkage, and Clinical Significance," *Compendium of Continuing Education in Dentistry* vol. 34, pp. 578-590, 2013.

[24] M. D. Goodner and C. N. Bowman, "Development of a Comprehensive Free Radical Photopolymerization Model Incorporating Heat and Mass Transfer Effects in Thick Films," *Chemical Engineering Science*, vol. 57, pp. 887-900, 2002.

[25] K. C. Wu and J. W. Halloran, "Photopolymerization Monitoring of Ceramic Stereolithography Resins by FTIR Methods," *Journal of Materials Science*, vol. 40, pp. 71-76, 2005.

[26] L. Fano, *et al.*, "Polymerization of Dental Composite Resins Using Plasma Light," *Biomaterials*, vol. 23, pp. 1011-1015, Feb 2002.

[27] M. Dewaele, *et al.*, "Influence of Curing Protocol on Selected Properties of Light-curing Polymers: Degree of Conversion, Volume Contraction, Elastic Modulus, and Glass Transition Temperature," *Dental Materials*, vol. 25, pp. 1576-1584, Dec 2009.

[28] B. T. Gao, *et al.*, "Comparison Between a Silorane-based Composite and Methacrylate-based Composites: Shrinkage Characteristics, Thermal Properties, Gel point and Vitrification Point," *Dental Materials Journal*, vol. 31, pp. 76-85, Jan 2012.

[29] A. Visvanathan, *et al.*, "The Influence of Curing Times and Light Curing Methods on the Polymerization Shrinkage Stress of a Shrinkage-optimized Composite with Hybrid-type Prepolymer Fillers," *Dental Materials*, vol. 23, pp. 777-784, Jul 2007.

[30] N. Silikas, *et al.*, "Influence of P/L Ratio and Peroxide/amine Concentrations on Shrinkage-strain Kinetics During setting of PMMA/MMA Biomaterial Formulations," *Biomaterials*, vol. 26(2), pp. 197-204, 2005.

[31] Y. Jian, *et al.*, "Polymerization Shrinkage of (Meth)Acrylate Determined by Reflective Laser Beam Scanning," *Journal of Polymer Science Part B-Polymer Physics*, vol. 50, pp. 923-928, Jul 2012.

[32] K. Kambly, *et al.*, "Characterization of Shrinkage and Stress in Large Area Maskless Photopolymerization," *Solid Freeform Fabrication Symposium Proceedings,* 2009.

[33] S. H. Dillman and J. C. Seferis, "Kinetic Viscoelasticity for the Dynamic Mechanical Properties of Polymer Systems," *Journal of Macromolecular Science - Chemistry,* 1987.

[34] P. Prasatya, *et al.*, "A Viscoelastic Model for Predicting Isotropic Residual Stresses in Thermosetting Materials: Effects of Processing Parameters," *Journal of Composite Materials,* vol. 35, pp. 826-848, 2001.

[35] T. A. Bogetti and J. John W. Gillespie, "Process-Induced Stress and Deformation in Thick-section Thermoset Composite Laminates," *Journal of Composite Materials,* vol. 26, 1992.

[36] S. H. McGee, "Curing of Farticulate Filled Composites," *Polymer Engineering and Science,* 1982.

[37] J. Qu and M. Cherkaoui, "Fundamentals of Micromechanics of Solids," 2006.

[38] S. Y. Fu, *et al.*, "Effects of Particle Size, Particle/matrix Interface Adhesion and Particle Loading on Mechanical Properties of Particulate-polymer Composites," *Composites Part B-Engineering,* vol. 39, pp. 933-961, Sep 2008.

[39] B. E. I. 178, "Fibre-reinforced Plastic Composites - Determination of Flexural Properties," 2003.

[40] C1161-13, "Standard Test Method for Flexural Strength of Advanced Ceramics at Ambient Temperature," *American Society for Testing and Materials,* 2013.

[41] M. Gurr, *et al.*, "Novel Acrylic Nanocomposites Containing In-situ Formed Calcium Phosphate/layered Silicate Hybrid Nanoparticles for Photochemical Rapid Prototyping, Rapid Tooling and Rapid Manufacturing Processes," *Polymer,* vol. 51, pp. 5058-5070, Oct 2010.

[42] T. L. Anderson, "Fracture Mechanics: Fundamentals and Applications," 2005.

[43] A. A. Griffith, "The Phenomena of Rupture and Flow in Solids," *Philosophical Transactoins,* vol. 221, pp. 163-198, 1920.

[44] G. R. Irwin, "Onset of Fast Crack Propagation in High Strength Steel and Aluminum Allloys," *Sagamore Research conference proceedings*, vol. 2, pp. 289-305, 1956.

[45] G. R. Irwin, "Fracture Dynamics," *Fracturing of metals,* pp. 147-166, 1948.

[46] G. R. Irwin, "Analysis of Stresses and Strains Near the End of a Crack Traversing a Plate," *Journal of applied mechanics,* vol. 24, pp. 361-364, 1957.

[47] D. S. Dugdale, "Yielding in Steel Sheets Containing Slits," *Journal of the Mechanics and Physics of Solids*, vol. 8, pp. 100-104, 1960.

[48] G. I. Barenblatt, "The Mathematical Theory of Equilibrium Cracks in Brittle Fracture," *Advances in Applied Mechanics,* vol. 7, pp. 55-129, 1962.

[49] W. Zhao, "Mode I Delamination Fracture Characterization of Polymeric Composites Under Elevated Temperature," *Ph.D. Thesis, Mechanical and Aerospace Engineering, Syracuse University*, 2011.

[50] H. Yoshihara, "Mode I and Mode II Initiation Fracture Toughness and Resistance Curve of Medium Density Fiberboard Measured by Double Cantilever Beam and Three-point Bend End-notched Flexure Tests," *Engineering Fracture Mechanics,* vol. 77, pp. 2537-2549, Sep 2010.

[51] J. M. Whitney, *et al.*, "A Double Cantilever Beam Test for Characterizing Mode I Delamination of Composite Materials," *Journal of Reinforced Plastics and Composites,* vol. 1, pp. 297-313, 1982.

[52] D5528-01, "Standard Test Method for Mode I Interlaminar Fracture Toughness of Unidirectional Fiber-reinforced Polymer Composites," *American Society for Testing and Materials,* 2001.

[53] J. G. Williams, "Large Displacement and End Block Effects in the DCB Interlaminar Test in MODE-I and MODE-II," *Journal of Composite Materials,* vol. 21, pp. 330-347, Apr 1987.

[54] J. G. Williams, "The Fracture-mechanics of Delamination Tests," *Journal of Strain Analysis for Engineering Design,* vol. 24, pp. 207-214, Oct 1989.

[55] S. Hashemi, *et al.*, "Mechanics and Mechanisms of Delamination in a Poly(ether sulfone) Fiber Composite," *Composites Science and Technology,* vol. 37, pp. 429-462, 1990.

[56] J. P. Berry, "Determination of Fracture Energies by the Cleavage Technique," *Journal of Applied Physics,* vol. 34, pp. 62-66, 1963.

[57] S. Raghavan, *et al.*, "Framework to Extract Cohesive Zone Parameters Using Double Cantilever Beam and Four-Point Bend Fracture Tests," *15th IEEE International Conference on Thermal, Mechanical and Multi-Physics Simulation and Experiments in Microelectronics and Microsystems (EuroSimE)*, April 2014, Ghent, Belgium.

[58] J. D. Barrett and R. O. Foschi, "Mode II Stress-Intensity Factors for Cracked Wood Beams," *Engineering Fracture Mechanics,* vol. 9, pp. 371-378, 1977.

[59] C. Schuecker and B. D. Davidson, "Effect of Friction on the Perceived Mode II Delamination Toughness from Three- and Four-point Bend End-notched Flexure Tests," *ASTM Special Technical Publication,* pp. 334-344, 2000.

[60] H. Wang and T. Vu-Khanh, "Use of End-loaded-split (ELS) Test to Study Stable Fracture Behaviour of Composites Under Mode II Loading," *Composite Structures,* vol. 36, pp. 71-79, 1996.

[61] L. A. Carlsson, *et al.*, "On The Analysis and Design of the End Notched Flexure (ENF) Specimen for Mode II Testing," *Journal of Composite Materials,* vol. 20, pp. 594-604, 1986.

[62] M. de Moura, *Interlaminar Mode II Fracture Characterization*. Cambridge: Woodhead Publ Ltd, 2008.

[63] S. De Barros and L. Champaney, "Crack Propagation Curves on Flexure Adhesion Tests," *International Journal of Structural Integrity,* vol. 4, pp. 396-406, 2013.

[64] Y. Wang and J. G. Williams, "Corrections For Mode-II Fracture Toughness Specimens of Composites Materials," *Composites Science and Technology,* vol. 43, pp. 251-256, 1992.

[65] M. de Moura, *et al.*, "Equivalent Crack Based Mode II Fracture Characterization of Wood," *Engineering Fracture Mechanics,* vol. 73, pp. 978-993, May 2006.

[66] M. de Moura, *et al.*, "Mode II Fracture Characterization of Pinus Pinaster Wood," in *Advanced Materials Forum Iv*. vol. 587-588, A. T. Marques, *et al.*, Eds., ed Stafa-Zurich: Trans Tech Publications Ltd, 2008, pp. 594-598.

[67] M. de Moura, *et al.*, "Numerical Analysis of the ENF and ELS Tests Applied to Mode II Fracture Characterization of Cortical Bone Tissue," *Fatigue & Fracture of Engineering Materials & Structures,* vol. 34, pp. 149-158, Mar 2011.

[68] A. Hillerborg, *et al.*, "Analysis of Crack Formation and Crack Growth in Concrete by Means of Fracture Mechanics and Finite Elements," *Cement and Concrete Research,* vol. 6, pp. 773-782, 1976.

[69] A. Hillerborg, "Application of the Fictitious Crack Model to Different Types of Materials," *International Journal of Fracture,* vol. 51, pp. 95-102, 1991.

[70] M. Ortiz and A. Pandolfi, "Finite-deformation Irreversible Cohesive Elements for Three-dimensional Crack-propagation Analysis," *International Journal for Numerical Methods in Engineering,* vol. 44, pp. 1267-1282, Mar 1999.

[71] A. Needleman, "A Continuum Model for Void Nucleation by Inclusion Debonding," *Journal of Applied Mechanics-Transactions of the Asme,* vol. 54, pp. 525-531, Sep 1987.

[72] S. de Barros, *et al.*, "Numerical Simulations of Crack Propagation Tests in Adhesive Bonded Joints," *Latin American Journal of Solids and Structures,* vol. 9, pp. 339-351, 2012.

[73] M. Alfano, *et al.*, "Cohesive Zone Modeling of Mode I Fracture in Adhesive Bonded Joints," in *Advances in Fracture and Damage Mechanics VI*. vol. 348-349, J. Alfaiate, *et al.*, Eds., ed Stafa-Zurich: Trans Tech Publications Ltd, 2007, pp. 13-16.

[74] P. W. Harper and S. R. Hallett, "Cohesive Zone Length in Numerical Simulations of Composite Delamination," *Engineering Fracture Mechanics,* vol. 75, pp. 4774-4792, Nov 2008.

[75] W. C. Cui, *et al.*, "A Comparison of Failure Criteria to Predict Delamination of Unidirectional Glass Epoxy Specimens Waisted Through the Thickness," *Composites,* vol. 23, pp. 158-166, May 1992.

[76] P. P. Camanho and C. G. Davila, "Mixed-mode Decohesion Finite Elements for the Simulation of Delamination in Composite Materials," *NASA/TM-2002-211737*, pp. 1-37, 2002.

[77] G. Alfano and M. A. Crisfield, "Finite Element Interface Models for the Delamination Analysis of Laminated Composites: Mechanical and Computational Issues," *International Journal for Numerical Methods in Engineering*, vol. 50, pp. 1701-1736, Mar 2001.

[78] J. Chen, *et al.*, "Predicting Progressive Delamination of Composite Material Specimens via Interface Elements," *Mechanics of Composite Materials and Structures*, vol. 6, pp. 301-317, Oct-Dec 1999.

[79] Y. Li, *et al.*, "Improvement of Interlaminar Mechanical Properties of CFRP Laminates Using VGCF," *Composites Part a-Applied Science and Manufacturing*, vol. 40, pp. 2004-2012, Dec 2009.

[80] H. Ning, *et al.*, "Improvement of the Mode II Interface Fracture Toughness of Glass Fiber Reinforced Plastics/aluminum Laminates Through Vapor Grown Carbon Fiber Interleaves," *Science and Technology of Advanced Materials*, vol. 15, 2014.

[81] S. Raghavan, *et al.*, "Cohesive Zone Models to Predict Multiple White Bumps in Flip-Chip Assemblies," *ASME 2014 International Mechanical Engineering Congress and Exposition (IMECE2014)*, November 2014, Montreal, Canada, IMECE2014-40199.

[82] W. E. R. Krieger, *et al.*, "Cohesive Zone Experiments for Copper/Mold Compound Delamination," *64th Electronic Components and Technology Conference*, May 2014, IEEE-CPMT and EIA, Orlando, FL.

[83] J. R. Rice, "The Mechanics of Earthquake Rupture," *Physics of the Earth's Interior*, pp. 555--649, 1980.

[84] A. Turon, *et al.*, "An Engineering Solution for Mesh Size Effects in the Simulation of Delamination Using Cohesive Zone Models," *Engineering Fracture Mechanics*, vol. 74, pp. 1665-1682, Jul 2007.

[85] E. B. W. Schrof, R. KoÈniger, W. Reich, R. Schwalm, "Depth Profling of UV Cured Coatings Containing Photostabilizers by Confocal Raman Microscopy," *Progress in Organic Coatings*, vol. 35, pp. 197-204, 1999.

[86] C. Sun, *et al.*, "Projection Micro-stereolithography Using Digital Micro-mirror Dynamic Mask," *Sensors and Actuators a-Physical*, vol. 121, pp. 113-120, May 2005.

[87] L. A. Mosher, "Double Exposure Gray-scale Photolithography," *M.S. Thesis, Electrical and Computer Engineering, University of Maryland,* 2008.

[88] J. W. Stansbury, *et al.*, "Conversion-dependent Shrinkage Stress and Strain in Dental Resins and Composites," *Dental Materials,* vol. 21, pp. 56-67, Jan 2005.

[89] J. W. Stansbury and S. H. Dickens, "Determination of Double Dond Conversion in Dental Resins by Near Infrared Spectroscopy," *Dental Materials,* vol. 17, pp. 71-79, Jan 2001.

[90] A. Peutzfeldt, "Resin Composites in Dentistry: The Monomer Systems," *European Journal of Oral Sciences,* vol. 105, pp. 97-116, Apr 1997.

[91] L. G. Lovell, *et al.*, "The Effect of Cure Rate on the Mechanical Properties of Dental Resins," *Dental Materials,* vol. 17, pp. 504-511, Nov 2001.